Aalborg University

Master of Science

The Department of Energy Technology

Offshore Energy Systems

Stabilization and Control of Grid Connected Converter for Offshore Wind Power Systems

Author:
Christopher Gravers Mostrup

Supervisors:
Amin Hajizadeh
Mohsen Soltani

AALBORG UNIVERSITY
DENMARK

June 7, 2018

Christopher Gravers Mostrup

Abstract

The purpose of this thesis is to study the power control and stability of different control schemes for grid-connected inverters. The underlying basis for the thesis is to evaluate and improve upon a baseline experimental model.

The baseline included harmonic compensation for the 5^{th} and the 7^{th} harmonics. Additional harmonic compensation was tested by including compensation for the 11^{th} and 13^{th} harmonics.

The baseline was a PI current control scheme. A PR control scheme was tested and, contrary to simulation results, increased the THD. The grid currents have a significant phase lag to the reference currents in the baseline. This phase lag was eliminated with the PR control scheme.

Implementing fuzzy logic controllers to regulate the gains of the current controllers was also tested for both control schemes.

The best improvement to the baseline came from the additional harmonic compensation. Fuzzy logic controllers further reduced the THD, resulting in an overall improvement of 1.17 percentage points and a final THD of 1.81 %.

Contents

Section 1

Introduction

One of the biggest challenges in todays society is climate change and global warming. Human activities are increasing the concentration of greenhouse gasses in the atmosphere. This will result in an overall temperature rise worldwide, warming the oceans and causing the sea level to rise.

There is a need for renewable energies that can produce energy with little to no pollution. Wind- and solar power have seen significant increases in installed capacities over the last years. Denmark is one of the front-runners by aiming to be independent of fossil fuels by 2050.

However, the increasing share of renewable energy sources introduces new challenges. In the conventional electricity grid, consumption is fluctuating whereas production can be controlled and adjusted with respect to the electricity demands. Renewable energy sources are dependent on the weather conditions, meaning the production suddenly becomes intermittent. It will be increasingly more difficult to balance the grid operation as more renewable energies are introduced into the grid. The lack of efficient energy storage techniques will make large grid connections to other countries a necessity to import and export electricity.

The performance of the renewable energy power systems is also extremely important. When connecting a wind turbine (or solar panel) to the grid, it is crucial that it does not create disturbances on the grid. Stabilisation, control and synchronisation of the grid-connected power systems with the grid is therefore paramount.

1.1 Problem Statement

The objective of this thesis is to study the power control and stability of grid side converters for offshore wind power systems. This thesis is comprised of two parts; a theoretical- and an experimental part.

In the theoretical part, different control strategies are evaluated and their performances are analysed. These will be implemented and verified in the laboratory using DSPACE to achieve optimal control and stability of the systems. A baseline experimental model will be used as the underlying basis for evaluating the control schemes. Improvements to the baseline performance is sought to be achieved with the following approach:

- Acquire technical knowledge of offshore wind power systems and power electronic converters.
- Simulate and compare different control strategies for grid-connected inverters.
- Implement proposed control strategies in the experimental setup.
- Optimise the currently implemented baseline experimental model.

Section 2

System Description

Wind turbines capture the energy from the wind and converts it into rotational mechanical energy with its aerodynamically designed blades. The design of the blades is a compromise between performance and costs. The same applies to the other components of a wind turbine, wherefore there are many different constructions used. The wind turbine can be with or without gearbox and power conversion. Overall, there are three types of wind turbine technologies:

- **Without power electronics:** The cheapest solutions are fixed speed wind turbines. They can regulate active power very fast. The fixed speed stems from using gear boxes and induction generators. The power production is controlled aerodynamically with stall, active stall and pitch control.
- **With partially rated power electronics:** These types of turbines do also have induction generators, but with a rounded rotor. Adding a resistance to the rotor enables control using power electronics. The turbine functions as a dynamic power source to the grid due to the power electronics, enabling control of both active- and reactive power.
- **With full-scale power electronics:** Turbines using full-scale power electronics can have many different configurations. They can use induction-, synchronous generators or synchronous generators multi-pole (with or without permanent magnets). The type of generator used determines whether the turbine has a gear box. Active- and reactive power can be controlled incredibly fast, due to the generator being decoupled from the grid by utilising a DC-link. The power conversion will add an increased loss, but it is often outweighed by the improved technical performance. This system has more sensitive electronic parts, adding to its complexity, but is generally the best technical solution.

This thesis will focus on the latter type of wind turbines. The wind power system can be split into two parts; the generator- and the grid since converter. The generator side converter is not a concern in this thesis, wherefore all focus lies on the grid side converter. The grid side converter consists of an inverter, an LCL filter, a grid connection and a pulse-width modulator for controlling the inverter.

2.1 Voltage Source Inverter

As mentioned, the generator is decoupled from the grid by a DC-link. The grid side converter converts the DC components to AC components that can be injected into the grid. A three-phase voltage source inverter consists of three half-bridges, preferably using insulated-gate bipolar transistors (IGBTs) due to their high efficiency and fast switching. Each half-bridge has two IGBTs that function in pairs. The pair cannot be switched ON simultaneously. Voltage source inverters are often used to transfer real power from a DC source to an AC load. The power comes from the DC source, wherefore the inverter does not produce any power itself. The DC source sometimes have its own control system for keeping the DC voltage constant.[1]

2.2 Pulse-Width Modulation

The voltage source inverter is controlled by a space vector pulse-width modulator (SVPWM). Space vector modulation is an algorithm for controlling the switching of the PWM. The basic principle behind the space vector modulation is to control the switches so that both switches in a leg is not ON at the same time. If this were to happen, the DC supply would short circuit. It is achieved by complementary operation within each leg, meaning if $IGBT_1$ is ON then $IGBT_2$ is OFF and vice versa. This results in eight possible switching vectors for the inverter, consisting of six active switching vectors and two zero vectors. SVPWM is considered to be one of the better techniques since it results in better fundamental output voltage, reduced switching frequency, and, most importantly, improved harmonic performance and reduced total harmonic distortion.[2][3][4]

The PWM generator used in this thesis generates pulses for carrier-based PWM. The PWM generator uses a carrier- and a reference signal. The carrier signal is a symmetrical triangle signal, whereas the reference signal is the reference voltage coming from the actuator output of the current controllers. The two signals are compared and used to determine the pulses for the IGBTs in the inverter, see Figure 2.1[5].

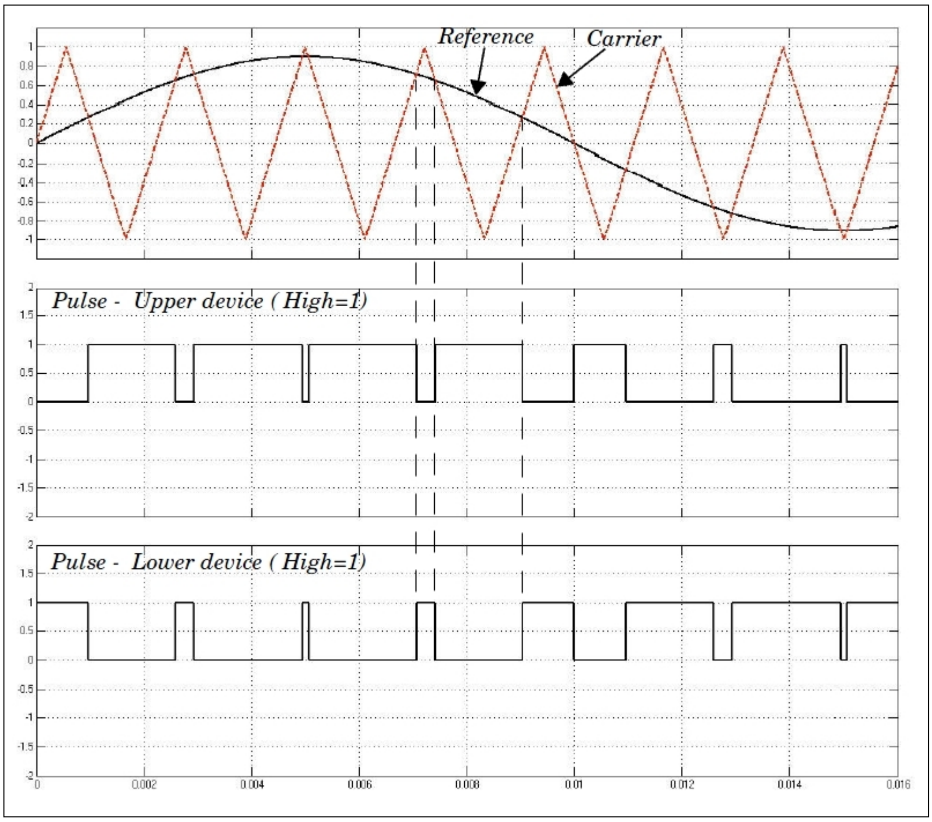

Figure 2.1: The principle behind the pulse-width modulator. The symmetrical triangle carrier signal is compared to the modulation signal to determine the switching of the IGBTs in the inverter.

As can be seen, the upper IGBT in the leg is turned ON whenever the reference signal is larger than the carrier signal. On the contrary, the lower IGBT is switched ON when the carrier signal is larger than the reference signal.[5]

2.3 LCL Filter

In grid-connected power systems, the filter used will often vary depending on the requirements. In many applications, a standard L filter is used, but it does not have great harmonic attenuation. It will result in a heavy voltage drop and the inductor needs to be very big in size.

LCL filters are often used instead of the conventional L filter for achieving smooth output currents from the inverter. It achieves higher attenuation and is cheaper, since the size and weight is significantly lower. LCL filters reduce distortion on the current injected into the grid, allowing for better performance.

The LCL filter consists of two inductors and a capacitor. The overall purpose is to transform the PWM signals to sinusoidal waveforms in order to synchronise with the grid. In the experimental results, the grid side inductor is replaced with an ideal transformer so that the system is decoupled from the grid. The ideal transformer serves the same purpose as a grid side inductor.[6]

Section 3

System Control

The grid-connected voltage source inverter is controlled by a fast internal current loop, which is used to regulate the grid current. The purpose of the current control loop is to ensure power quality and current stability. Harmonic compensation and dynamic response are important characteristics of the current controller.[7, p. 3]

3.1 Reference Frames

The complexity of three-phase systems can make it difficult to regulate and control due to the continuously changing components. Mathematical transformations are often used to decouple variables and can aid in solving equations containing time varying quantities by referring all variables to a common frame of reference. Essentially, the transforms are used to rotate the reference frames of AC waveforms in such a way that they become DC quantities. The DC signals are used to control the power system, since they are much easier to control. The outputs of the current control system are transformed back to their original three-phase AC reference frame.

The two most common methods of transformation are the Clarke- and Park transformations. The Clarke transformation converts vectors in the abc-reference frame into vectors in the $\alpha\beta0$-reference frame. The $\alpha\beta0$-reference frame is also referred to as the stationary reference frame. Whereas the abc-reference frame has three-phase quantities at an angle of 120 degrees to each other, the α- and β quantities are perpendicular to each other. The Clarke transformation of the three-phase currents can be performed with Equation 3.1.

$$\begin{bmatrix} i_\alpha \\ i_\beta \\ 0 \end{bmatrix} = \sqrt{\frac{2}{3}} \begin{bmatrix} 1 & -\frac{1}{2} & -\frac{1}{2} \\ 0 & \frac{\sqrt{3}}{2} & -\frac{\sqrt{3}}{2} \\ \frac{1}{\sqrt{2}} & \frac{1}{\sqrt{2}} & \frac{1}{\sqrt{2}} \end{bmatrix} \begin{bmatrix} i_a \\ i_b \\ i_c \end{bmatrix} \tag{3.1}$$

The Park transformation is used to rotate the quantities from $\alpha\beta0$-reference frame to dq0-reference frame. The dq0-frame is also referred to as the synchronous reference frame. The dq quantities are still perpendicular to each other, but they are shifted at an angle θ to the $\alpha\beta$ axis. θ is the instantaneous angle of an arbitrary frequency, the angular grid frequency ω_0 in this instance. The Park transformation of the currents from stationary-to synchronous reference frame can be seen in Equation 3.2.[8][9]

$$\begin{bmatrix} i_d \\ i_q \\ 0 \end{bmatrix} = \begin{bmatrix} cos\theta & sin\theta & 0 \\ -sin\theta & cos\theta & 0 \\ 0 & 0 & 1 \end{bmatrix} \begin{bmatrix} i_\alpha \\ i_\beta \\ 0 \end{bmatrix} \tag{3.2}$$

3.2 Phased-Locked Loop

There are many different methods for grid synchronisation in distributed generation systems. The one used in this thesis is the phase-locked loop (PLL) technique. The PLL is a device that uses one signal to track another. It is common to implement the PLL in synchronous reference frame, whose construction can be seen in Figure 3.1.

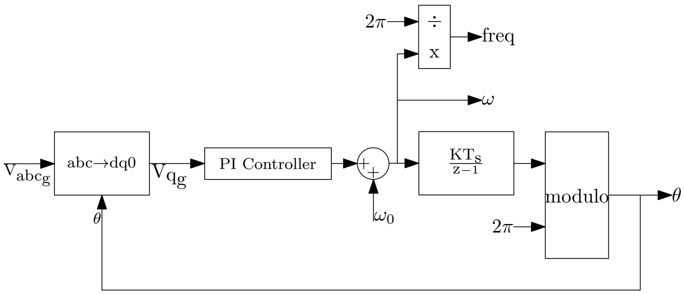

Figure 3.1: Phase-locked loop implemented in synchronous reference frame and used for grid synchronisation.

The input of the PLL is the grid voltages that are transformed into dq-frame. Only the V_d component is used in the PLL, where the reference voltage $V_{d_{ref}}$ is set to zero. A PI controller is usually used to regulate and control this variable. The actuator output of the PI controller is the error of the grid frequency. This error is added onto the nominal angular grid frequency, resulting in the angular grid frequency. This frequency is then integrated, with a inclination cut every 2π, in order to obtain the phase angle. The phase angle is fed back into the abc to dq transformation, constructing a feedback loop.[10]

Distortions in the grid can impact the operation of the PLL. The dynamic response of the PLL is determined by the dynamic algorithm used. Since the PLL in this thesis is only used to synchronise the control variables to the grid voltages, a slow dynamic algorithm is used.

The tuning of the PLL is determined from the settling time, T_{set}, and the damping ratio, ζ, of the system. The continuous time domain transfer function of the PLL system is:

$$G_{PLL}(s) = \frac{K_P s + \frac{K_P}{T_I}}{s^2 + K_P s + \frac{K_P}{T_I}} \tag{3.3}$$

This expression is comparable to the standard second-order transfer function having a zero:

$$G(s) = \frac{2\zeta\omega_n s + \omega_n^2}{s^2 + 2\zeta\omega_n s + \omega_n^2} \tag{3.4}$$

The gains for the PI controller in the PLL can be derived from the two expressions, 3.3 and 3.4:

$$K_P = \frac{9.2}{T_{set}} \quad \wedge \quad T_I = \frac{\zeta^2 T_{set}}{2.3} \qquad \text{where} \quad \omega_n = \frac{4.6}{\zeta T_{set}} \tag{3.5}$$

The damping ratio and settling time are provided in the baseline experimental setup; $\zeta = 0.7$ and T_{set}=0.1.[11]

3.3 Reference Power

The reference currents used in the control loops are calculated from the active- and reactive power requirements. In all models, the values of active- and reactive power can be changed to evaluate and meet certain demands. The instantaneous active- and reactive powers in dq-frame can be calculated from Equations 3.6 and 3.7, respectively.

$$P = \frac{3}{2}(V_d I_d + V_q I_q) \tag{3.6}$$

$$Q = \frac{3}{2}(V_q I_d - V_d I_q) \tag{3.7}$$

The active- and reactive power requirements are known and the two voltages are measured from the grid. Solving the two equations for the two unknown current variables will give the reference currents that are used in the control schemes.[12]

If the control schemes are implemented in stationary reference frame, the dq voltages are replaced in the two equations with the $\alpha\beta$ voltages, whereas the corresponding $\alpha\beta$ reference currents are calculated.

3.4 Harmonic Compensation

There are numerous ways to compensate current harmonics in grid-connected power systems. A common way is using PR controllers to reduce the amount of harmonic distortion for the particular harmonics. PR controllers will be evaluated and tested in this thesis, however harmonic compensation is still needed for the PI control schemes.

The method used in this thesis is based upon the functioning principle of a PR controller. Cascaded integrator compensators are used for each of the harmonics. The harmonic compensation is performed after the current controllers, instead of being integrated into the current controller (as is the case with PR controllers). Figure 3.2 shows the harmonic compensation scheme used in the simulations and experimental setup.[13]

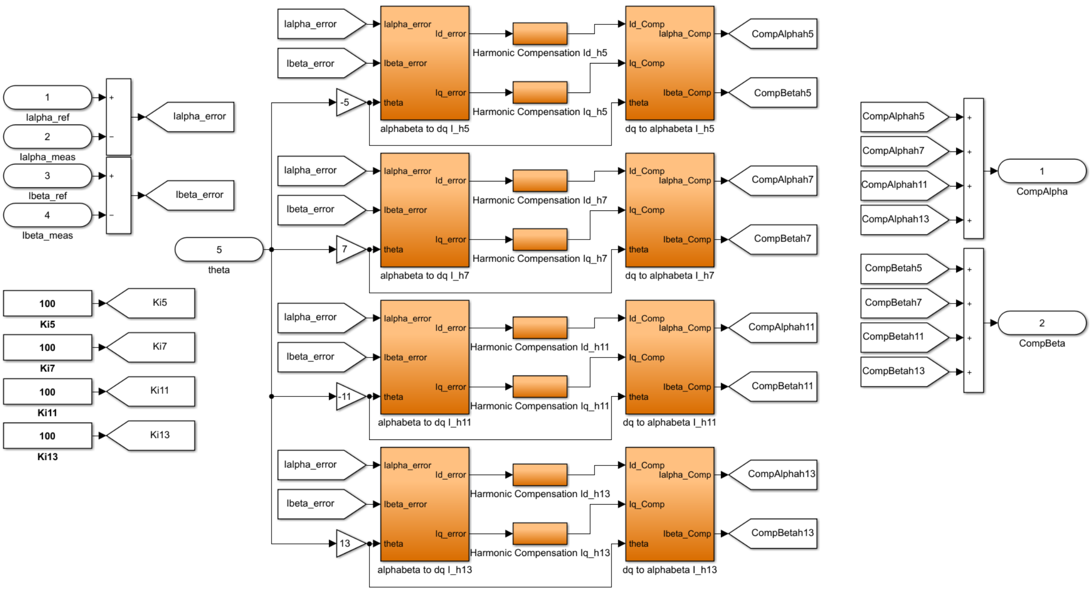

Figure 3.2: Integrator based harmonic compensation, including the 5^{th}, 7^{th}, 11^{th} and 13^{th} harmonics.

The errors between the reference- and measured currents in α- and β-frame is transformed into dq-frame. Normally, when transforming to or from dq-frame, the angle θ of the fundamental frequency is used. However, the current errors are adjusted so they match the harmonics that must be compensated for. This is done by multiplying θ with -5, 7, -11 or 13.

Harmonics are not only characterised by their name and frequency, but also their sequence. Harmonic sequence refers to the phasor rotation of the harmonic voltages and -currents in comparison to the fundamental waveform. Positive sequence harmonics rotate in the same direction as the fundamental frequency, whereas negative sequence harmonics rotate in the opposite direction. Triplen harmonics (multiples of 3) have no rotational sequence, meaning they do not rotate and are in phase with the fundamental frequency.

Only odd-numbered harmonics change the shape of the fundamental waveform. Even-numbered harmonics have an equal number of positive- and negative half cycles, resulting in the half cycles cancelling out each other. The sign of the gains to θ for each harmonic indicate whether the corresponding harmonic rotates with or against the fundamental waveform.[14][15]

The transformed dq current errors are compensated using integral anti-windup integrators. Windup occurs when an actuator gets saturated and a normal linear control problem becomes nonlinear, since the controller can no longer produce the output required. This happens because of some limits on performance, e.g. a valve cannot be opened more than fully. When the actuator is saturated, the error continuously increases. This will result in problems within the integral parts of e.g. PID controllers, given that the integral part tracks the past errors. The system response will overshoot, which can take long for the system to correct. This issue is usually prevented by resetting or limiting the integral part of the controller.

The method used for anti-windup in this thesis is the so-called "Dow method". It utilises the "Back-Calculation method", but only the integral part is being back-calculated to reset the integral windup. Extra measures are only taken when the integrator is saturated.[16]

The actuator outputs for all the harmonic compensators are added to the reference voltage, used as an input in the SVPWM.

3.5 PI Control

Synchronous reference frame (dq-frame) is commonly used in many applications due to its effectiveness and relative simplicity. The inverter current- and grid voltage waveforms are transformed into a reference frame that rotates synchronously with the grid voltages. This results in DC quantities that can eliminate the steady-state error that usually comes with the use of proportional-integral (PI) control, while simultaneously providing independent control of active- and reactive power. PI controllers are often used in dq control structures due to their satisfactory behaviour when regulating DC quantities.[7][17]

The PI control scheme used in this paper can be seen in Figure 3.3.[7][18][19]

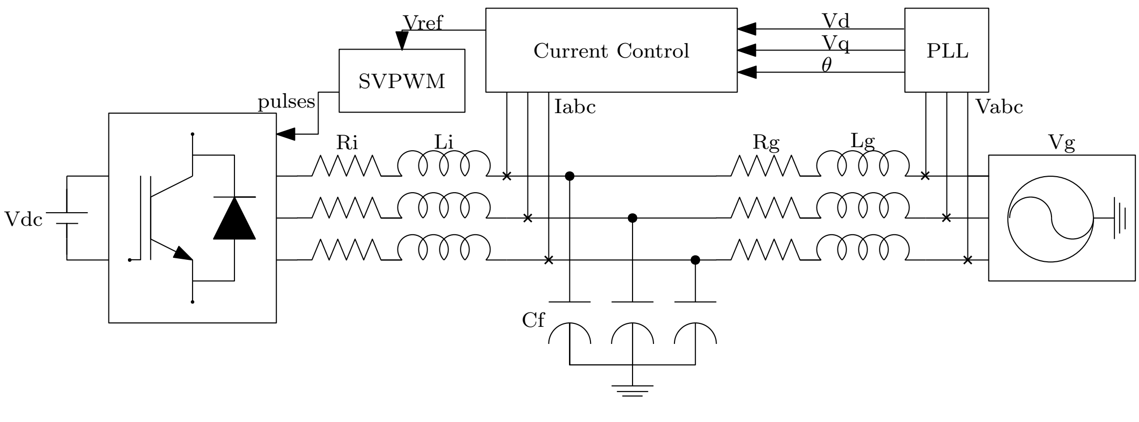

Figure 3.3: PI current control scheme used for grid-connected voltage source inverters.

The inverter currents and grid voltages are used in the current control loop. The grid voltages are used in the PLL. The grid voltages are transformed into dq-frame inside the PLL, which will, together with the angle θ, be used in the current control. The output of the current control block in Figure 3.3 is a reference voltage used in the SVPWM to control the switching of the inverter. The current control block varies, depending on which control scheme is used. In this section, the use of PI controllers for current control will be discussed.

The principle behind a PID controller is to read a sensor and compute a desired actuator output depending on the input. The input of a PID controller is the error between a measured- and a desired variable. The PID controller consists of a proportional-, an integral- and a derivative response, all summed up to compute the output.

The proportional component depends solely on the error. The error is subjected to a proportional gain, K_P. This gain determines the output response to the error input signal. If the proportional gain was set to 10 and the error is 5, the proportional output response would be 50. The proportional gain has great influence on the effectiveness of the controller, since it generally determines the speed of the control system response. If the proportional gain is increased beyond a certain threshold, the system will start to oscillate. These oscillations can get out of control and make the system unstable.

The integral component sums up the input error over time. Since the integral gain, K_I, is subjected to an integrator, the integral output has a slow response. The integral response will increase gradually over time, unless the input error is zero. The steady-state error is the final error between the desired- and measure input variables. The goal is to get the steady-state error to zero. In this thesis, integral windup is prevented by performing an external reset.

The derivative component is responsible for decreasing the output of the controller if the measured variables are changing rapidly. It is proportional to the rate of change of the measured variable. Increasing the derivative gain, K_D, will make the system react more strongly to changes and thereby increase the speed of the control system response. Since the derivative component is highly influenced by noise, most practical appliances use very little to no derivative gain. This is because the derivative component can make the system unstable if there is noise on the feedback signal or if the control loop rate is too slow.[20]

In this control method, the derivative component will not be used, wherefore the controller used is a conventional PI controller. The control scheme for the current control (Current Control block in Figure 3.3) is shown in more detail in Figure 3.4.

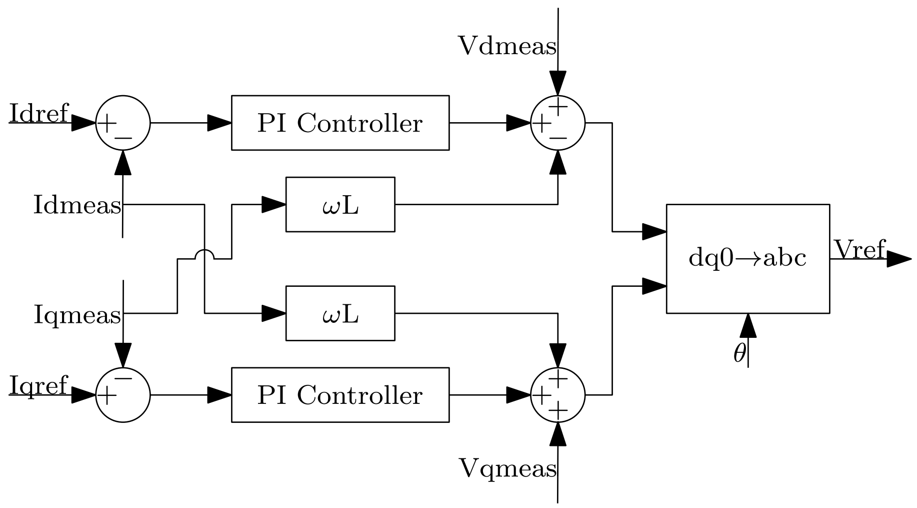

Figure 3.4: Current control using a PI controller in synchronous reference frame.

Figure 3.3 showed that the current measurements were taken from the inverter side of the filter. These current measurements are referred to as I_{meas}. They are transformed into dq-frame, making them much easier to control. The current measurements are subtracted from the current references, yielding the error that is fed into the PI controllers. The steady-state error should be as close to zero as possible. The output response of the PI controllers are added onto a voltage feed forward and a cross-coupling term. This will improve the performance of the PI controllers by compensating the couplings from the output filter. Using voltage feed forwards can heavily reduce overshoot. The resulting reference voltages are then transformed back to abc-frame and used as the input for the SVPWM.[7][21][19]

3.5.1 Tuning of the PI Controllers

To achieve the optimum performance of the PI controllers, they must be tuned correctly. The current control loop consists of a PI controller, the converter current, delay and the DC voltage. The block diagram for the current control loop can be seen in Figure 3.5.

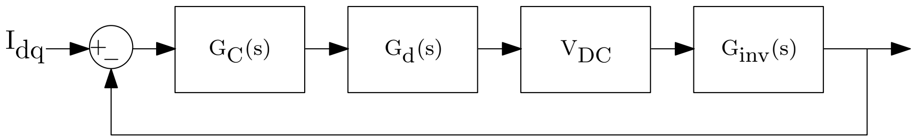

Figure 3.5: Block diagram for the current PI control loop.

The transfer function for the PI controller is:

$$G_{PI}(s) = K_P + \frac{K_I}{s} \tag{3.8}$$

The total controller delay consists of a processing delay and a PWM delay from the command signal to drive signals. The transfer function for the total delay can be expressed as:

$$G_d(s) = e^{-s\tau_d} \tag{3.9}$$

The time delay, τ_{d}, can have different values depending on the size of the delay. According to [22], the minimum delay is defined as $\tau_{\mathrm{d}} = \frac{\mathrm{T_s}}{2}$, medium delay as $\tau_d = \mathrm{T_s}$, and the maximum delay as $\frac{3\mathrm{T_s}}{2}$, where $\mathrm{T_s}$ is the sampling period. Normally this is equal to the switching frequency, but, depending on the switching frequency, this is not always the case since a too large sampling period can cause instability in the simulations. This is explained further in Chapter 4. Furthermore, the time delay chosen has great influence on the stability analysis of the system.

The transfer function for the converter current is defined as:

$$G_{inv}(s) = \frac{C_f L_g s^2 + C_f R_g s + 1}{f_a s^3 + f_b s^2 + f_c s + f_d} \tag{3.10}$$

Where:

$$\begin{aligned} f_a &= C_f L_{inv} L_g \\ f_b &= C_f L_{inv} R_g + C_f L_g R_{inv} \\ f_c &= C_f R_{inv} R_g + L_{inv} + L_g \\ f_d &= R_{inv} + R_g \end{aligned}$$

The system parameters for the electrical components etc. are located in Appendix A.1.

The DC voltage can be assumed to be constant as long as the capacitance is large or if DC voltage compensation is included in the control system.

The total system open loop transfer function can then be defined as:

$$G_{sys_{OL}}(s) = G_{PI}(s)G_d(s)V_{DC}G_{inv}(s) \tag{3.11}$$

Since there is a unity feedback, the closed loop system transfer function becomes:

$$G_{sys_{CL}}(s) = \frac{G_{PI}(s)G_d(s)V_{DC}G_{inv}(s)}{1 + G_{PI}(s)G_d(s)V_{DC}G_{inv}(s)} \tag{3.12}$$

The stability of the system is very important, primarily the closed loop system. Even if the open loop system is unstable, the closed loop system can still be stable. Normally when tuning, the open loop system is used for analysing the stability of the closed loop system. There are many different ways to analyse the stability of a system. Here, the step response, root locus, and Nyquist plots are all used.[22][17]

Bode plots could be used to give the information about the system stability, but Nyquist plots can handle right-half plane singularities. The Nyquist plot is most commonly based upon Cauchy's argument principle. The basic principle behind Cauchy's argument principle is to take a single point in the s-plane and plug it into the transfer function. This will result in a new complex number, which can then be mapped in a new arbitrary plane, here referred to as the w-plane. By plotting more and more points, as to conform a continuous line and connecting the line to itself, the Nyquist contour can be made. The contour refers to the self-connecting line in the s-plane. The Nyquist contour will generate a continuous self-connecting line in the w-plane, which is the Nyquist plot. The Nyquist plot contains the phase- and magnitude information for each of the zeros and poles of the system.

In order to make the following easier to explain, a more general transfer function is used:

$$G_{OL}(s) = G(s)H(s) \tag{3.13}$$

$$G_{CL}(s) = \frac{G(s)H(s)}{1 + G(s)H(s)} \tag{3.14}$$

The poles of the open loop transfer functions are values of s that cause the denominator to become 0, meaning the result will go to infinity. The open loop transfer function will be unstable if there is a pole in the right-half plane.

For the closed loop system, the poles are of interest. However, in order to divide by 0, 1+G(s)H(s) must be 0. The stability of the closed-loop system can therefore be analysed by looking at the zeros of 1+G(s)H(s). The Nyquist plot is made for G(s)H(s), the open loop system. The Nyquist plot encircles the origin depending on the amount of poles and zeros present in the Nyquist contour. If there is a surplus of 1 pole in the contour, the origin will be circled once in the counter-clockwise direction. Each encirclement in the counter-clockwise direction indicates that amount of surplus poles. If the encirclements are clockwise, there will be a corresponding surplus of zeros inside the contour.

This is very important and the fundamental principle behind the Nyquist plot. Since the contour is drawn in the entire right-half plane of the s-plane, this will reveal how many more poles than zeros are within the right-half plane. To analyse the stability of the closed loop system, the mapping must be done for $G(s)H(s)$ and then shift the entire plot to the right by 1. Since this can be difficult due to the complexity of the plot, the origin is instead shifted to the left by 1. This is why the encirclement of -1 is important when analysing the Nyquist plot. By calculating the open loop poles and looking at the encirclements of -1, the number of zeros in the right-half plane can be calculated as:

$$Z = N + P \tag{3.15}$$

Where Z is the number of zeros in the right-half plane, N is the number of clockwise encirclements of -1, and P is the number of open loop poles in the right-half plane. This means that in order to guarantee that there are no zeros in the right-half plane, there must be one counter-clockwise encirclement for every open loop pole in the right-half plane.[23][24]

The gains of the PI controller must now be determined. The experimental setup, see Section 5.1, is stable for a proportional gain of up to 20. The simulation in Section 4.1 remains stable beyond this proportional gain value of 20. However, since the simulations does not take disturbances into account, the lowest common denominator will be used for tuning.

For analysis purposes, several proportional- and integral gains will be analysed. Based upon the experimental setup, the proportional gain will be tested for 10/15/20, whereas the integral gain will be tested for 1500/2000/2500. According to [25], the smallest proportional gain is paired with the largest integral gain, the largest proportional gain is paired with the smallest integral gain, and the two medium gains are paired with each other. This is further used and elaborated upon in the Fuzzy-Logic controller part, Section 3.7.

As mentioned previously, the amount of delay is pivotal to analyse the system stability. The minimum delay was defined to be $\tau_d = \frac{\mathrm{T_s}}{2}$ in [22]. The delay can be difficult to determine and it will only be an estimate. Furthermore, the delay depends on the sampling time chosen. By altering the sampling time, the stability of the system will change accordingly. Since it is known, from the simulations and experimental results, that the system is stable for $\mathrm{K_P} = 20$ and $\mathrm{K_I} = 1500$, this will be used to better approximate the delay of the system. To begin with, the minimum delay defined earlier will be used and the system stability will be evaluated. It is important to note that the model is being evaluated as a continuous-time model with delay. The mathematical constant e is irrational, meaning it cannot be written as a quotient of integers. This will render the root locus method useless for values of $\tau_\mathrm{d} > 0$. Most difficulties, when dealing with time-delay systems in continuous time, arises from the infinite dimensions of the delay element. Therefore, it is necessary to make a rational approximation of the delay element in order to determine the poles of the system.[26]

The Padé approximation method is used to approximate the delay element. The MATLAB function *pade* is used, where rational models are used to approximate time delays. The delay is approximated using a rational transfer function that is using Padé approximation formulas.[27]

The root locus can now be plotted for the open loop transfer function, Equation 3.11, which can be found in Appendix A.2. The root locus shows that there are no poles in the RHP. There is a pole at the origin, meaning that the open loop system is marginally stable. To determine if the closed loop system is stable, the open loop transfer function (without Padé approximation) will be plotted in the Nyquist plot (see Appendix A.2). The Nyquist plot shows that there are two clockwise net encirclements of -1, resulting in two zeros in the RHP of the closed loop system. This clearly indicates that the closed loop system is unstable.

Remember that the system is known to be stable in both the simulations and the experimental setup with $K_P = 20$ and $K_I = 1500$. The limit for K_P before the system becomes unstable in the experimental setup is around 24, but, to allow for unaccounted disturbances and margins, a gain of 20 is used. The estimate of the time delay proved to be incorrect, wherefore a new, lower time delay must be used. Naturally, you cannot choose the time delay as you please, but the initial assumption of the time delay proved to be incorrect. The gain- and phase margins are critical to ensure a stable performance under varying conditions. Assessing the requirements of the margins is a compromise between performance and stability. Lower margins are often tied to better performance, but can also lead to instability. The requirements for the stability margins in this thesis are determined to be 10 dB for the gain margin and 60° for the phase margin.[28]

By trial and error, the new appropriate time delay estimate is determined to be $\tau_d = \frac{T_s}{20}$. The same procedure is done as previously; Padé approximation of the time delay, root locus of the open loop poles and Nyquist plot of the open loop system to analyse the closed loop stability of the system. The root locus of the open loop transfer function can be seen in Figure 3.6.

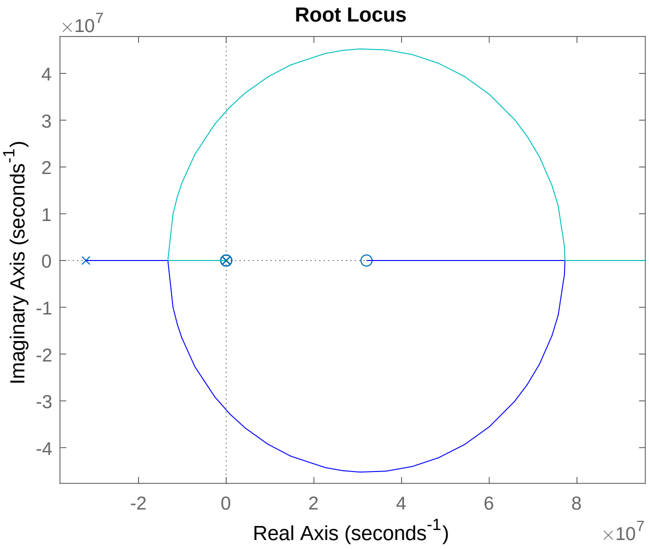

Figure 3.6: Root locus for open-loop system using Padé approximation with $K_P = 20, K_I = 1500, \tau_d = T_s/20$.

A zoomed in version around the origin can be found in Figure A.5, Appendix A.3. The open loop system is still marginally stable due to the pole at the origin. The Nyquist plot for the system can be seen in Figure 3.7.

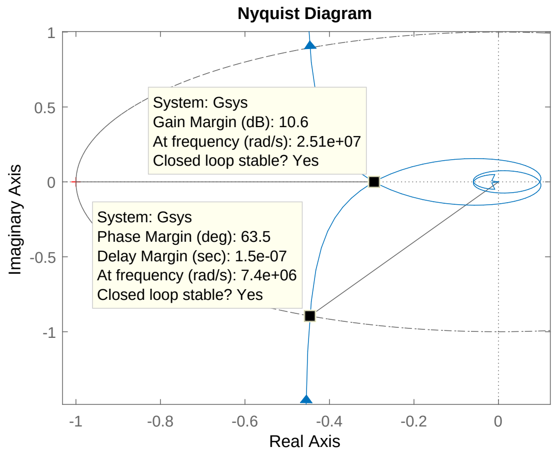

Figure 3.7: Zoomed in Nyquist plot for open-loop system using Padé approximation with $K_P = 20, K_I = 1500, \tau_d = T_s/20$.

This plot is zoomed in around the origin, since the encirclements of -1 cannot be seen in the full plot. The full plot can be found in Figure A.6, Appendix A.3.

The Nyquist plot shows that there are no net encirclements of -1. With no poles in the RHP of the open loop system and no encirclements of -1, the closed loop system is asymptotically stable. The gain margin is 10.6 dB. It's determined by the distance between the crossing of the real axis and -1. The phase margin is 63.5°, determined by the angle between the real axis and the crossing of the unit circle. The step response of the closed loop system is shown without Padé approximation in Figure 3.8. It is slightly underdamped, with a very small overshoot and a rapid rise- and settling time.

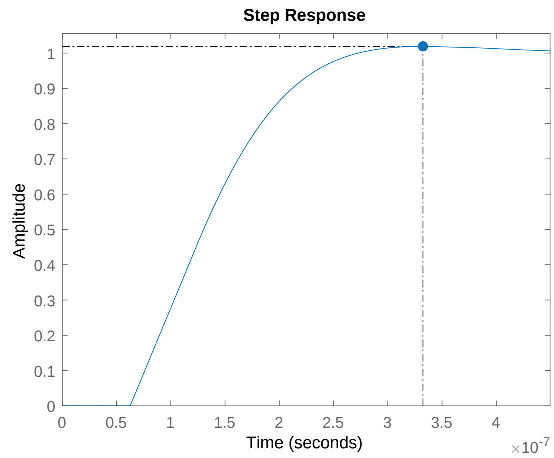

Figure 3.8: Step response of closed-loop system with $K_P = 20, K_I = 1500, \tau_d = T_s/20$.

It is now desired to evaluate the system stability of the scenarios for $\mathrm{K_P} = 15; \mathrm{K_I} = 2000$ and $\mathrm{K_P} = 10; \mathrm{K_I} = 2500$. These instances will be used to compare the performance of the controller and they will furthermore be used as part of the Fuzzy Logic controllers in

Section 3.7. The root locus, Nyquist plots and step responses of both scenarios will not be shown here, but can be found in Appendix A.4.

To start off with, the analysis will be performed for $K_P = 15$ and $K_I = 2000$. As can be seen in Figure A.7, the root locus has not changed much, compared to the previous. The open loop system is still marginally stable with a pole in the origin and no poles in the RHP. The Nyquist plot looks identical to the previous, but zooming in around the origin shows that the stability margins have increased. By looking at Figure A.8, it can be seen that the gain margin has now increased to 13.1 dB, whereas the phase margin has increased to 70.1°. With no open loop poles in the RHP and no net encirclements of -1, the closed loop system is still asymptotically stable. The step response has now become overdamped (Figure A.9).

By decreasing the proportional gain even further, the stability margins become even larger. For $K_P = 10$ and $K_I = 2500$, the root locus, Nyquist plot and step response is also to be found in Appendix A.4. The root locus in Figure A.10 has changed insignificantly, still being marginally stable for the open loop system. The Nyquist plot, Figure A.11, gives a gain margin of 16.6 dB and a phase margin of 76.7°. This further confirms that the stability margins increases as the proportional gain decreases. The step response in Figure A.12 is still overdamped, but with an even faster response time.

An overview of the stability margins for each of the different scenarios can be seen in Table 3.1.

	Gain Margin	**Phase Margin**	**Step Response**
$K_P = 20$ $K_I = 1500$	10.6 dB	63.5°	Underdamped
$K_P = 15$ $K_I = 2000$	13.1 dB	70.1°	Overdamped
$K_P = 20$ $K_I = 1500$	16.6 dB	76.7°	Overdamped

Table 3.1: Comparison of stability margins for closed-loop system with different proportional- and integral gains.

These scenarios will be simulated in Section 4.1 and experimentally tested in Section 5.1.

3.6 PR Control

In the PI current control scheme, synchronous reference frame was used due to its simplicity and relative effectiveness. However, it has some drawbacks such as potential distortion of the line current due to background harmonics introduced along the voltage feed forward path, in case the grid voltage is distorted. This distortion can trigger LC resonance, especially when using an LCL filter. PI control also leads to steady-state current error in both phase and magnitude, wherefore unsatisfactory harmonic compensation performance is expected. The phase angle of the grid voltage is a necessity due to the transformation to dq-frame.

Another method that has gained much popularity in current control of grid-connected systems is the proportional resonant (PR) controller in stationary reference frame, $\alpha\beta$-frame. The phase angle of the grid voltage is no longer necessary and the overall complexity of the control system lowers. PR controllers are less sensitive to noise and error in synchronisation and, most importantly, they introduce an infinite gain at selected resonance frequencies, thereby eliminating the steady-state error at those frequencies. The control scheme is very similar to the PI control scheme, but without the voltage feed forwards and coupling terms which are proved unnecessary by [29]. PR controllers also introduce a simple cascading of harmonics compensation compensators for eliminating selected low-order harmonics.[30][7] The PR control scheme is shown in Figure 3.9.

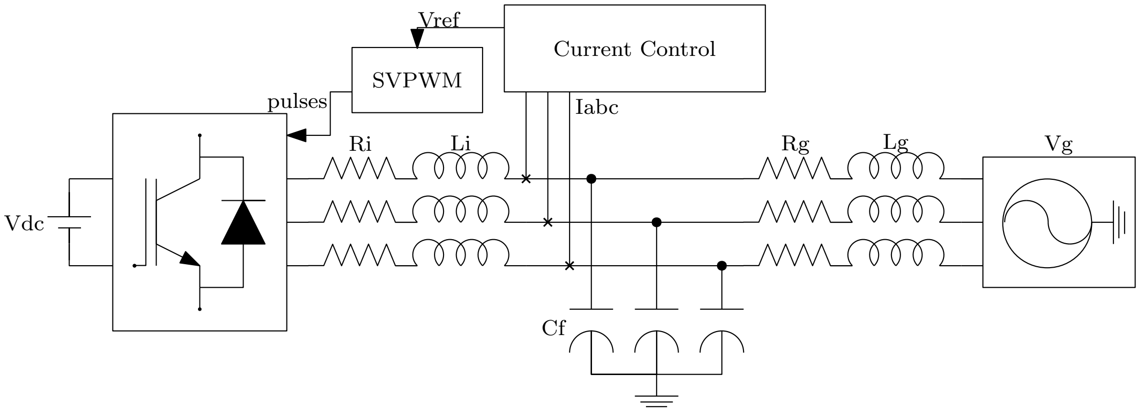

Figure 3.9: PR control scheme used for grid-connected voltage source inverter.

The most substantial change is the removal of the phase-locked loop. Since the phase angle of the grid voltage is no longer needed for the reference frame transformation, it's only used to observe the grid frequency and for the harmonic compensation, Section 3.4. The current measurements are still taken from the inverter side of the LCL filter. The inverter currents are transformed to $\alpha\beta$-frame, which is the reference frame used in this control scheme.

The principle behind a PR controller is much like the PID controller. It is fed with a sensed signal and computes a desired actuator output depending on the input. PR controllers with two interconnected integrators are widely used because of their simple frequency adaptation. The transfer function for a PR controller tracking a harmonic of order h can be expressed as:

$$G_{PR_h}(s) = K_{P_h} + K_{I_h} \frac{s}{s^2 + h^2\omega_0^2} \tag{3.16}$$

Where ω_0 is the fundamental grid frequency of the grid. The infinite gain in open loop at the resonant frequency $h\omega_0$ ensures optimal tracking for components oscillating at that resonant frequency, when implemented in closed loop. Multiple resonant controllers can be added in parallel to compensate for certain harmonics. Figure 3.10 shows how the individual gain K_P is added separately and uniformly for all fundamental frequencies.

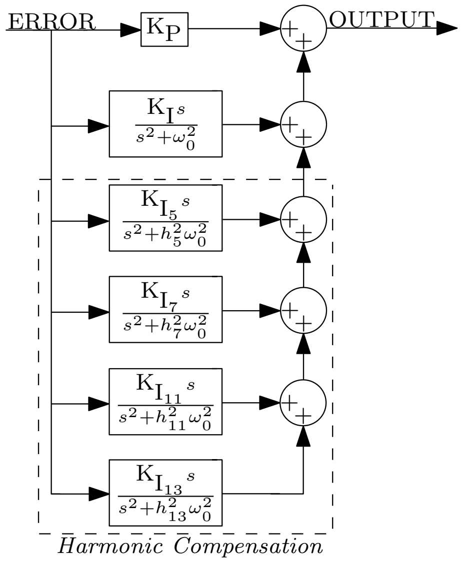

Figure 3.10: Block diagram of a PR controller with additional harmonic compensation.

The figure indicate that the 5^{th}, 7^{th}, 11^{th} and 13^{th} harmonics are compensated for. The transfer function in Equation 3.18 can be decomposed in a control scheme for the PR controller utilising two integrators. In digital devices, continuous domain schemes cannot be used. This is stated again in Chapter 4, since all models are implemented in discrete domain. Tuning and evaluating the system stability is simpler in continuous domain, which is why it is being done. However, discretization often introduce certain inaccuracies that is important to be aware of.

Discretizing from continuous domain will lead to a displacement of the resonant poles. This will result in a variation of the frequency of which the infinite gain is located, based upon the expected resonant frequency, and can potentially lead to a large steady-state error. Furthermore when implementing resonant controllers, the system delay may cause instability as the resonant frequency and sampling period increase. The latter can be compensated for with a delay compensation scheme by introducing a phase lead. The optimum target leading angle is in most cases found from the phase lead of two samples. However as proved in [31], a significant amount of the phase delay is not efficiently compensated for this way. This reduces the phase margins and introduces abnormal peaks in the closed loop frequency response. Since this error is added onto the inaccuracy between the estimated- and the actual phase lead, the stability of the system worsens even more. For these exact reasons, phase compensation will not be used in this thesis.

The resonant control scheme in continuous domain is comprised of a direct integrator and an integrator in feedback. Figure 3.11 shows the discrete scheme of the resonant controller. The direct integrator is discretized using the forward Euler method, whereas the feedback integrator is discretized using the backward Euler method.

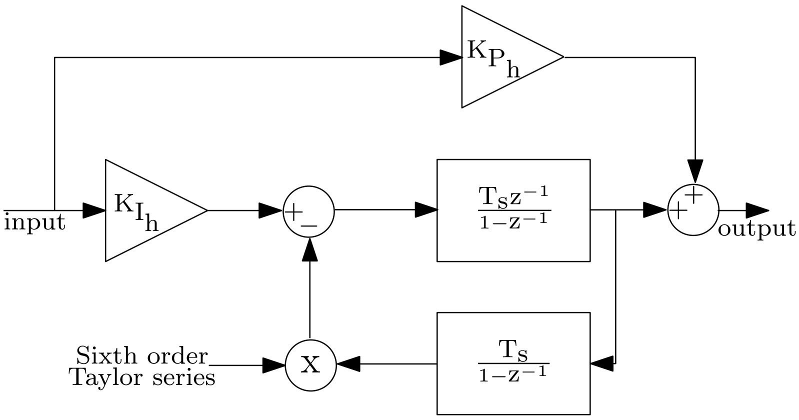

Figure 3.11: Proposed discrete scheme of a PR controller.

A precise resonant pole placement is paramount for achieving perfect tracking. The pole placement is approximated using a sixth order Taylor series:

$$h^2\omega_0^2 \rightarrow h^2\omega_0^2 - h^4\frac{\omega_0^4 T_s^2}{12} + h^6\frac{\omega_0^6 T_s^4}{360} \tag{3.17}$$

The PR current control scheme resembles that of the PI control scheme. As was noted in Figure 3.9, the PLL block is no longer necessary when controlling in stationary reference frame. Additionally, there are some changes made to the Current Control block, which can be seen in Figure 3.12.

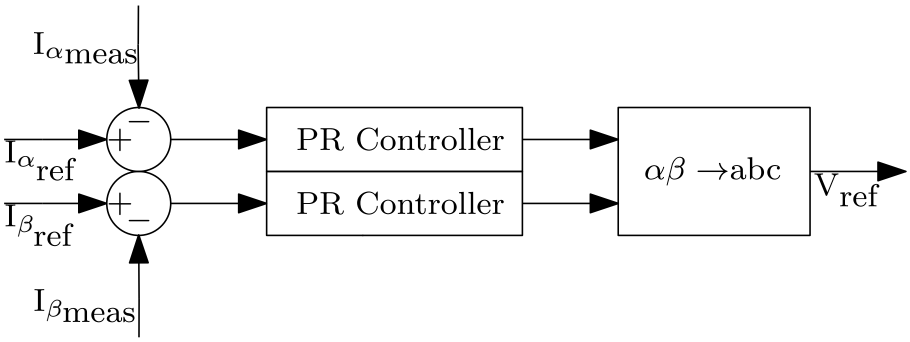

Figure 3.12: Current control using PR controllers in stationary reference frame.

The control scheme has been simplified substantially by removing the need for voltage feed forwards and cross-coupling terms. The phase angle of the grid voltage is also no longer required for the reference frame transformations. The error between the measured- and reference currents is fed into a PR controller. There is one for each frame component. The actuator output of the controllers are transformed back to abc-frame, constituting the reference voltage being fed into the SVPWM.[7][30][31]

3.6.1 Tuning of PR Controllers

As for the stability analysis of the PR current control scheme, the method used is very similar to that of the PI current control scheme. The block diagram for the system was shown in Figure 3.5, where the PI controller is now replaced with a PR controller. The transfer function for the PR controller consists of the transfer function for the fundamental controller and the transfer functions for each of the harmonic compensators. The overall transfer function for a PR controller compensating for the 5^{th}, 7^{th}, 11^{th} and 13^{th} harmonics can be seen in Equation 3.18.[31][7]

$$G_{PR}(s) = K_P + K_I \frac{s}{s^2 + \omega_0^2} + \sum_{h=5,7,11,13} K_{I_h} \frac{s}{s^2 + h^2\omega_0^2} \tag{3.18}$$

Here, h is the compensated harmonic and ω_0 is the fundamental grid frequency. The integral gains $\mathrm{K_I}$ and $\mathrm{K_{I_h}}$ are the integral gain for the fundamental controller part and the integral gains for the harmonics, respectively. The proportional gain, $\mathrm{K_P}$, and the integral gain, $\mathrm{K_I}$, are kept at the same values as with the PI control scheme. $\mathrm{K_P}$ will therefore be tested for values of 10/15/20, whereas $\mathrm{K_I}$ will be set to vary between 1500/2000/2500. The reason behind this is again to prepare the implementation of a Fuzzy Logic controller in the PR current control scheme. For the same reason, the low value of the proportional gain is matched with the high value of the integral gain and vice versa, as it was done in Section 3.5.1 and [25]. The integral gains for each harmonic, $\mathrm{K_{I_h}}$, is set to 1000.

The system transfer function still consists of the transfer functions for; the delay, the inverter current, the DC voltage and the controller. The feedback for the closed loop system is still negative unity feedback, meaning the open loop- and closed loop transfer functions are defined as:

$$G_{sys_{OL}}(s) = G_{PR}(s)G_d(s)V_{DC}G_{inv}(s) \tag{3.19}$$

$$G_{sys_{CL}}(s) = \frac{G_{PR}(s)G_d(s)V_{DC}G_{inv}(s)}{1 + G_{PR}(s)G_d(s)V_{DC}G_{inv}(s)} \tag{3.20}$$

The open loop transfer function is now analysed in root locus to determine the stability of the closed loop system. Padé approximation of the processing delay is still performed in order to be able to plot the root locus. Since the root locus looks similar to that of the PI control system, it has been moved to Appendix A.5. The root locus shows that there are several poles on or very near the imaginary axis, but no poles are in the RHP. Therefore, the open loop system can be considered as marginally stable.

Moving on to the Nyquist plot, Figure A.15 and A.16 in Appendix A.5 indicate no encirclements of -1. MATLAB is not very good at plotting the Nyquist plot when poles are on the imaginary axis of the open loop system, meaning the lines forming a cross in Figure A.15 extend far out. However, it does show the accurate gain- and phase margins, which, according to Figure A.16, are 10.6 dB and 63.5° respectively.

The bode plot was not evaluated for the PI control scheme, since the Nyquist plot supplied all information about the stability of the system. As for the PR controller, the bode plot can show interesting information about the frequency response of the system, such as the "infinite" gains around the harmonic frequencies. The bode plot for the open-loop system transfer function can be found in Figure 3.13

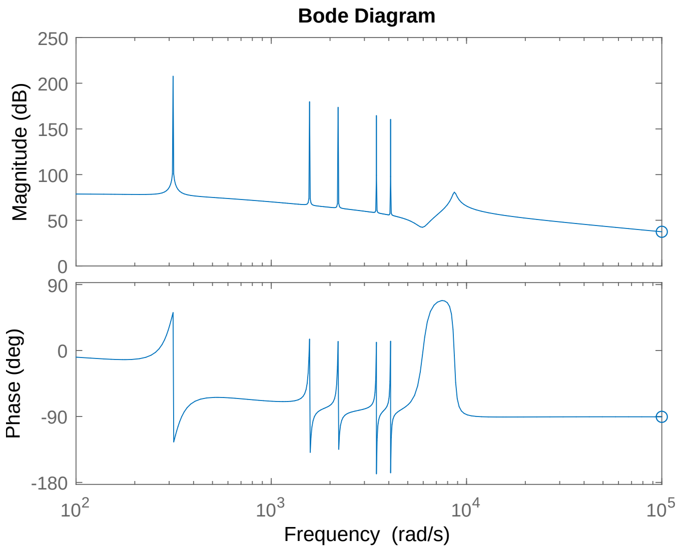

Figure 3.13: Bode plot for PR control scheme compensating 5^{th}, 7^{th}, 11^{th} and 13^{th} harmonics for $K_P = 20$ and $K_I = 1500$.

Lastly, the step response of the closed loop system is evaluated and depicted in Figure A.17 in Appendix A.5. It indicates very satisfactory behaviour, since the rise- and settling time are both extremely rapid, overshoot is around 2 % and the steady-state error is 0.

The other scenarios, where the proportional- and integral gains are varied, must also be evaluated. A zoomed in root locus, -Nyquist plot, -bode plot and step response are depicted in Appendix A.5. The gain- and phase margins increase proportionately to the decrease in proportional gain. A comparison between the stability margins for the different scenarios is shown in Table 3.2.

	Gain Margin	**Phase Margin**	**Step Response**
$K_P = 20$ $K_I = 1500$	10.6 dB	63.5°	Underdamped
$K_P = 15$ $K_I = 2000$	13.1 dB	70.1°	Overdamped
$K_P = 20$ $K_I = 1500$	16.6 dB	76.7°	Overdamped

Table 3.2: Comparison of stability margins for proportional resonant closed-loop system with different proportional- and integral gains.

It should be noted that the stability margins for the different PR control scenarios are identical to their PI control counterparts. This makes sense, since the proportional- and integral gains are the same and furthermore shows that the additional harmonic compensation in the PR controllers have not altered the theoretical stability of the system.

3.7 Fuzzy Logic Controller

The two previous sections opened up for the use of fuzzy logic controllers. The principle behind fuzzy logic is to model logical reasoning with vague or ambiguous statements. The concept can handle partial truths, where the truthfulness of a particular statement can vary between completely true and -false. The so-called truth variable stipulates the degree of truth to a statement. Fuzzy logic resembles human reasoning in that certain things cannot be categorized as entirely true or -false.[32]

The advantages of using fuzzy logic are manifold. It is conceptually easy to understand, since it is an intuitive approach without extensive complexity. Most things are imprecise, even on close inspection, and the flexibility of fuzzy logic creates a tolerance for inexact data.[33]

In control systems, the point of fuzzy logic is to map an input space to an output space. Fuzzy systems do not necessarily replace conventional control techniques, but can be blended with them. The whole concept begins with fuzzy sets. Fuzzy sets have no exact defined boundary and contains elements of only partial degree of membership. An example of this is how one would define if a person is tall. There is no precise boundary that, e.g., all people above 1.8 meters are tall. One might postulate that all everyone above 2 meters is clearly tall, but where is the lower boundary located? Individual perception, geographical location and age all affect the definition of tall. Yes/no logic is no longer as useful, since there is no definite truth to the statement. Fuzzy logic makes it possible to answer a yes or no question with a non precise yes or no answer. This way of reasoning is common in humans, which is why it resembles human reasoning.

The truth value varies between 0 and 1, where 0 is completely false and 1 is completely true. However, it also permits values in between, meaning something can be partially true or false. To use the previous example, the truth value of a person with a height of 1.8 meters can be 0.8. He is for the most part tall (taller than the average e.g.), but he is not completely tall.

Membership functions are curves that represent how each point in the input space correlates to a membership value (truth value). The membership function can be defined as an arbitrary curve that is chosen based on simplicity and efficiency. The simplest of which are formed using straight lines, i.e. triangular- and trapezoidal membership functions. They can also be based upon the Gaussian distribution curve, achieving smoothness and non-zero capabilities at all points for the membership values. In case that the truth values are better represented with asymmetric membership functions, sigmoidal- or polynomial based curves can be used. However, expansive membership functions are not required for good performance of a fuzzy interference system, wherefore the simple membership functions can often do what is required.

Rules are used to correlate the membership values to a specific output. The ruleset is comprised of logical operators as well as premise and consequence. The size of the ruleset expands with more inputs and outputs. The type of logical operators used are often *AND*, *OR* and *NOT*. This is most easily explained with some examples.

Imagine being at a restaurant and need to determine the amount of tip to give. It is determined by the service and the food, i.e. two inputs. If both the food and service were good, then the tip will be average. Maybe the food was spectacular, but the service was mediocre. Food is weighed heavier in this scenario, leading to an above average tip. An extra consequence, output, could be added in the form of recommendation. Even if the tip was above average, the restaurant would not get a recommendation due to its mediocre service. All these rules can be adjusted accordingly so that good performance of the fuzzy interference system is achieved.

But what is a good tip? How you define the output depends on the type of fuzzy logic system used. There are two types; Mamdani and Sugeno. Mamdani is most commonly used and was the first of the two to be proposed. The output of the Mamdani interference system is based upon fuzzy sets, just like the input. The output aggregate is comprised of a range of output values, but, since it is desired as a single number, it must be defuzzified. There are different methods to defuzzify the aggregate output, where the most popular is the centroid calculation, returning the center of area under the output aggregate.

Sugeno type interference systems are different for the output membership functions. They are either linear or constant. The advantage of the Sugeno is that they are less resource intensive and works well with PID control systems.[34][35][36]

The input membership functions of both types of fuzzy logic controllers are identical to each other. It is common to have two inputs, where the first is the error between the measured- and the reference current in grid-connected power systems. This error is divided into categories; negative large (NL), negative small (NS), zero (Z), positive small (PS) and positive large (PL). The five categorizations are also used for the second input, which is the change of error. By taking the derivative of the error, the system response should become more resilient and thereby reduce the overshoot.

3.7.1 Tuning of Fuzzy Logic Controllers

Because of certain difficulties with the experimental setup, only the Sugeno fuzzy logic controller will be used and tested in this thesis. The difficulties with the experimental setup is explained in detail in Chapter 5. One of the consequences of this is that the Fuzzy Logic Toolbox cannot be implemented in the experimental setup, wherefore a fuzzy logic controller must be build from scratch. In order to evaluate the performance of this fuzzy logic controller, it will be compared to the performance of the Sugeno Fuzzy Logic Toolbox in Section 4.3.

The first order of business is to tune the membership functions for the fuzzy logic controller. The Fuzzy Logic Toolbox cannot run in real time since it is too computational expensive. To ensure that the fuzzy logic controller can run in real time, it must be computationally inexpensive. As mentioned in the previous section, triangular- and trapezoidal membership functions are the simplest, wherefore they are used to design the controller. The membership functions are tuned differently depending on the control scheme, whether it is for the laboratory or the simulations.

To illustrate how they are designed, the experimental PI control setup will be used as an example. The goal here is to develop a fuzzy logic controller that controls the proportional- and integral gains of the PI controllers. The fuzzy logic controllers are implemented into each frame, as shown in Figure 3.14.

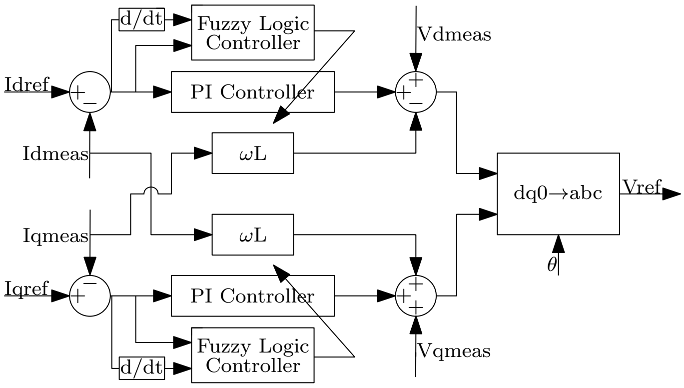

Figure 3.14: Current control using fuzzy logic controllers to control PI controllers in synchronous reference frame.

The overall control scheme remains unchanged. The fuzzy logic controllers are added concurrent to the PI controllers. The outputs of the fuzzy logic controllers are the proportional- and integral gains that are fed into the PI controllers. The gains will therefore vary depending on the amplitudes of the error and change in error.

The current PR control scheme utilising fuzzy logic controllers can be found in Figure 3.15.

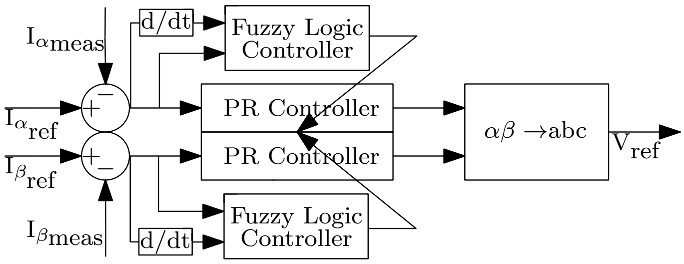

Figure 3.15: Current control using fuzzy logic controllers to control PR controllers in stationary reference frame.

The scheme is different between the simulations and the laboratory, since the voltage feed forwards cannot be removed in the experimental setup. Whenever they are removed, the inverter instantly trips. This is further elaborated upon in Chapter 5.

The membership functions will be tuned according to the errors and changes in errors. Since the fuzzy logic controllers are desired to control the gains of the PI controllers, the errors and change in errors are extracted from the conventional PI control scheme. The errors in each frame from the experimental setup can be seen in Appendix A.6, Figures A.26 and A.27. Since they are very similar, the membership functions will be tuned according to the d-frame and used in both frames. Similarly, the changes in errors can be found in Figures A.28 and A.29. These also look similar and the membership functions are also only tuned based on one of the frames.

The membership functions are based upon [25] and [37], where the locations of the triangle- and trapezoidal corners are the ones that are tuned. The membership functions for both the error and the change in error in the experimental setup can be seen in Figure 3.16.

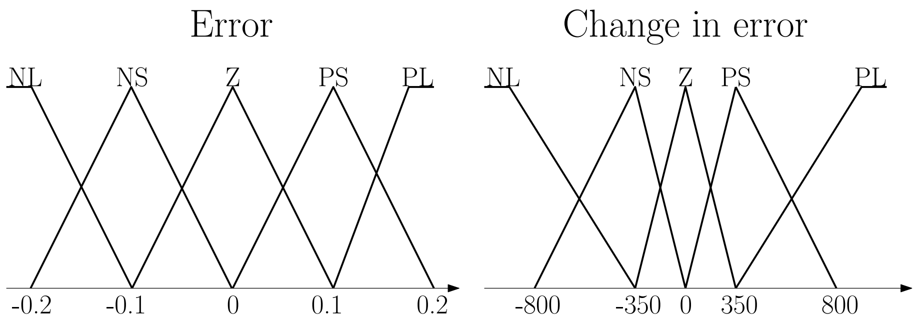

Figure 3.16: Membership functions for error and change in error for PI control scheme in experimental setup.

As mentioned earlier, there are five categories; negative large (PL), -small (NS), zero (Z), positive small (PS), and -large (PL). The principle behind these can be illustrated with an example; an error of -0.16 will produce outputs greater than 0 for the membership functions NL and NS. The corresponding y-value for NL is approximately 0.4, whereas it is around 0.6 for NS. Since the value of NS is larger than NL, the input value of -0.16 will be categorised as NS. The reason why NL and PL are trapezoidal is because they must extend to infinity. To reduce computational resources, they extend to very large negative- and positive values, respectively, ensuring that all probable inputs can be categorised.

The fuzzy logic controller must also be designed for the PR control scheme. Since the error- and change in error values are different in $\alpha\beta$-frame than in dq-frame, they must be tuned separately. The membership functions, experimental error measurements and -change in error measurements for the stationary reference frame can all be found in Appendix A.6.

After the two inputs have been categorised, the rulseset is used to determine the output for the fuzzy logic controller. The ruleset is taken from [25] and can be seen in Table 3.3.

		Error (e)							Error (e)				
Output K_P		NL	NS	Z	PS	PL	**Output K_I**		NL	NS	Z	PS	PL
	NL	L	L	M	M	S		NL	S	S	M	L	L
	NS	L	L	M	S	S		NS	S	S	M	L	L
Change in error (Δe)	Z	M	M	M	M	M	Change in error (Δe)	Z	M	M	M	M	M
	PS	S	M	M	M	L		PS	L	L	M	S	S
	PL	S	S	M	L	L		PL	L	L	M	S	S

Table 3.3: Ruleset for fuzzy logic controller outputs K_P and K_I based upon the membership functions for inputs e and Δe.

The output values S, M and L stand for small, medium and large, respectively. Remember that only the Sugeno fuzzy logic controller is used in this thesis, meaning there are no output membership functions, just constant values. For the integral gain, K_I, small is set to 1500, medium to 2000 and large to 2500. These values are consistent throughout all simulations and will not be changed. The proportional gain, K_P, will be adjusted depending on the simulation. In the baseline experimental setup (explained in Chapter 5), the maximum possible proportional gain before instability is 24. K_P=20 is the maximum recommended value in this baseline. The medium value of K_P will be set to 10/15/20, as was the gains chosen for the PI control scheme in Section 3.5. The values of S and L for

K_P are set to M-1 and M+1, respectively. Values of M±2, M±3 and M±4 was tested, but using M±1 was found to achieve the least amount of total harmonic distortion (THD).

The influence of using the change in error as a second input can be seen in the ruleset. If both inputs are negative, the output gains are set to L, since higher gains will result in quicker response time. However, if one input is negative and the other is positive, the gains are set to small. This is to account for the momentum of the signals and will reduce overshoot as the error goes to 0. This principle is the advantage with fuzzy logic control over conventional controllers.

Section 4

Simulations

Each control scheme listed in Chapter 3 is simulated in Simulink. The purpose of the simulations is to evaluate the performances of the control schemes. After the control schemes have been simulated, they will be tested in the laboratory, see Chapter 5. To summarise, the PI control-, PR control, fuzzy logic PI control-, and fuzzy logic PR control schemes will all be simulated. Furthermore, additional harmonic compensation outside the 5^{th} and 7^{th} harmonics will be tested. In the experimental setup, a baseline has been provided which is essentially the PI control scheme.

This baseline experimental setup will be the basis of all simulations. The baseline is very restricted and many decisions will be made with this restriction in mind. In the baseline, harmonic compensation is made for the 5^{th} and 7^{th} harmonics. The harmonic compensation will be extended further to include the 11^{th} and 13^{th} harmonics. Extending the harmonic compensation even further would make sense in the theoretical testing, but since the experimental setup becomes unstable by compensation beyond the 13^{th} harmonics, only up to and including the 13^{th} harmonics is simulated and tested.

All simulations are run in discrete time, since it allows for real time implementation in the experimental setup. A sampling time, T_s, of $1.25 \cdot 10^{-06}$ is used. Setting the sampling time to the same value as the switching frequency sampling time will lead to instability in the simulations, wherefore this value is chosen. The simulations will run for 0.5 seconds. A step input for increasing P_{ref} at 0.3 seconds can be tested to evaluate the dynamic response of the systems.

Figures of the simulations can all be found in Appendix A.7. The simulations are all comprised of the same overall components. As can be seen in A.31, the simulations all consist of the grid-connected voltage source inverter electrical system, the current control system, and scopes for evaluating the results.

The grid-connected voltage source inverter block can be seen in Figure A.32. A Three-Phase Source is used to simulate the grid. The grid voltage is lower than the DC voltage to ensure the correct direction of flow.

The Current Control System block is where the simulations differ from one another. The block contains common components that are the same throughout all simulations, one of which is the phase-locked loop. The block diagram of the phase-locked loop in the simulations can be seen in Figure A.33, Appendix A.7.

The harmonic compensation block is altered slightly throughout the simulations. The structure of the harmonic compensator in the simulations was shown back Figure 3.2. As can be seen, the values can be changed depending on which harmonics need compensation. The 5^{th} and 7^{th} are compensated in all simulations, due to them being compensated in the baseline experimental model, whereas the 11^{th} and 13^{th} harmonics are compensated additionally in some simulations.

The Reference Power Calculations- and Reference Frame Transformations blocks vary depending on the reference frame used for that particular control scheme. The Reference Power Calculations block can be seen in Appendix A.7, Figure A.34, where the power calculations within each box were explained in Section 3.3. As for the Reference Frame

Transformations block, it is used to transform between the three frames; abc-, dq0-, and $\alpha\beta 0$-frame.

The SVPWM is consistent throughout all simulations as well. The PWM generator used is the PWM Generator (2-level) Three-phase bridge (6 pulses) from the Simscape library.

The Current Control blocks are the ones that will change depending on the control scheme used. They will each be shown, elaborated and analysed in the next sections.

4.1 PI Control

The PI control is also referred to as the baseline. As is explained in Chapter 5, this is the baseline model used in the experimental setup. The baseline compensates for the 5^{th} and 7^{th} harmonics and this is the baseline must be evaluated and improved in this thesis.

The Current Control block for the PI control scheme simulation can be seen in Figure A.35, Appendix A.8. From here, the values of K_P, K_I, P_{ref} and Q_{ref} can be changed. Furthermore, harmonic compensation can be enabled and disabled together with the step response increase in P_{ref}. By default, the step increase is set to 1000 W at 0.3 seconds, but can be changed accordingly in the Reference Power Calculations block.

The current control is separated into two separate frames; d- and q-frame. The content of these two blocks can be found in Appendix A.8, Figures A.36 and A.37 respectively. The current control includes conventional PI controllers with voltage feed forwards and coupling terms, as described in Section 3.5.

The simulation is run for the three different scenarios previously described; K_P=10/15/20 and K_I=2500/2000/1500. The power reference values will be kept constant, meaning P_{ref} is set to 2200 W and Q_{ref} is 0 VAR. Harmonic compensation will also be enabled for the 5^{th} and 7^{th} harmonics in order to compare with the baseline experimental results later on.

The first simulation that is performed is with $K_P = 20$ and $K_I = 1500$. The grid voltage-, grid current-, and grid frequency measurements are shown in Figure 4.1 for the last 3 cycles.

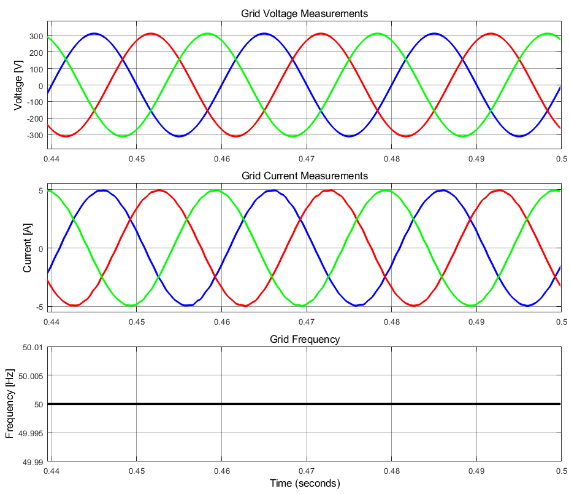

Figure 4.1: Grid voltage, -current and -frequency measurements for PI control scheme simulation with $K_P = 20$ and $K_I = 1500$.

Since the grid is simulated using a three-phase source, the grid voltage is naturally stable with no THD. Furthermore, the phase-locked loop functions as intended, keeping the frequency at a stable 50 Hz. The current injected into the grid is compared to the reference current from the reference power calculations in Figure 4.2.

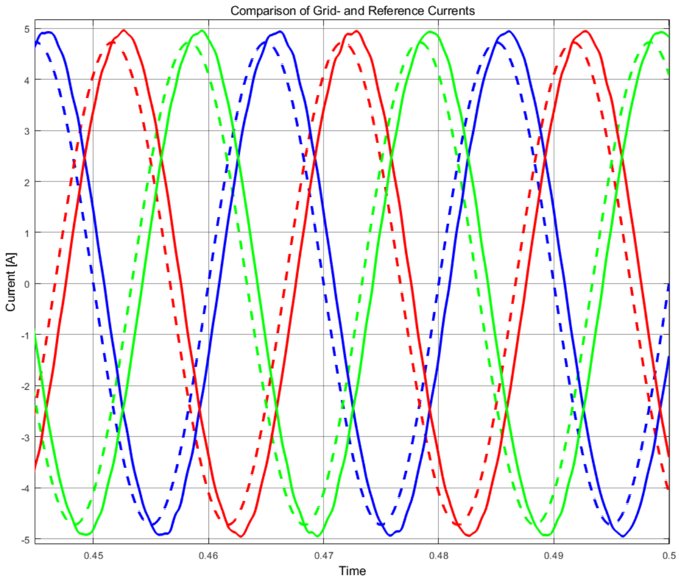

Figure 4.2: Comparison of the grid- and reference currents for PI control scheme simulation with $K_P = 20$ and $K_I = 1500$.

The amplitude of the waves are proportional to the active power requirement ($P_{ref} = 2200$ W). There are some distortions on the grid currents, which must be analysed to determine the amount of THD on the signals. There is a noticeable lag between the grid- and the reference currents, which is caused by the control loop. A lead compensator could decrease the significance of this lag, but it will not be discussed in this thesis. The amount of THD on the grid currents can be analysed using the Fast Fourier Transform (FFT) integrated into the powergui block of the simulation. The FFT is taken over 11 cycles to get a representative average. The THD for phase a is 0.61 %, and 0.62 % for both phase b and -c. An overview of all the simulation results can be found at the end of each section.

The simulation parameters will now be changed and tested for the two other scenarios; K_P=15 and K_I=2000, and K_P=10 and K_I=2500. Because the comparison of the grid- and reference currents as well as the grid voltage and -frequency look identical to the ones shown in Figures 4.1 and 4.2, they will now be included in this thesis.

Even though the voltage-, current-, and frequency measurements look identical, there is a noticeable difference in the THD for the different scenarios, wherefore they are compared in Table 4.1. The comparison table also includes the THD results for additional harmonic compensation, where the 11th and 13th harmonics are compensated.

		THD			
PI Control	Phase	Standard HC		Additional HC	
$K_P = 10$, $K_I = 2500$	a	0.53 %		0.54 %	
	b	0.51 %	≈ 0.53 %	0.51 %	≈ 0.53 %
	c	0.54 %		0.53 %	
$K_P = 15$, $K_I = 2000$	a	0.56 %		0.62 %	
	b	0.59 %	≈ 0.58 %	0.59 %	≈ 0.59 %
	c	0.60 %		0.57 %	
$K_P = 20$, $K_I = 1500$	a	0.61 %		0.59 %	
	b	0.62 %	≈ 0.62 %	0.62 %	≈ 0.60 %
	c	0.62 %		0.59 %	

Table 4.1: Comparison of the THD three different PI current control schemes. Standard harmonics are 5th and 7th, whereas additional harmonics include 11th and 13th.

It might seem odd that the additional harmonic compensation has not improved the THD. It is important to remember that these are ideal simulations without external disturbances. As shown in Chapter 5, this additional harmonic compensation will greatly improve the performance of the control system in practice, which is why it is considered in the simulations as well. What also comes as a surprise is that the THD increases with K_P. From the simulation results, the first scenario yields the best performance. In practice however, the last scenario has the best performance. It is important to take these values with some scepticism and draw a final conclusion once more data has been gathered.

4.2 PR Control

As mentioned back in Section 3.6, proportional resonant controllers have gained notoriety in grid-connected inverter control. With the removal of the voltage feed forwards and the coupling terms, the complexity of the control system has lowered. By simulating this control scheme, it can be compared to the performance of the conventional PI control scheme, potentially increasing the performance of the system.

Because of the restrictions on the experimental setup, two variations of the PR control scheme will be simulated. The first one is without voltage feed forwards and coupling terms, whereas the second is with voltage feed forwards. The experimental setup cannot run if the voltage feed forwards are removed, as the inverter instantly trips out. For this reason, the actual PR control scheme used and implemented will have voltage feed forwards implemented. However, in order to compare the performance with- and without voltage feed forwards added, both variations will be simulated in this section.

The Current Control block in the simulation for the PR control scheme can be seen in Appendix A.9. Since the control scheme is using stationary reference frame, the current control is performed separately for each frame; α- and β-frame. The content of these two blocks can be found in Figures A.39 and A.40, also in Appendix A.9. In the experimental setup, a *Task Overrun* error occurs when additional harmonic compensation is added.

This is caused by the restrictiveness of the setup and is the result of a lack in memory. For this very reason, the additional harmonic compensation will not be performed on the PR control scheme.

The simulation is once again run for the same three scenarios as for the PI control scheme. Figure 4.3 shows the grid voltage-, grid currents-, and grid frequency measurements for the scenario with K_P=20 and K_I=1500 without the feed forward and coupling terms.

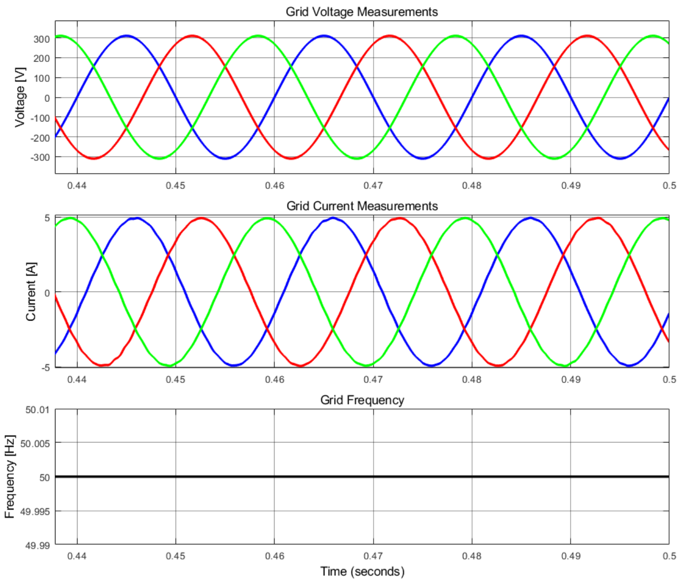

Figure 4.3: Grid voltage, -current and -frequency measurements for PR control scheme simulation with $K_P = 20$ and $K_I = 1500$.

The figure shows that the grid voltages, -currents and -frequency are still stable. The reference- and grid currents are compared in Figure 4.4.

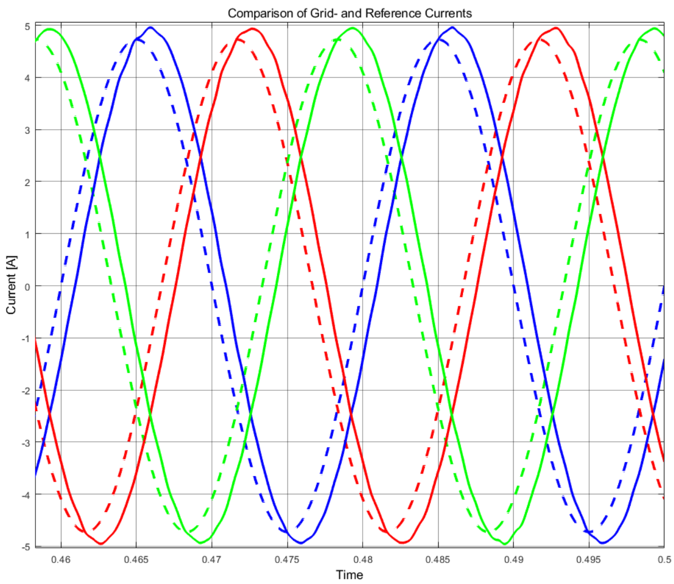

Figure 4.4: Comparison of the grid- and reference currents for PR control scheme simulation with $K_P = 20$ and $K_I = 1500$.

There is still a phase lag between the two currents, which again could potentially be eliminated with a lead controller. The grid voltage-, grid current- and frequency measurements for the PR control scheme with voltage feed forward and coupling terms incorporated are not included in this paper, since they too look identical to the already shown graphs. Running both PR control schemes with all three scenarios each, the THD results are compared in Table 4.2.

		THD			
PR Control	Phase	Standard PR		w/ Voltage Feed Forward	
$K_P = 10$, $K_I = 2500$	a	0.44 %		0.44 %	
	b	0.41 %	≈ 0.43 %	0.37 %	≈ 0.42 %
	c	0.45 %		0.44 %	
$K_P = 15$, $K_I = 2000$	a	0.49 %		0.48 %	
	b	0.47 %	≈ 0.48 %	0.44 %	≈ 0.46 %
	c	0.49 %		0.47 %	
$K_P = 20$, $K_I = 1500$	a	0.51 %		0.53 %	
	b	0.48 %	≈ 0.50 %	0.55 %	≈ 0.53 %
	c	0.50 %		0.52 %	

Table 4.2: Comparison of the THD three different PR current control schemes with- and without voltage feed forwards and coupling terms.

Overall, the PR control scheme reduces the amount of THD compared to the conventional PI control scheme, according to these simulations. Using voltage feed forwards in the PR scheme will increase the THD for some and decrease it for other scenarios. The experimental results in Chapter 5 will verify whether this holds true in practice.

4.3 Fuzzy Logic PI Control

The PI control simulation from Section 4.1 is further expanded upon by integrating a fuzzy logic controller to control the proportional- and integral gains. As mentioned in Section 3.7, the fuzzy logic Sugeno will be used, since the Mamdani cannot be implemented into the experimental setup. The issue lies with the Fuzzy Logic Toolbox in Simulink, which is too computational intensive to run in real time with this experimental setup. The fuzzy logic Sugeno controller will therefore be build from the ground up and compared to the simulations with the Fuzzy Logic Sugeno Toolbox controller to compare its performance.

The Current Control block utilising fuzzy logic for controlling the PI controllers can be found in Appendix A.10, Figure A.41. The only difference between this and that of the conventional PI control scheme is that the proportional- and integral gains are no longer determined as constants and fed into the current control for each frame, as shown in Figure A.42 and A.43 in Appendix A.10. The gains of the PI controllers are now controlled by a fuzzy logic Sugeno controller. In the two figures, the fuzzy logic controller build from scratch is shown. To use the Fuzzy Logic Toolbox instead, this block should be replaced with that. Three scenarios will again be simulated for; $K_P = 10 \pm 1$, $K_P = 15 \pm 1$ and $K_P = 20 \pm 1$. When testing for e.g. $K_P = 20 \pm 1$, the medium output value of the Sugeno fuzzy logic controller will be 20, the large output will be 21, and the small output will be 19. The reason why ± 1 is chosen is from evaluating the performance of the experimental setup. ± 1 resulted in the least amount of THD, compared to $\pm 2, \pm 3, \pm 4$. The output for the integral gains will be consistent throughout all simulations, $K_I = 2000 \pm 500$.

The grid voltage-, grid current-, and grid frequency measurements are shown in Figure 4.5 for $K_P = 20 \pm 1$, using the Fuzzy Logic Toolbox controller. The grid voltage is still stable and the frequency is 50 Hz.

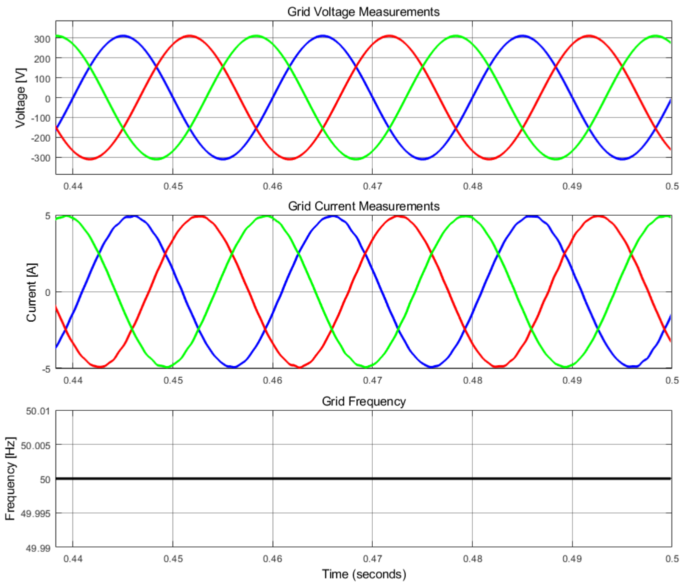

Figure 4.5: Grid voltage, -current and -frequency measurements for fuzzy logic PI control scheme simulation with $K_P = 20 \pm 1$.

Comparing the reference- and measured currents in Figure 4.6 shows no real difference to the conventional PI control scheme.

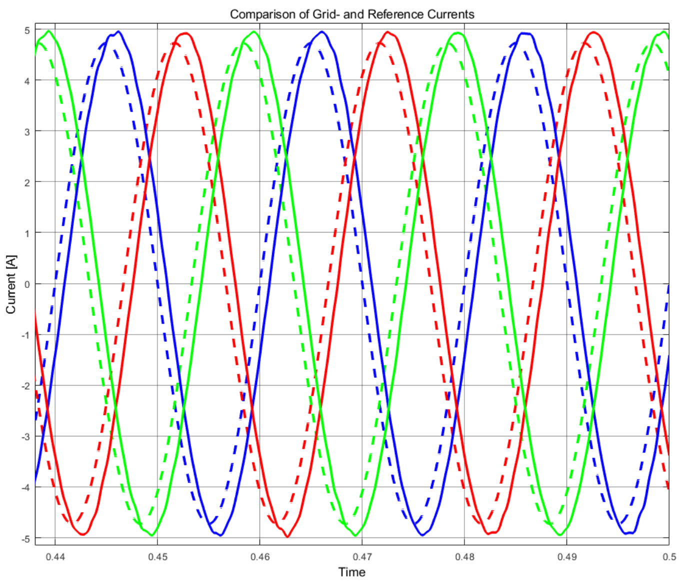

Figure 4.6: Comparison of the grid- and reference currents for fuzzy logic PI control scheme simulation with $K_P = 20 \pm 1$.

As far as the other simulations, where $K_P = 15 \pm 1$ and $K_P = 10 \pm 1$, the current comparisons cannot be distinguished from Figure 4.6, wherefore they are not included in this paper.

The fuzzy logic controller build from scratch consists of the same elements as the Fuzzy Logic Toolbox controller; membership functions for the error and change in error, ruleset and defuzzification. The overall Simulink model of the fuzzy logic scratch block can be seen in Figure A.44. The membership functions and evaluation is constructed using many logical operators in order to categorise the inputs, as illustrated in Figures A.45 and A.46. After the inputs have been categorised, the ruleset, see Figure A.47, determines the appropriate outputs for the fuzzy logic controller. The ruleset is constructed using even more logical operators than for in membership functions evaluation. All figures mentioned can be found in Appendix A.10.

The membership functions are tuned differently in the simulations than in the experimental setup. They are tuned from the error and change in error between the reference- and measured currents in the simulation control loops, see Figure A.48. The error and change in error between the d- and q-frames are very similar, wherefore they will be tuned from the d-frame measurements and used in both frames. Since these two parameters are different in the simulations compared to the experimental setup, the membership functions must the tuned with respect to the appropriate application. The membership functions used in both the d- and q-frame for both inputs are shown in Figure 4.7.

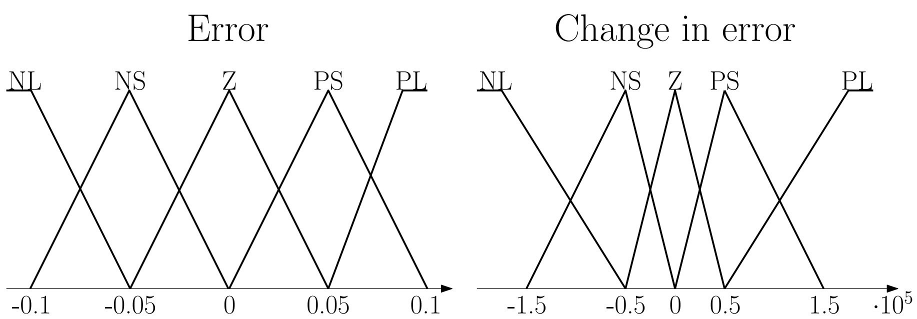

Figure 4.7: Membership functions used for fuzzy logic controllers in fuzzy logic PI control scheme.

The fuzzy logic scratch controller is also tested using additional harmonic compensation. As with the conventional PI control scheme, this entails compensating the 11$^{\text{th}}$ and 13$^{\text{th}}$ harmonics in addition to the 5$^{\text{th}}$ and 7$^{\text{th}}$ harmonics. Given that the performance cannot be compared by evaluating the voltage-, current-, and frequency measurements, the THDs are compared in Table 4.3 to give a better indication of the performances.

		THD					
Fuzzy Logic PI Control	Phase	Toolbox		Scratch		Scratch Additional HC	
	a	0.55 %		0.5 %		0.57 %	
$K_P = 10 \pm 1$	b	0.55 %	≈ 0.56 %	0.53 %	≈ 0.52 %	0.54 %	≈ 0.55 %
	c	0.57 %		0.52 %		0.53 %	
	a	0.61 %		0.59 %		0.61 %	
$K_P = 15 \pm 1$	b	0.57 %	≈ 0.58 %	0.61 %	≈ 0.61 %	0.63 %	≈ 0.63 %
	c	0.56 %		0.62 %		0.64 %	
	a	0.57 %		0.59 %		0.64 %	
$K_P = 20 \pm 1$	b	0.60 %	≈ 0.60 %	0.61 %	≈ 0.60 %	0.62 %	≈ 0.64 %
	c	0.64 %		0.59 %		0.65 %	

Table 4.3: Comparison of the THDs for three different fuzzy logic PI control scenarios. Fuzzy Logic Toolbox is the build-in Simulink block, whereas Fuzzy Logic Scratch is build from the ground up. Both are Sugeno fuzzy logic controllers.

The table shows that the fuzzy logic scratch controller performs just as well as the Fuzzy

Logic Toolbox controller. From these simulations, it cannot be determined definitively whether the performance is better or worse, since the performance looks very much the same. However, if simulation time is used in the evaluation as well, the performance of the fuzzy logic controller build from scratch is much better, since it is less computationally intensive and the simulation runs much, much faster. This is also what makes it possible to use the fuzzy logic controller in real time, since the Fuzzy Logic Toolbox controller is too taxing on the experimental setup used in this thesis. As for the additional harmonic compensation, the conclusion from these simulations must be that they do not improve the performance of the control schemes. This is most likely due to the few harmonics actually present in this ideal system. Compensating for additional harmonics will only introduce more harmonic distortion. This will not be the case in the experimental results though, since there are naturally much more external disturbances in the system. Go to Chapter 5 to see the experimental results for this control schemes.

4.4 Fuzzy Logic PR Control

As mentioned back in Section 4.2, the PR control scheme cannot be implemented in the experimental setup without using voltage feed forwards. The comparison between the PR control scheme with and without voltage feed forwards indicated that the performance was very much the same between the two. Whether this is the case in practice cannot be tested, but, in this section, only the control scheme with voltage feed forwards will be tested with fuzzy logic implementation.

As was the case with the fuzzy logic PI control in the previous section, the fuzzy logic controller is used to regulate the proportional- and integral gains of, in this section, the PR controller. The Fuzzy Logic Toolbox controller will be compared to the performance of the fuzzy logic controller build from scratch, both being Sugeno types.

The Current Control block of the fuzzy logic controlled PR scheme simulation can be found in Appendix A.11, Figure A.49. Figure A.50 and A.51 show how the fuzzy logic controller is used to control and vary the proportional- and integral gains within the α- and β-frames, respectively. The fuzzy logic controllers showed in the figures are the ones build from scratch, which should be replaced by the Fuzzy Logic Toolbox controller if required.

The construction of the fuzzy logic controller from scratch was explained back in Section 4.3. The membership functions of the fuzzy logic controller are again tuned from the error and change in error in the conventional PR control scheme simulation. However, since they look very similar to those of the errors and change in errors in the PI control scheme, the same membership functions will be used as was used in Section 4.3. The same three scenarios will be tested; $\mathrm{K_P} = 10 \pm 1$, $\mathrm{K_P} = 15 \pm 1$ and $\mathrm{K_P} = 20 \pm 1$.

The grid voltage-, grid current-, and frequency measurements are shown in Figure 4.8 below, using the fuzzy logic controller build from scratch.

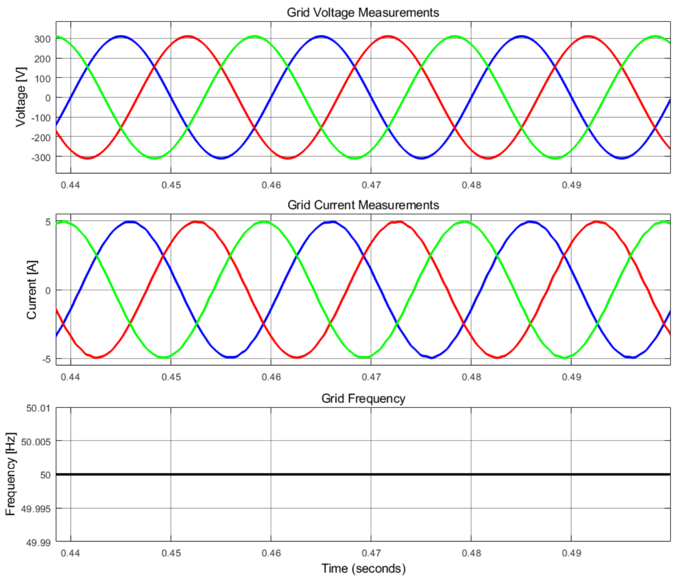

Figure 4.8: Grid voltage, -current and -frequency measurements for fuzzy logic PR control scheme simulation with $K_P = 20 \pm 1$.

The grid voltage is stable, the current injected into the grid satisfies the active power requirement, and the frequency is stable around 50 Hz. Figure 4.6 plots the reference- and grid currents together for comparison.

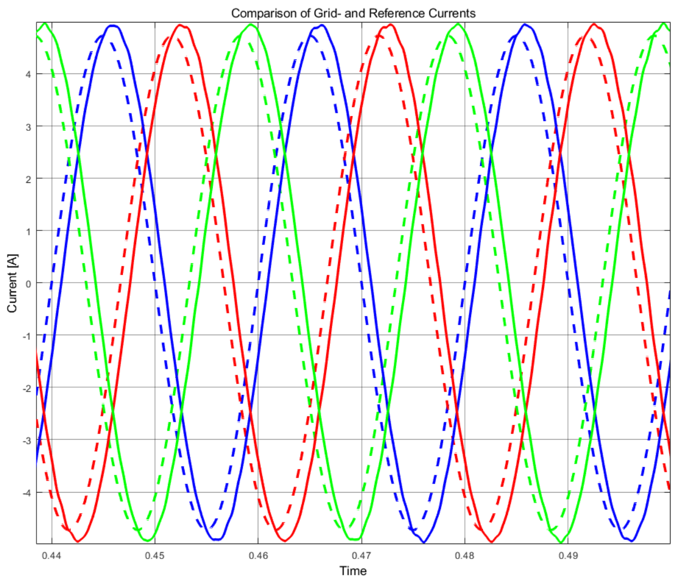

Figure 4.9: Comparison of the grid- and reference currents for fuzzy logic PR control scheme simulation with $K_P = 20 \pm 1$.

By now it is clear that the comparison between the reference- and grid current plots all look identical for almost all control schemes. They contain a small phase lag, which could be eliminated by using a lead controller. Again, this will not be examined in this thesis. The performance of the simulations is still best compared by evaluating the THD, wherefore an overview can be seen in Table 4.4 below.

		THD			
Fuzzy Logic PR Control	Phase	Toolbox		Scratch	
	a	0.47 %		0.41 %	
$K_P = 10 \pm 1$	b	0.48 %	≈ 0.47 %	0.39 %	≈ 0.41 %
	c	0.45 %		0.42 %	
	a	0.45 %		0.46 %	
$K_P = 15 \pm 1$	b	0.43 %	≈ 0.44 %	0.47 %	≈ 0.47 %
	c	0.45 %		0.48 %	
	a	0.50 %		0.50 %	
$K_P = 20 \pm 1$	b	0.51 %	≈ 0.50 %	0.47 %	≈ 0.51 %
	c	0.49 %		0.57 %	

Table 4.4: Comparison of the THDs for three different fuzzy logic PR control scenarios. Fuzzy Logic Toolbox is the build-in Simulink block, whereas Fuzzy Logic Scratch is build from the ground up. Both are Sugeno fuzzy logic controllers.

The same applies here as it did for the fuzzy logic PI control in Section 4.3; no definite conclusion can be made on the performance of the fuzzy logic scratch controller compared to the Fuzzy Logic Toolbox controller. The THDs are better for some gains and worse for others. However, the simulation time is still much, much quicker than the toolbox controller, allowing the fuzzy logic scratch controller to be implemented in the real-time experimental setup.

4.5 Discussion of Simulation Results

It can be quite tedious to compare the different control schemes without a proper overview of all the simulation results. This is the purpose of this section. Table A.1 below has been made to give an overview of the different simulations.

	THD		
Current Control Schemes	K_P=10	K_P=15	K_P=20
PI Control	0.53 %	0.58 %	0.62 %
PI Control Additional HC	0.53 %	0.59 %	0.60 %
PR Control	0.42 %	0.46 %	0.53 %
Fuzzy Logic PI Control	0.52 %	0.61 %	0.60 %
Fuzzy Logic PI Control Additional HC	0.55 %	0.63 %	0.64 %
Fuzzy Logic PR Control	0.41 %	0.47 %	0.51 %

Table 4.5: Overview and comparison of the THD results for all simulations of the different current control schemes. Additional harmonic compensation includes the 11^{th} and 13^{th} harmonics as opposed to only the 5^{th} and 7^{th} harmonics.

It is important to keep in mind that these results reflect an ideal situation, where some disturbances are unaccounted for and not present in the simulations. Therefore, these results should be taken with a degree of uncertainty.

The PI control scheme represents the baseline given in the experimental setup. The control loop is not identical to that of the experimental setup, more on this in Chapter 5, but the results of the PI control simulations can be interpreted as the baseline results. These are the results that are desired to improve for achieving better performance for the current control of the system.

According to the simulation results, adding extra harmonic compensation will not improve the performance of the control system. In fact, it will worsen the performance. It will be exiting to test this out in the experimental setup, to see if that is really the case in practice as well. But so far, the simulation results show it will not improve the performance of the baseline.

On the other hand, using a PR controller instead of a PI controller will greatly increase the performance of the system. This is most likely due to the extra harmonic compensation for the 5^{th} and 7^{th} harmonics, compensating after the controllers as well as inside the controllers. However, it will require some experimental testing to draw any final conclusions.

As for the fuzzy logic controller implementation, the results are inconsistent across the board. From the simulations, there is no indication that using fuzzy logic to control the gains of the PI- and PR controllers will increase the performance of the control system. This must also be taken to the experimental setup in order to draw any final conclusions on the implementation of fuzzy logic controllers.

Section 5

Experimental Results

The purpose of this chapter is to test the control schemes in a laboratory experimental setup. A baseline experimental model has been provided and the goal of this thesis is to improve the performance of the experimental setup. In order to do this, the baseline and experimental setup must be explained.

Throughout the previous chapters, it has been hinted that the experimental setup is very restricted and there are certain limitations that prohibits some changes to be implemented. Pictures of the laboratory setup can be seen in Appendix A.12, Figures A.53 and A.54. The latter picture has numbers written, which will be referred to when discussing where measurements are taken from within the system.

The laboratory setup consists of an inverter (point 1), inverter side inductors (point 2), voltage- and current measurements (point 3), filter capacitor in parallel (point 4), ideal transformer used as the grid side inductor (point 5), and then connection to the grid afterwards. Voltage measurements can only be taken from point 3, meaning it is the capacitor voltage. Current measurements can be taken both from point 3 and 5. In the baseline, the current measurements are taken from point 5, from the ideal transformer. This essentially means that the current measurements used in the control loop are the grid currents, whereas the voltage measurements used are the capacitor voltages. The current measurements can be changed to point 3, which is basically the inverter current.

It is most likely apparent by now that the control schemes used in the simulations are different from the experimental setup. There are several reasons for that. Most importantly, the simulations were not possible when changing the control loop to use the grid current measurements, instead of the inverter currents. The system became very unstable. The only way to prevent the system from being unstable was to lower the gains to such a degree that there was almost no actuation from the controllers. By using the inverter currents, the gains in the simulations can be increased as high as they can in the experimental setup.

The question then might be; what happens when the currents used in the control loop of the experimental setup are changed to the inverter currents (point 3)? Figure 5.1 shows the grid currents alongside the reference currents for the laboratory PI control scheme using the inverter currents in the control loop. The THD is around 36 %, concluding that this cannot be implemented.

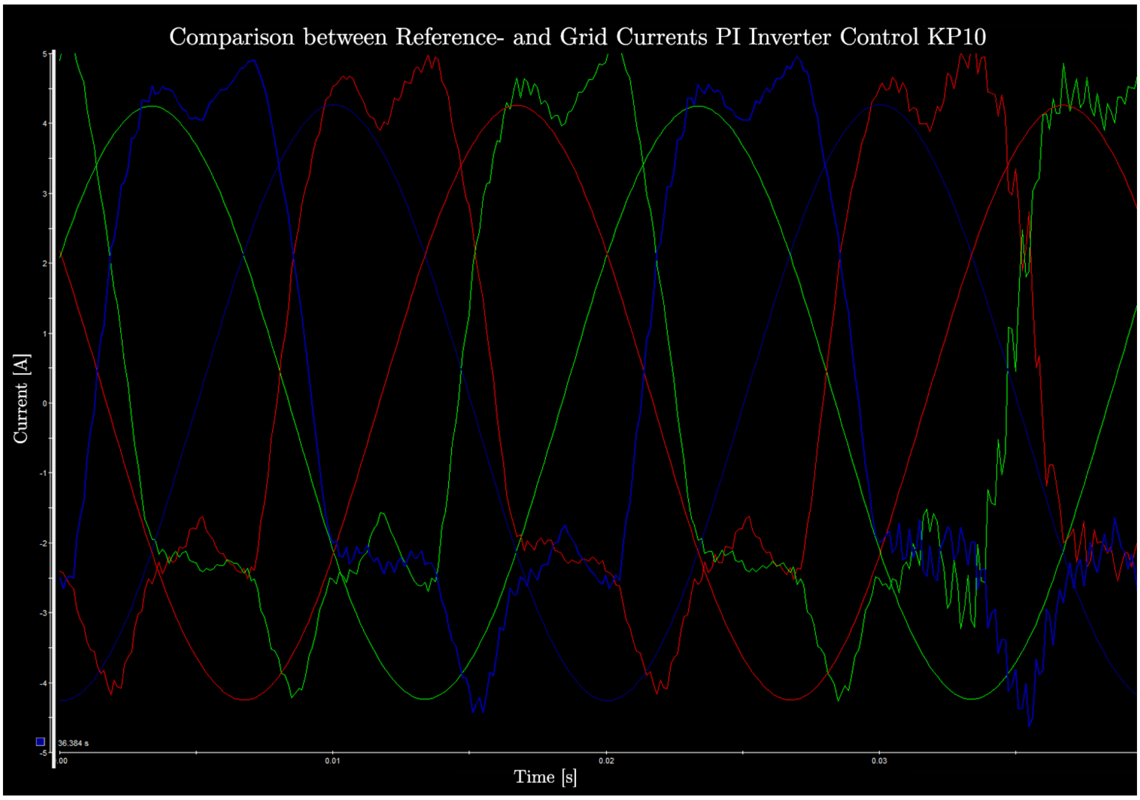

Figure 5.1: Grid current measurements compared the reference currents for the laboratory PI control scheme using inverter current measurements in the control loop for K_P=10.

Figure A.55 and A.56 in Appendix A.12 shows the corresponding graphs for the scenarios K_P=15 and K_P=20, displaying high instability with the THD reaching up towards 98 %. A potential cause for this could be the sampling time chosen. In the experimental setup, the sampling time is $1.25{\cdot}10^{-4}$, whereas it is $1.25 \cdot 10^{-6}$ in the simulations. Setting it to $1.2510{\cdot}^{-4}$ in the simulations will make the simulations unstable. This essentially means that the simulations are also unstable when using the same sampling time, as is used in the experimental setup. Due to the restrictiveness of the experimental setup, the sampling time cannot be increased to $1.25{\cdot}10^{-6}$. If the sampling time could be increased, the instability of the experimental setup when using the inverter currents in the control loop could potentially be resolved.

As for the voltage measurements used in the experimental setup, it seems odd that the capacitor voltage is used. In grid-connected inverter control systems, the grid voltage is always used to synchronise the currents to the grid voltages. By using the capacitor voltage, the control system cannot function optimally since the voltage has yet to be filtered fully and will contain some sort of distortion. This might have a very small effect on the system operation or it might have a great impact. A way to illustrate that this might be an issue is to take a look at Figure 5.2.

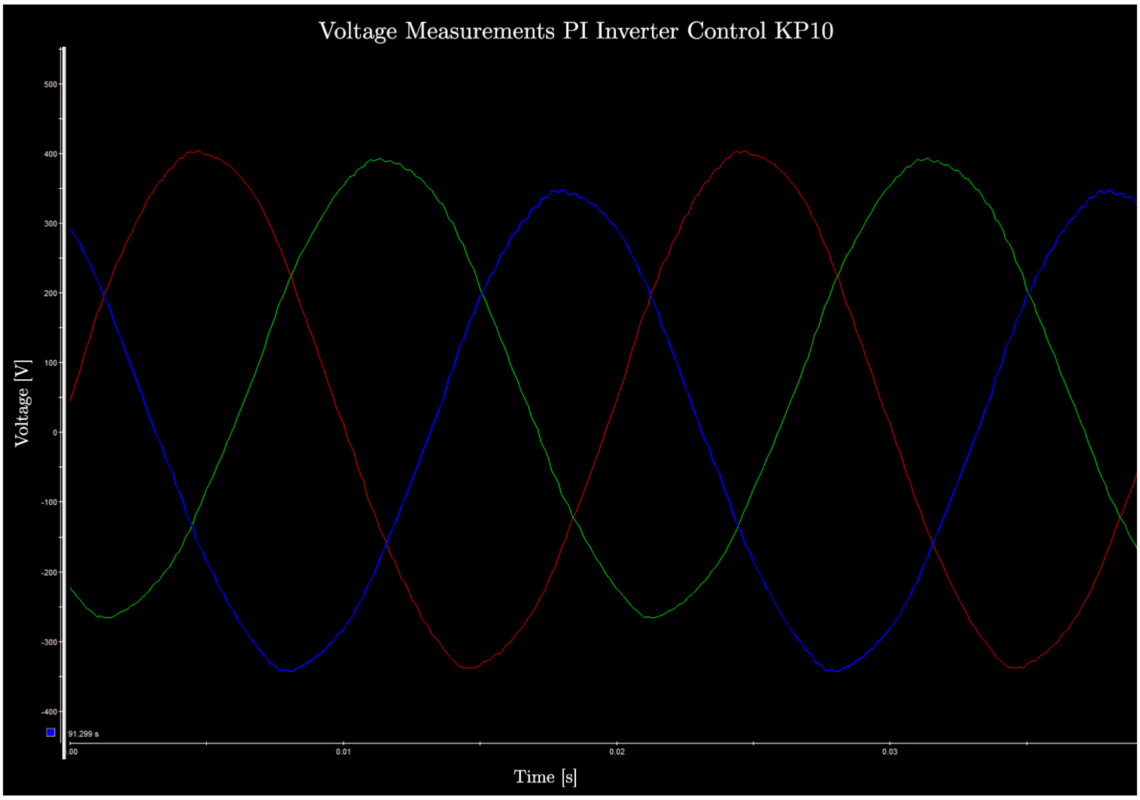

Figure 5.2: Voltage measurements for the laboratory PI control scheme using inverter current measurements in the control loop for K_P=10.

This is the voltage measurements that are used in the phase-locked loop to synchronise the currents and used as voltage feed forwards. The currents used in the control loop are still the inverter currents, where it was shown that the performance was unsatisfactory. Taking a closer look at the figure above, it can easily be seen that the signals are distorted and does not have the same amplitudes. No matter if the system is stable or not, the voltage measurements used in the control system should remain unaffected. That is the reason why the grid voltage is used, since that is generally without any distortion. If the proportional gain is increased from 10 to 20, the voltage signals get heavily distorted, see Figure 5.3.

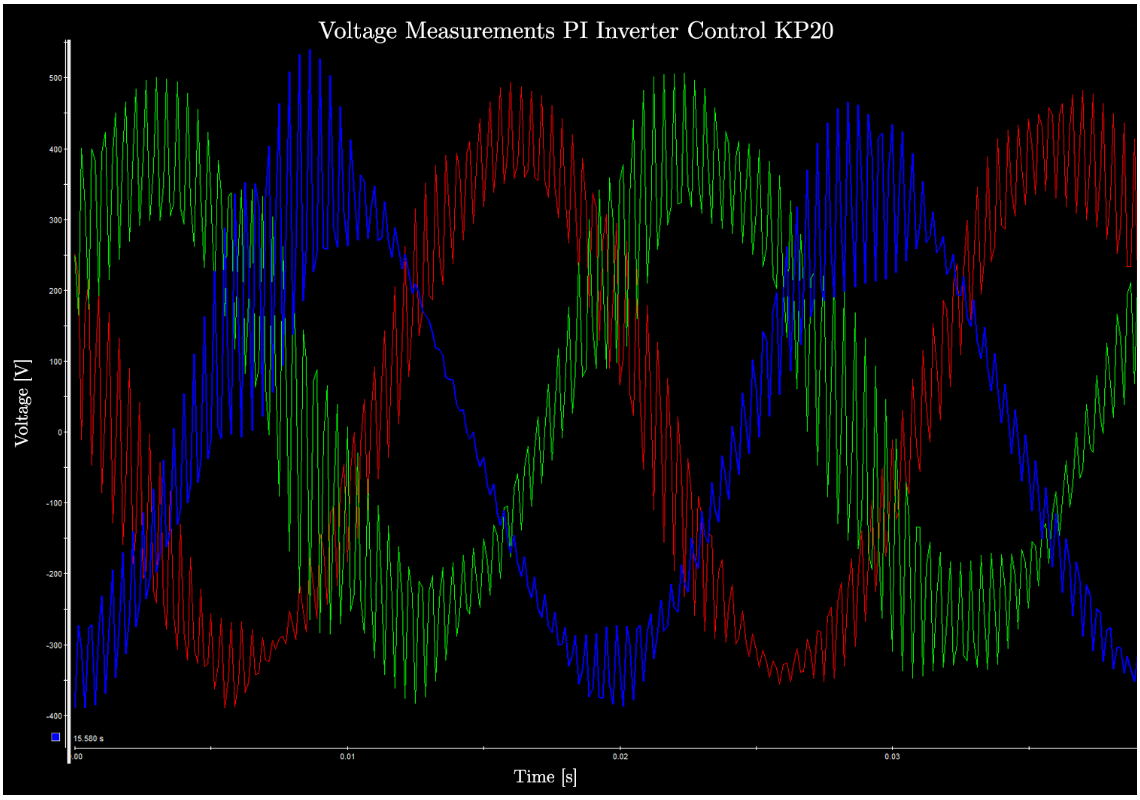

Figure 5.3: Voltage measurements for the laboratory PI control scheme using inverter current measurements in the control loop for K_P=20.

The distortions are so severe that it will have a large impact on the system performance. Keep in mind, these voltage signals should be unaffected. This can have severe implications to the system and is most likely one of the reasons behind the restrictiveness of the experimental setup.

The frequency for the control scheme using the inverter current can be found in Appendix A.12, Figure A.57. It is only shown for K_P=10, since K_P=15 and K_P=20 look very similar and remains around 50 Hz.

The following section will elaborate on more issues with the baseline model provided. It is important to note that the scope of this thesis is to improve the experimental control system and not improve the overall system performance. This is a very important distinction, since it allows to solely focus on the current control system. What this essentially means is that even though the system performance might not be optimal and has some restrictions, the purpose is to replace the PI control scheme, used in the baseline model, with other types of control schemes. By comparing the performance of the baseline model to the performances of the other control schemes, the performance can be determined by the reduction made in the THD of the baseline model.

5.1 PI Control

This section will evaluate the baseline model, which is basically a PI control scheme. The same configuration and parameters are chosen as in the simulations, see Appendix A.1. First and foremost, the grid voltage and frequency will be evaluated. Remember that the grid voltage is actually the capacitor voltage in this setup, which is not ideal. The easiest way to compare the performances is by comparing the THDs of the control schemes. Like in the simulations, additional harmonic compensation will be tested. The baseline includes harmonic compensation for the 5th and 7th harmonics, whereas the additional harmonic compensation will include the 11th and 13th harmonics. A comparison of the THDs for the different scenarios can be seen in Table 5.1.

	THD	
PI Control	Baseline	Additional HC
$K_P = 10$, $K_I = 2500$	3.43 %	2.09 %
$K_P = 15$, $K_I = 2000$	2.94 %	1.99 %
$K_P = 20$, $K_I = 1500$	2.71 %	1.94 %

Table 5.1: Comparison of the THDs in the experimental setup for the PI control scheme. Standard harmonics are 5th and 7th (baseline model), whereas additional harmonics include 11th and 13th.

The performances of both the baseline and the baseline with additional harmonic compensation look very good. Both can achieve THDs below 3 %, even at medium gains. It is clear that the performance is increased heavily by compensating for the additional harmonics. Even for the lowest proportional gain, the performance is better than for the baseline with the highest proportional gain. If a system is close to instability, compensating for the additional harmonics can lead to larger stability margins, since the gains can be lowered substantially. This is not an issue in this experimental setup though.

The voltage- and frequency measurements are also stable, as shown in Figure A.58 and A.59, Appendix A.13.

From inspecting Table 5.1 and evaluating the voltages and frequency, the performances of the control schemes look very good at first glance. However when inspecting the grid current measurements, something is not right. Figure 5.4 compares the reference currents to the grid currents for $K_P = 20$.

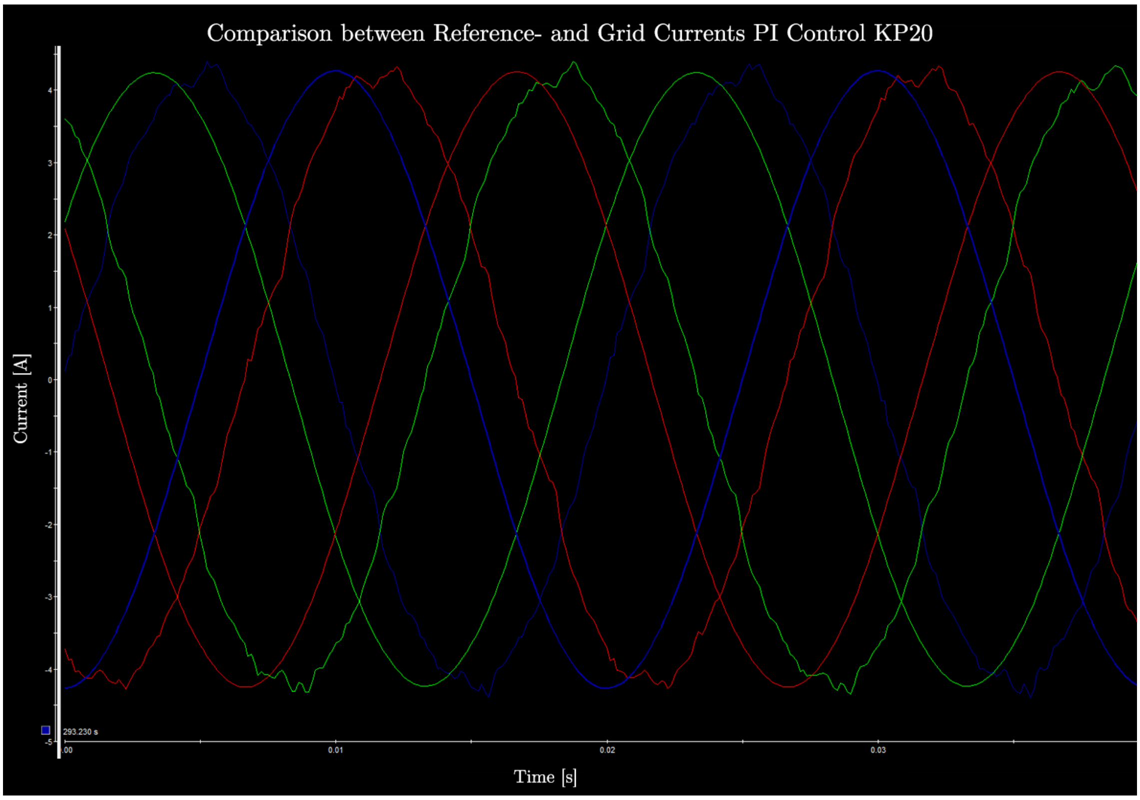

Figure 5.4: Comparison of the grid- and reference currents for PI control scheme in experimental setup with $K_P = 20$.

The figure shows that there is a significant phase lag between the grid currents and the reference currents. The amplitudes are equal, but they are not synchronised. This is a problem, since it will create disturbances on the grid. The reason behind the large phase lag is unclear. The same issue arises for $K_P = 15$ and $_P = 10$, shown in Figure A.60 and A.61. The fact, that they are not synchronised, further confirms that the baseline does not function properly.

The problem persists for all proportional gains tested. The voltage measurements for the other proportional gains will not be included in this thesis, since they are identical to the ones found in Figure A.58. The frequency measurements and current comparisons can be found in Appendix A.13.

As for the experimental results for the additional harmonic compensation, this same issue arises. The current comparisons for these are located in Appendix A.13.

5.2 PR Control

It is now time to test the PR control scheme in the experimental setup. As mentioned back in Section 4.2, the voltage feed forwards cannot be removed from the experimental setup. Furthermore, the experimental testing cannot be done for additional harmonic compensation, meaning only the 5^{th} and 7^{th} harmonics are compensated for.

As with the PI control scheme, the THDs of the different scenarios are noted and can be seen in Table 5.2 below.

PR Control	THD
$K_P = 10$ $K_I = 2500$	4.08 %
$K_P = 15$ $K_I = 2000$	3.62 %
$K_P = 20$ $K_I = 1500$	3.66 %

Table 5.2: Comparison of the THDs in the experimental setup for the PR control scheme.

The table indicates that the performance of the PR control scheme is worse than the PI control scheme, contrary to the conclusion from the simulations in Section 4.5. In order to determine the difference in results between the two, a closer look will be taken at the voltage-, current-, and frequency measurements. As for the voltage- and frequency measurements, please refer to Figure A.66 and A.67, respectively. These remain more or less similar to those for the PI control scheme. Taking at closer look at the grid currents for $K_P = 20$ in Figure 5.5, a noticeable difference can be noticed.

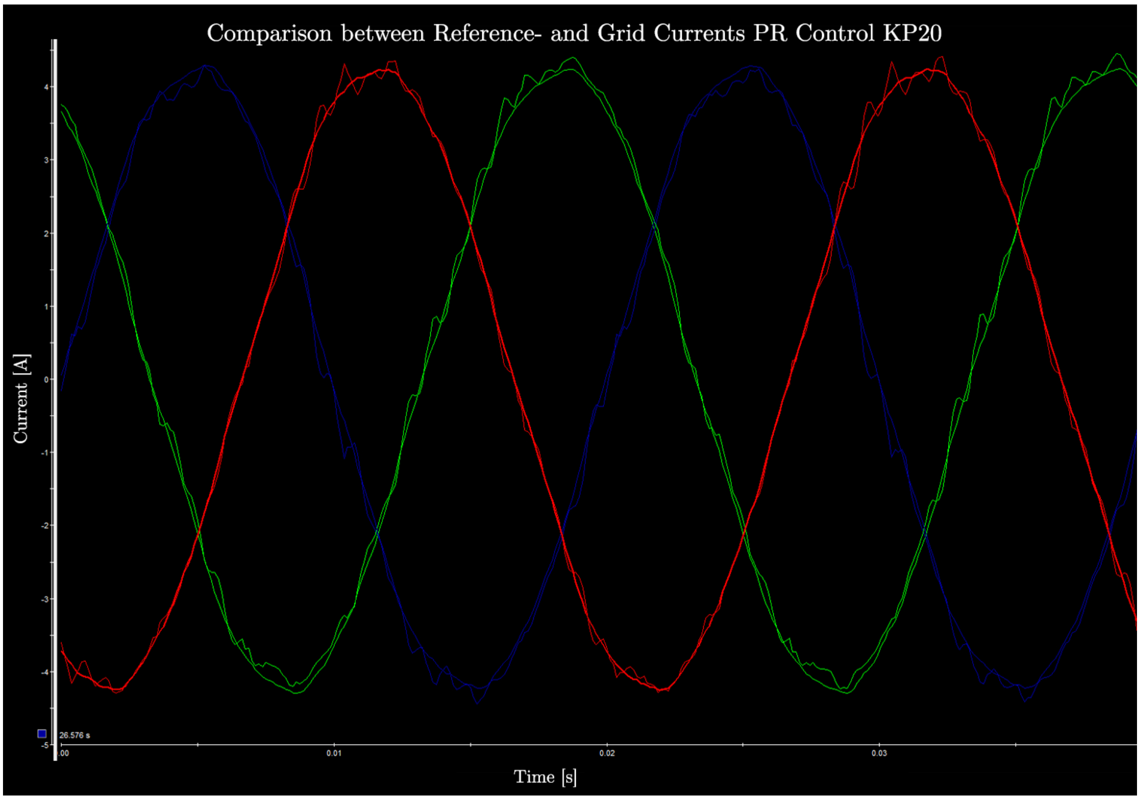

Figure 5.5: Comparison of the grid- and reference currents for PR control scheme in experimental setup with $K_P = 20$.

The phase lag has been eliminated and the grid currents follow the reference currents nicely. However, there is significantly more distortion on the signal. The fact that there is such a drastic difference between the two control schemes is very peculiar and the reason behind it is unclear. One might think that it is due to the removal of the coupling terms in the PR control scheme, but that has been tested and was not the cause. The biggest difference between the two control schemes is the reference frame used. The PR control scheme uses stationary reference frame and does not require θ to be transformed, whereas the PI control scheme operates in synchronous reference frame and does require θ to be transformed. However, this does not explain why there is a heavy phase lag for the PI control scheme and none for the PR control scheme. The phase-locked loop functions correctly and the angle θ has been used consistently and correctly throughout all transformations in the PI control scheme.

The comparisons between the grid- and reference currents for $K_P = 15$ and $K_P = 10$ are located in Appendix A.14. The same interpretations are applicable for these.

The question is now which control scheme is determined to have the best performance.

Looking solely at the THDs, the PI control scheme wins. However, the current injected into the grid for the PI control scheme is out of sync and this will result in more issues than the higher THD from the PR control scheme. Both control schemes will be improved in the coming sections by implementing fuzzy logic controllers, but the distinction between the results is very important to keep in mind.

5.3 Fuzzy Logic PI Control

As was done in Section 4.3, the PI control scheme is expanded by implementing fuzzy logic controllers to regulate the proportional- and integral gains of the PI controllers. The fundamental principles and tuning was explained back in Section 3.7 and 4.3, where the former included the tuning for the experimental setup. As was mentioned earlier, the Fuzzy Logic Toolbox controller in Simulink is too computationally expensive to implement in the experimental setup. For this reason, a fuzzy logic controller was build from scratch which fortunately can run in real-time and can be implemented into the experimental models.

The voltage- and frequency measurements will not be included in this thesis, since they are identical to those for the conventional PI control scheme. The current comparisons between the reference- and grid currents, on the other hand, can be found in Appendix A.15 for all scenarios, including the different gain scenarios as well as the additional harmonic compensation. They are all moved to the appendix, since they look similar to each other and to those from the conventional PI control scheme and does not give any new information. Table 5.3 shows the THDs for each of the different scenarios.

	THD	
Fuzzy Logic PI Control	Standard HC	Additional HC
$K_P = 10 \pm 1$	2.91 %	1.87 %
$K_P = 15 \pm 1$	2.58 %	1.81 %
$K_P = 20 \pm 1$	2.41 %	1.88 %

Table 5.3: Comparison of the THDs in the experimental setup for the fuzzy logic controlled PI control scheme. Standard harmonics are 5^{th} and 7^{th} (baseline model), whereas additional harmonics include 11^{th} and 13^{th}.

The purpose of adding fuzzy logic into the control scheme was to improve the performance of the PI control scheme. By evaluating the THDs, this is successfully accomplished. A deeper comparison will be performed in Section 5.5, where all the control schemes are compared to each other. As for now, it is safe to conclude that the fuzzy logic PI control scheme performs better than the conventional PI control scheme, both with and without the additional harmonic compensation.

5.4 Fuzzy Logic PR Control

The PR control scheme is also expanded upon by using fuzzy logic to regulate the proportional- and integral gains of the PR controllers. The tuning of the fuzzy logic controllers for the PR control scheme in the experimental setup was performed back in Section 3.7.1.

The voltage- and frequency measurements are not included once again, since they are non-distinguishable from those for the conventional PR control scheme. The comparisons between the reference- and grid currents are located in Appendix A.16. Table 5.4 shows the THDs for the different gain scenarios tested.

Fuzzy Logic PR Control	THD
$K_P = 10 \pm 1$	3.87 %
$K_P = 15 \pm 1$	3.53 %
$K_P = 20 \pm 1$	3.60 %

Table 5.4: Comparison of the THDs in the experimental setup for the fuzzy logic controlled PR control scheme.

Implementing the fuzzy logic controllers into the PR control scheme has improved the performance, but the THD still does not reach below the distortion of the baseline. However, the same interpretation applies, where the grid currents tracks the reference currents nicely without any phase delay. Why this is the case is still unclear.

5.5 Discussion of Experimental Results

The PI control scheme was the baseline model provided that was desired to be optimised. It can be difficult to determine when exactly the performance of the control system has been improved, since there are many factors in play. The grid currents are severely out of phase with the reference currents in the baseline model, which will cause disturbances to the grid when the currents are injected into it. Therefore, the baseline model can be improved both by reducing the phase lag and by reducing the total harmonic distortion of the current.

Table 5.5 shows all THD values for all control schemes tested in the experimental setup. The table includes the THD values for the corresponding simulations. It is important to keep in mind that the simulations use the inverter current measurements in the current control loop, whereas the experimental setup uses the grid current measurements. This will obviously affect the THD values.

	THD					
	Simulations			Laboratory		
Current Control Schemes	K_P=10	K_P=15	K_P=20	K_P=10	K_P=15	K_P=20
PI Control	0.53 %	0.58 %	0.62 %	3.43 %	2.94 %	2.71 %
PI Control Additional HC	0.53 %	0.59 %	0.60 %	2.09 %	1.99 %	1.94 %
PR Control	0.42 %	0.46 %	0.53 %	4.08 %	3.62 %	3.66 %
Fuzzy Logic PI Control	0.52 %	0.61 %	0.60 %	2.91 %	2.58 %	2.41 %
Fuzzy Logic PI Control Additional HC	0.55 %	0.63 %	0.64 %	1.87 %	1.81 %	1.88 %
Fuzzy Logic PR Control	0.41 %	0.47 %	0.51 %	3.87 %	3.53 %	3.60 %

Table 5.5: Comparison of the THDs for all control schemes tested in the experimental setup.

From looking at the table, it can be somewhat difficult to figure out the actual improvement for each of the control schemes compared to the conventional PI control scheme. Therefore, Table 5.6 shows the percentage-wise improvement for each of the control schemes compared to the baseline. The value listed is the additive value, meaning if the THD has been improved from 0.5 % to 0.4 %, the improvement will show as 0.1 % in the table below. The percentage-wise improvement values are calculated from taking the average over all gain scenarios.

	THD	
Current Control Schemes	Simulations	Laboratory
PI Control Additional HC	0.00 %	1.02 %
PR Control	0.11 %	−0.76 %
Fuzzy Logic PI Control	0.00 %	0.39 %
Fuzzy Logic PI Control Additional HC	−0.03 %	1.17 %
Fuzzy Logic PR Control	0.11 %	−0.64 %

Table 5.6: Additive percentage-wise improvements compared to the baseline conventional PI control scheme.

There is a very big distinction between the simulations and experimental results as to which control schemes provide better performances. Concluding from the simulations alone, the PR control scheme is the only way to improve the baseline performance. Compensating for additional harmonics will not yield any benefits and the fuzzy logic controller is not improving the performance whatsoever.

However, taking a look at the experimental results, the tables have turned. Here, the PR control scheme worsens the performance of the system, whereas compensating for the additional harmonics and implementing fuzzy logic control into the control schemes greatly improves the THD. The most effective way of improving the experimental setup is to add extra harmonic compensation for the 11th and 13th harmonics. Incorporating fuzzy logic into the control schemes will also decrease the THD, however not as much as the additional harmonic compensation. Combining the additional harmonic compensation with fuzzy logic controllers will overall yield the best result possible, when only evaluating the THDs.

However, the PR control schemes greatly improves the grid current in other ways. Even though the THD is higher, the phase lag has been eliminated, which should overall cause less disturbances on the grid. It is therefore quite difficult to determine which control scheme is the most optimal, since they improve the baseline model in different ways.

Section 6

Improvements and Future Work

If further work was to be made on this setup, the complications with the experimental setup need to be solved. The limitations and restrictions make it difficult to implement other types of non-linear controllers. It could be interesting to study fuzzy logic self training controllers and controllers based on neural networks. At this very moment, it does not seem likely that these types of controllers can be successfully implemented into the experimental setup.

The baseline grid currents contain a great deal of phase lag, which is not ideal. Extensive testing would be needed to locate the cause of this. It might be necessary to completely rebuild the experimental setup in hopes of removing some of the restrictiveness it contains. The phase lag could potentially be reduced by implementing a lead controller, but it is unclear if that would cause more harm to the performance.

As of now, harmonic compensation has only been tested to and including the 13^{th} harmonics. The system becomes unstable when the 17^{th} and 19^{th} harmonics are compensated. However, this could be improved upon since it might be an issue with the harmonic compensation technique performed.

Adding more measurement points throughout the setup would allow for testing of other, more comprehensive control schemes. The capacitor currents are used in many applications, being added onto the inverter currents in the control loop. This could potentially reduce the THD within the system and could help synchronise the currents to the grid.

Last, but not least, DC voltage control could be the focus of future work. Adding a separate control loop for the DC voltage is common practice and could be used to further expand the control system of the experimental setup.

Section 7

Conclusion

The objective of this thesis was to study the power control and stability of grid side converters for offshore wind power systems. The underlying basis for the thesis was to evaluate and improve upon a baseline experimental model.

In order to understand and evaluate the performances of different control schemes for a grid-connected inverter, it is necessary to understand the topology and acquire technical knowledge about the wind power system. It was explained back in Chapter 2 that there are three main types of wind turbine technologies. One without power electronics, one with partially rated power electronics and one with full-scale power electronics. The former is only able to regulate active power and are the cheapest solution. By adding a resistance to the generator rotor, the second type allows for control of both active- and reactive power. However, the third type is the best technical solution, since it enables very fast regulation of both active- and reactive power due to the generator being decoupled from the grid by a DC-link. This is the type of system that is used in this thesis. The conversion from DC to AC is done with a voltage source inverter, an LCL filter, space vector pulse-width modulation and a current control loop.

Different control schemes were evaluated and tested in this thesis. The PI current control scheme functioned as the baseline model, for which the goal was to improve the performance thereof. The harmonic compensation in the baseline was done for the 5^{th} and 7^{th} harmonics. One of the ways to improve the performance was to compensate for additional harmonics, wherefore the 11^{th} and 13^{th} harmonics were included in the harmonic compensation. Adding the additional harmonic compensation proved to be the most effective way to reduce the THD. The additional harmonic compensation alone reduced the THD by a percentage point.

Implementing fuzzy logic controllers also greatly decreased the THD of the baseline by approximately 0.4 percentage points. The fuzzy logic controllers had to be build from scratch, since the restrictiveness of the experimental setup did not allow for the Fuzzy Logic Toolbox controller in Simulink to be implemented.

Contrary to simulation results, the PR control scheme did not improve the THDs of the baseline model. The THD increased with 0.76 percentage points in the experimental setup. However, the grid currents were found to be heavily out of phase with the reference currents. The grid currents where in phase with the reference currents in the PR control schemes. Even though the THD increased, the performance of the PR control scheme could be seen as having improved the baseline model, since having a phase lag is not optimal. The reason for the phase lag in the PI control schemes is uncertain, but it indicates that there are some issues with the performance of the baseline model.

The goal of the thesis was to improve the current control scheme of the baseline. The results and conclusion of the control scheme performances should therefore primarily lie on the THD of the grid currents. By combining the additional harmonic compensation with the implementation of fuzzy logic controllers to regulate the proportional- and integral gains of the current controllers, the THD improved by 1.17 percentage points from the baseline model. The lowest amount of THD obtained was 1.81 %, which is a significant improvement.

Section 8

References

[1] Z. Chen; E. Spooner. Voltage source inverters for high-power variable-voltage dc power sources. Technical report, 2001.

[2] J. YingYing; W. XuDong; M. LiangLiang; Y. ShuCai; Z. HaiXing. Application and simulation of svpwm in three phase inverter. Technical report, 2011.

[3] N/A. Chapter 4 space vector pulse width modulation. URL: `https://www.researchgate.net/profile/Mohamed_Mourad_Lafifi/post/How_to_find_switching_angles_from_nearest_level_control_technique_in_multilevel_inverter/attachment/59d6463c79197b80779a1411/AS%3A456910638981125%401485947393821/download/09_chapter+4+SPACE+VECTOR+PULSE+WIDTH+MODULATION.pdf`. Accessed: 6/6-2018.

[4] Wikipedia. Space vector modulation. URL: `https://en.wikipedia.org/wiki/Space_vector_modulation`, 2018. Accessed: 6/6-2018.

[5] MathWorks. Pwm generator. URL: `https://se.mathworks.com/help/physmod/sps/powersys/ref/pwmgenerator.html`. Accessed: 6/6-2018.

[6] A. Reznik; M. Simões; A. Al-Durra; S. Muyeen. Lcl filter design and performance analysis for grid interconnected systems. Technical report, 2014.

[7] F. Blaabjerg; R. Teodorescu; M. Liserre; A. Timbus. Overview of control and grid synchronization for distributed power generation systems. Technical report, 2006.

[8] Wikipedia. Direct-quadrature-zero transformation. URL: `https://en.wikipedia.org/wiki/Direct-quadrature-zero_transformation`, 2017. Accessed: 6/6-2018.

[9] Microsemi. Park, inverse park, clarke, inverse clarke transformations mss software impementatino user guide. Technical report, 2013.

[10] T. Allaoui; M. Denaï. Decoupling and control of real and reactive power in grid-connected photovoltaic power system. Technical report, 2013.

[11] A. Timbus; R. Teodorescu; F. Blaabjerg; M. Liserre. Synchronization methods for three phase distributed power generation systems. an overview and evaluation. Technical report, 2005.

[12] MathWorks. Power (dq0, instantaneous. URL: `https://se.mathworks.com/help/physmod/sps/powersys/ref/powerdq0instantaneous.html`, 2013. Accessed: 6/6-2018.

[13] X. Yuan; W. Merk; H. Stemmler; J. Allmeling. Stationary-frame generalized integrators for current control of active power filters with zero steady-state error for current harmonics of concern under unbalanced and distorted operating conditions. Technical report, 2002.

[14] Electronics Turtorials. Harmonics. URL: `https://www.electronics-tutorials.ws/accircuits/harmonics.html`. Accessed: 6/6-2018.

[15] All About Circuits. Harmonic phase sequences. URL: https://www.allaboutcircuits.com/textbook/alternating-current/chpt-10/harmonic-phase-sequences/. Accessed: 6/6-2018.

[16] E. Torstensson. Comparison of schemes for windup protectiond. Technical report, 2013.

[17] E. Twining; D. Holmes. Modelling grid-connected voltage source inverter operation. Technical report.

[18] K. Jalili; S. Bernet. Design of lcl filters of active-front-end two-level voltage-source converters. Technical report, 2009.

[19] M. Liang; T. Zheng. Synchronous pi control for three-phase grid-connected photovoltaic inverter. Technical report, 2010.

[20] National Instruments. Pid theory explained. URL: http://www.ni.com/white-paper/3782/en/, 2011. Accessed: 12/5-2018.

[21] R. Teodorescu; F. Blaabjerg. Flexible control of small wind turbines with grid failure detection operating in stand-alone and grid-connected mode. Technical report, 2004.

[22] X. Zhang; J. Spencer; J. Guerrero. Small-signal modeling of digitally controlled grid-connected inverters with lcl filters. Technical report, 2013.

[23] Wikipedia. Nyquist stability criterion. URL: https://en.wikipedia.org/wiki/Nyquist_stability_criterion, 2018. Accessed: 23/5-2018.

[24] Brian Douglas. Nyquist stability criterion, part 1. URL: https://www.youtube.com/watch?v=sof3meN96MA, 2013. Accessed: 23/5-2018.

[25] O. Kaplan; N. Altin. Fuzzy pi controlled inverter for grid inveractive renewable energy systems. Technical report, 2015.

[26] L. Mirkin; Z. Palmor. Control issues in systems with loop delays. Technical report, 2005.

[27] MathWorks. pade. URL: https://se.mathworks.com/help/control/ref/pade.html. Accessed: 24/5-2018.

[28] Venable Instruments. Specify gain and phase margins on all your loops. URL: https://venable.biz/technical-publications/specify-gain-phase-margins-loops/. Accessed: 25/5-2018.

[29] R. Teodorescu; F. Blaabjerg; U. Borup; M. Liserre. A new control structure for grid-connected lcl pv inverters with zero steady-state error and selective harmonic compensation. Technical report, 2004.

[30] R. Teodorescu; F. Blaabjerg; M. Liserre; P. Loh. Proportional-resonant controllers and filters for grid-connected voltage-source converters. Technical report, 2006.

[31] A. Yepes; F. Freijedo; Ó. López; J. Doval-Gandoy. High-performance digital resonant controllers implemented with two integrators. Technical report, 2011.

[32] Stanford Encyclopedia of Philosophy. Fuzzy logic. URL: https://plato.stanford.edu/entries/logic-fuzzy/. Accessed: 30/5-2018.

[33] MathWorks. What is fuzzy logic? URL: https://se.mathworks.com/help/fuzzy/what-is-fuzzy-logic.html. Accessed: 30/5-2018.

[34] MathWorks. Foundations of fuzzy logic. URL: https://se.mathworks.com/help/fuzzy/foundations-of-fuzzy-logic.html#bp78l70-5. Accessed: 30/5-2018.

[35] MathWorks. Fuzzy inference process. URL: https://se.mathworks.com/help/fuzzy/fuzzy-inference-process.html. Accessed: 30/5-2018.

[36] MathWorks. Comparison of sugeno and mamdani systems. URL: https://se.mathworks.com/help/fuzzy/comparison-of-sugeno-and-mamdani-systems.html. Accessed: 30/5-2018.

[37] G. Rao; R. Sankar. Fuzzy-pi control of grid interact three-phase voltage source inverter. Technical report, 2017.

Appendix A

Appendix

A.1 System Parameters

Parameters	Value	Variable
Fundamental grid frequency	50 Hz	freq_0
Switching frequency	8 kHz	f_{sw}
Sampling time (simulations	$1.25{\cdot}10^(-6)$ s	T_{s}
DC voltage	666 V	V_{DC}
Grid voltage	380 V	V_{g}
Inverter side inductance	1.8 mH	$\mathrm{L}_{\mathrm{inv}}$
Inverter side resistance	0.1 Ω	$\mathrm{R}_{\mathrm{inv}}$
Filter capacitance	14 μF	C_{f}
Grid side inductance	2 mH	L_{g}
Grid side resistance	1.4 Ω	R_{g}
Damping ratio	0.7	ζ
Settling time PLL	0.1 s	$\mathrm{T}_{\mathrm{set}}$
DC voltage	666 V	V_{DC}

Table A.1: System parameters for grid-connected inverter.

A.2 PI Tuning KP=20 KI=1500 Minimum Delay

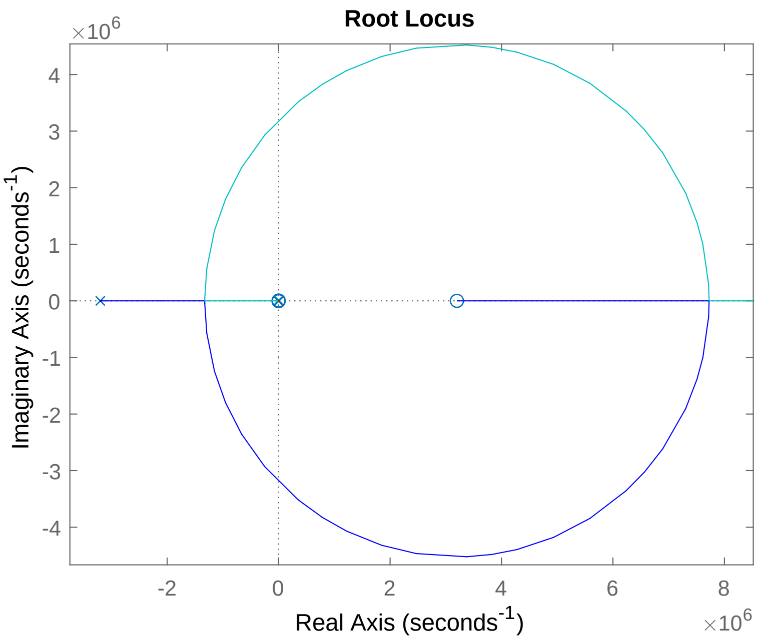

Figure A.1: Root locus for open-loop system using Padé approximation with $K_P = 20, K_I = 1500, \tau_d = T_s/2$.

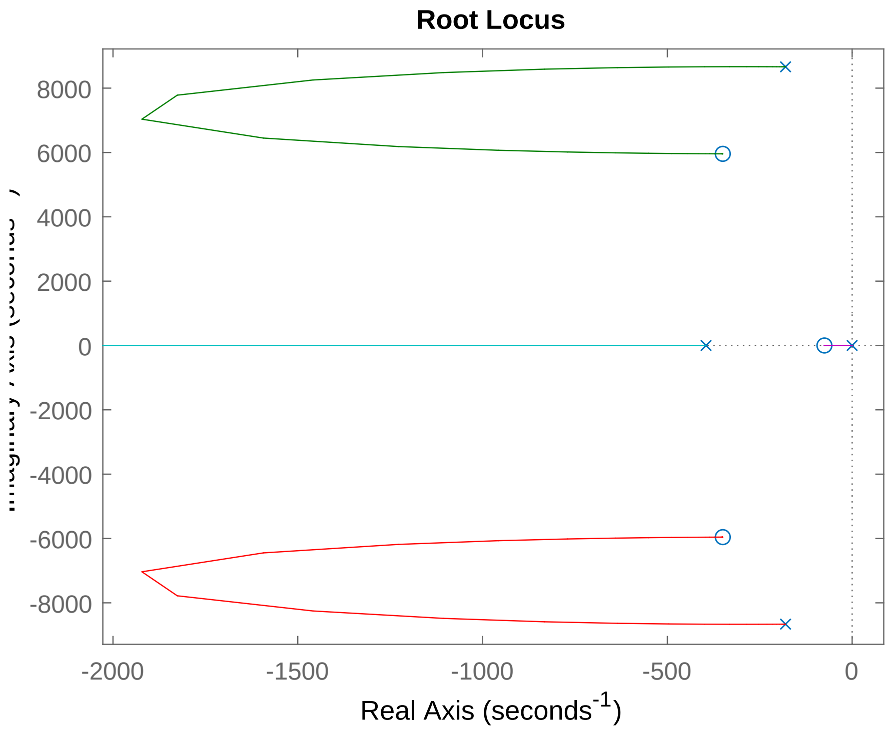

Figure A.2: Zoomed in root locus for open-loop system using Padé approximation with $K_P = 20, K_I = 1500, \tau_d = T_s/2$.

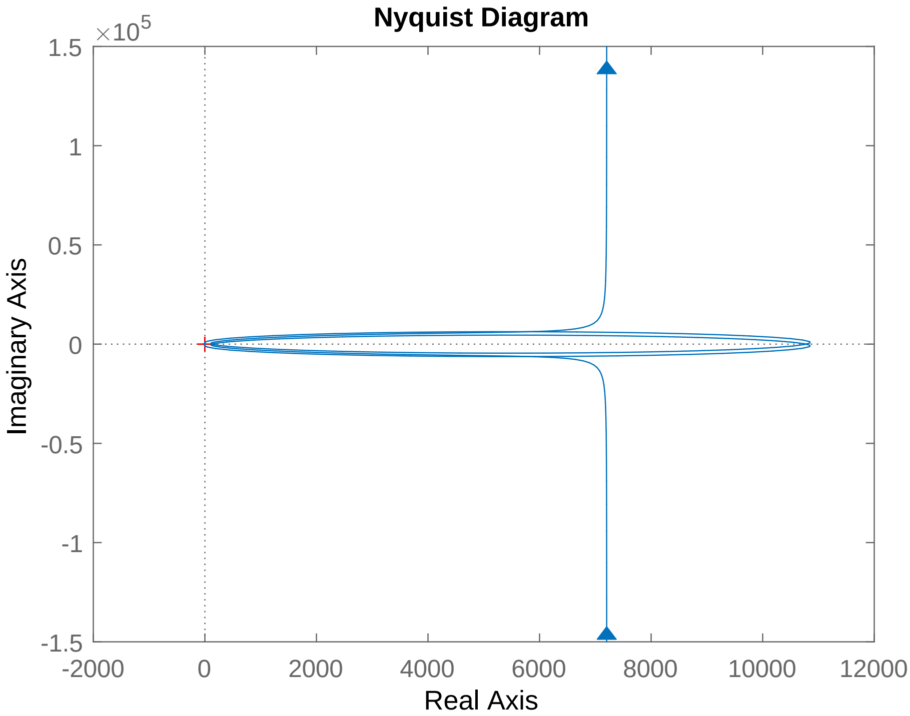

Figure A.3: Nyquist plot for open-loop system with $K_P = 20, K_I = 1500, \tau_d = T_s/2$.

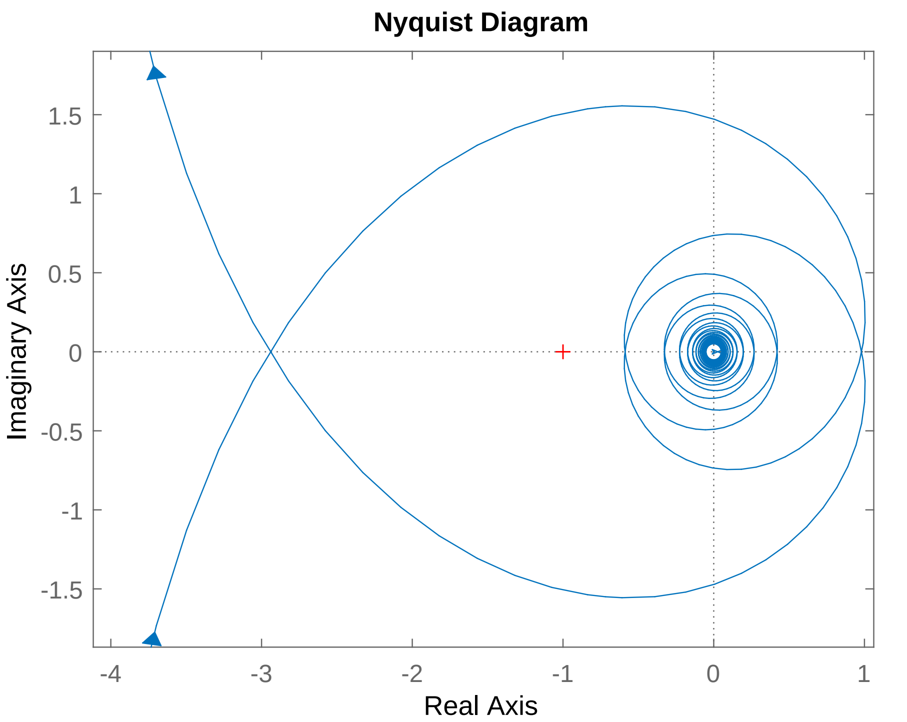

Figure A.4: Zoomed in Nyquist plot for open-loop system with $K_P = 20, K_I = 1500, \tau_d = T_s/2$.

A.3 PI Tuning KP=20 KI=1500 New Delay

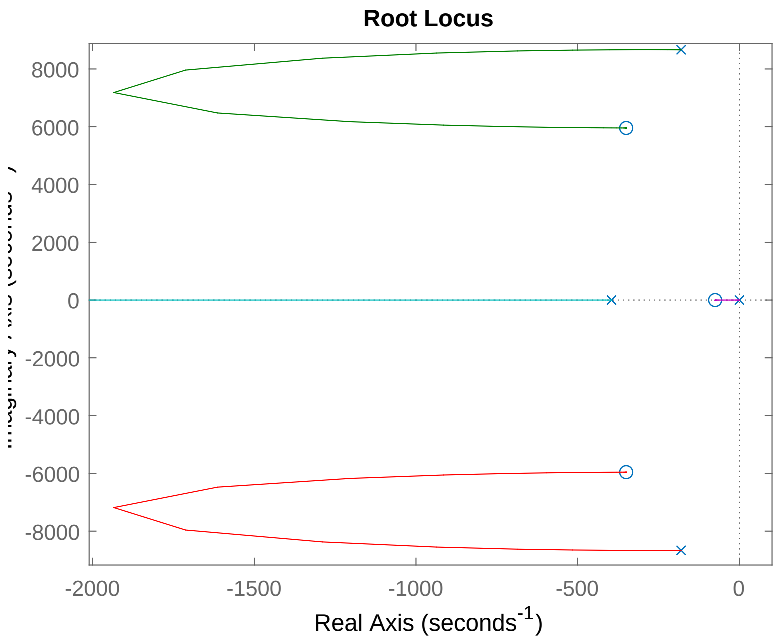

Figure A.5: Zoomed in root locus for open-loop system using Padé approximation with $K_P = 20, K_I = 1500, \tau_d = T_s/20$.

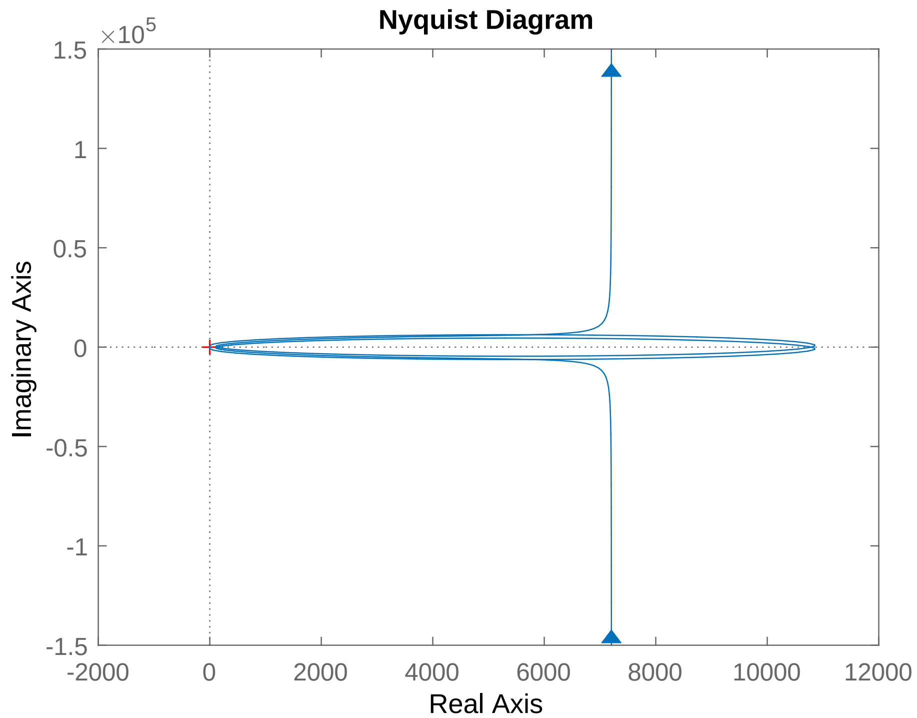

Figure A.6: Nyquist plot for open-loop system with $K_P = 20, K_I = 1500, \tau_d = T_s/20$.

A.4 PI Tuning KP=15/10 KI=2000/2500 New Delay

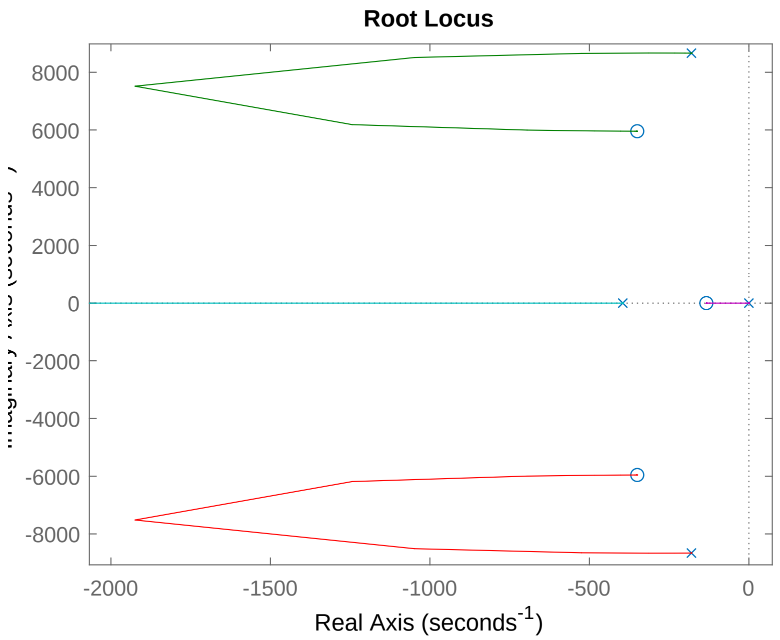

Figure A.7: Zoomed in root locus for open-loop system using Padé approximation with $K_P = 15, K_I = 2000, \tau_d = T_s/20$.

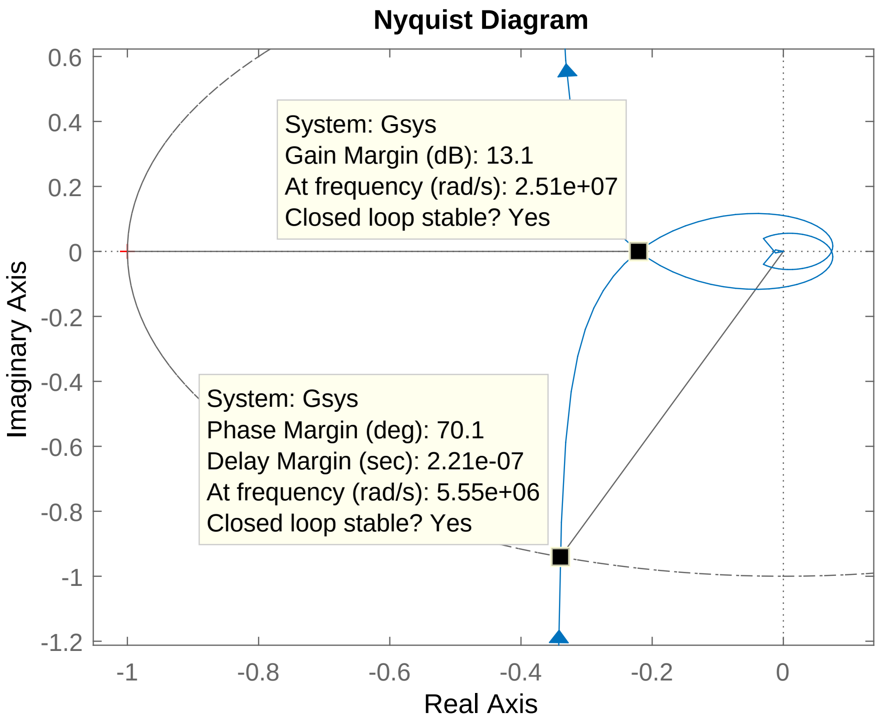

Figure A.8: Zoomed in Nyquist plot for open-loop system with $K_P = 15, K_I = 2000, \tau_d = T_s/20$.

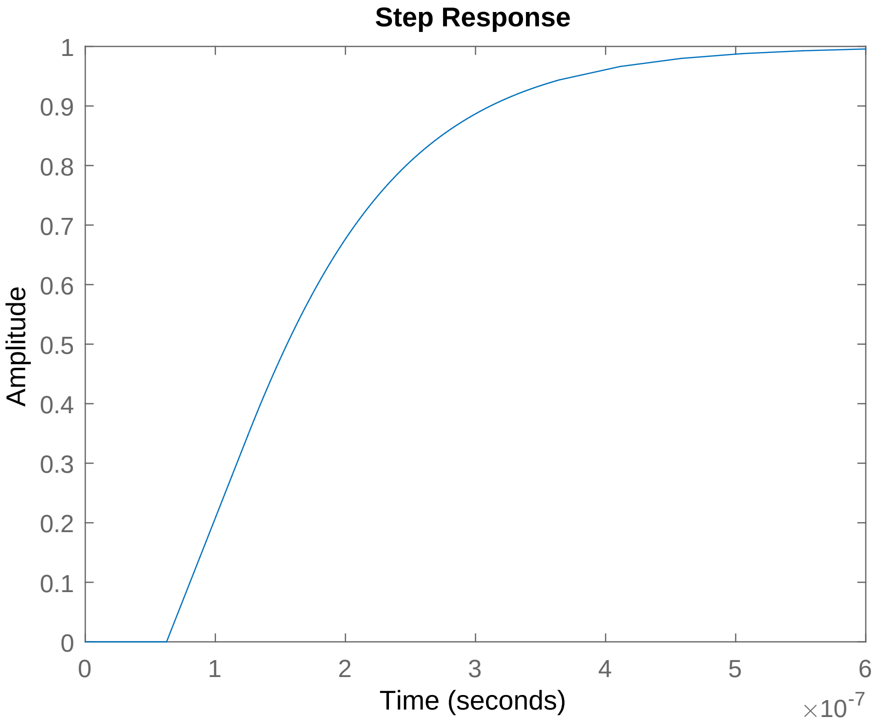

Figure A.9: Step response for closed-loop system with $K_P = 15, K_I = 2000, \tau_d = T_s/20$.

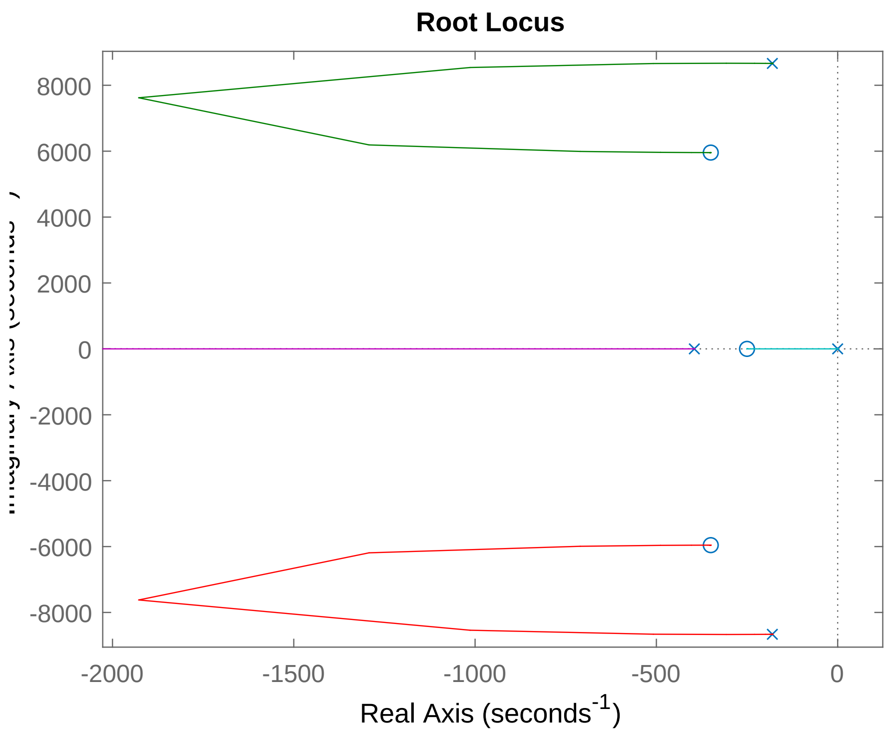

Figure A.10: Zoomed in root locus for open-loop system using Padé approximation with $K_P = 10, K_I = 2500, \tau_d = T_s/20$.

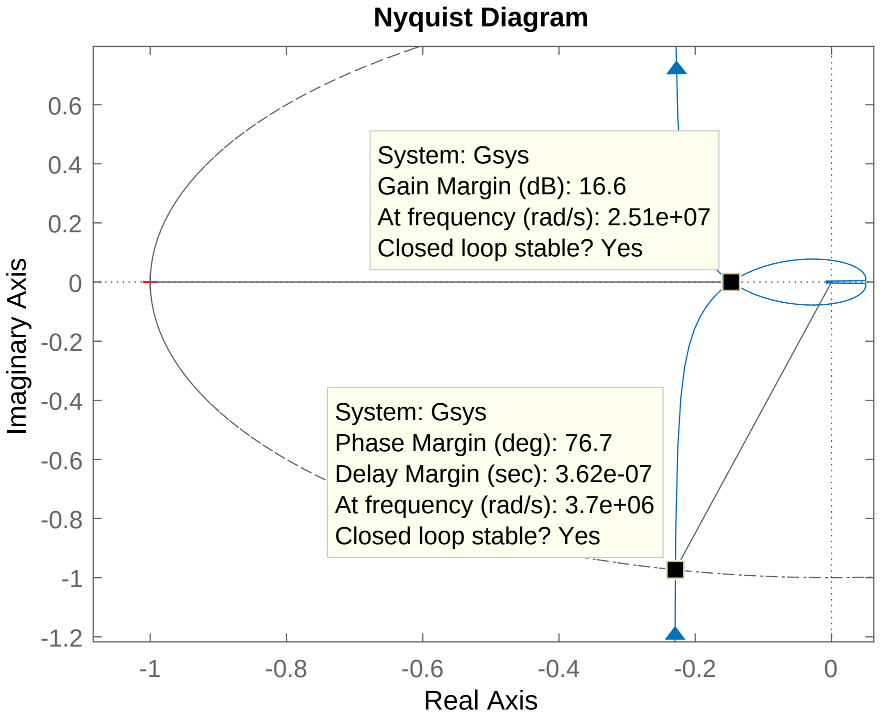

Figure A.11: Zoomed in Nyquist plot for open-loop system with $K_P = 10, K_I = 2500, \tau_d = T_s/20$.

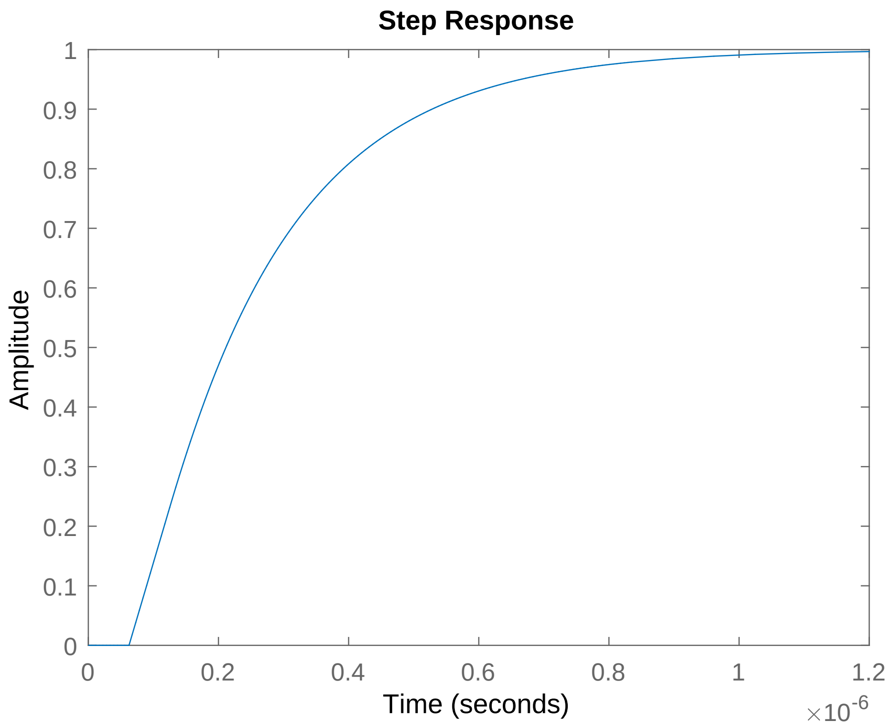

Figure A.12: Step response for closed-loop system with $K_P = 10, K_I = 2500, \tau_d = T_s/20$.

A.5 PR Tuning

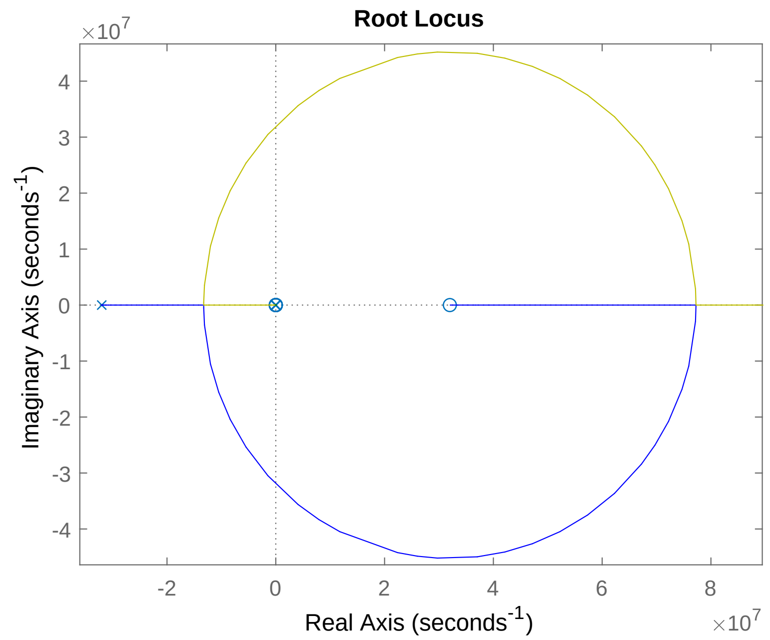

Figure A.13: Zoomed in root locus for proportional resonant open-loop system using Padé approximation with $K_P = 20, K_I = 1500$.

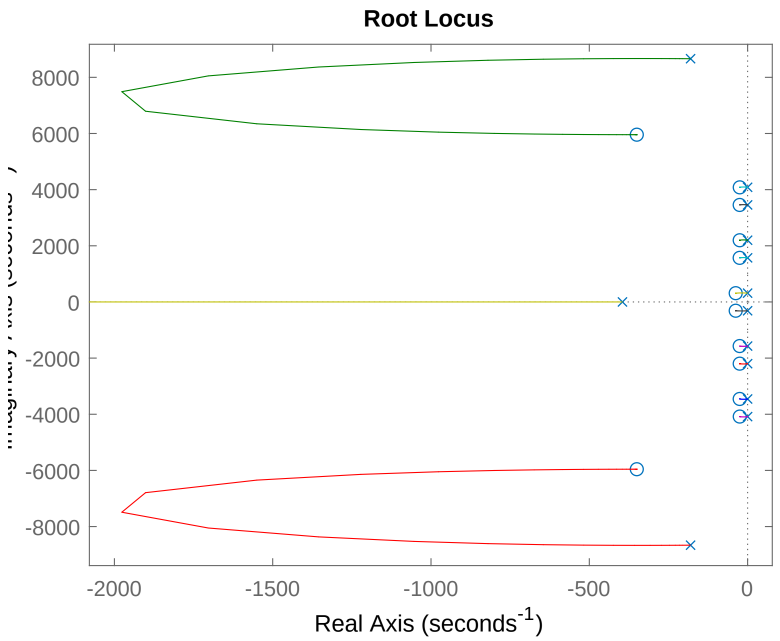

Figure A.14: Root locus for proportional resonant open-loop system using Padé approximation with $K_P = 20, K_I = 1500$.

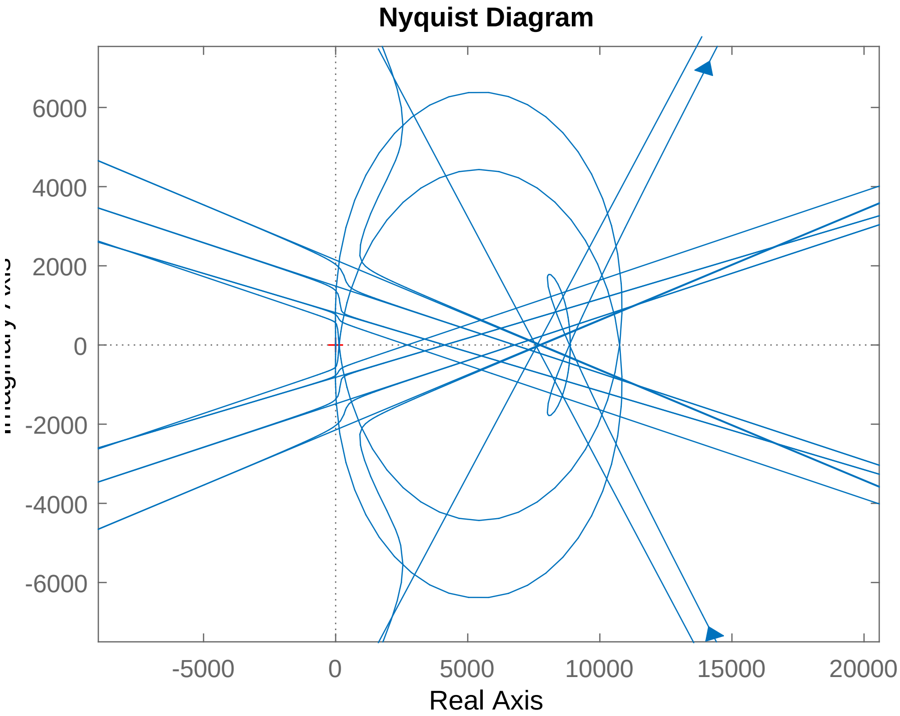

Figure A.15: Nyquist plot for proportional resonant open-loop system with $K_P = 20, K_I = 1500$.

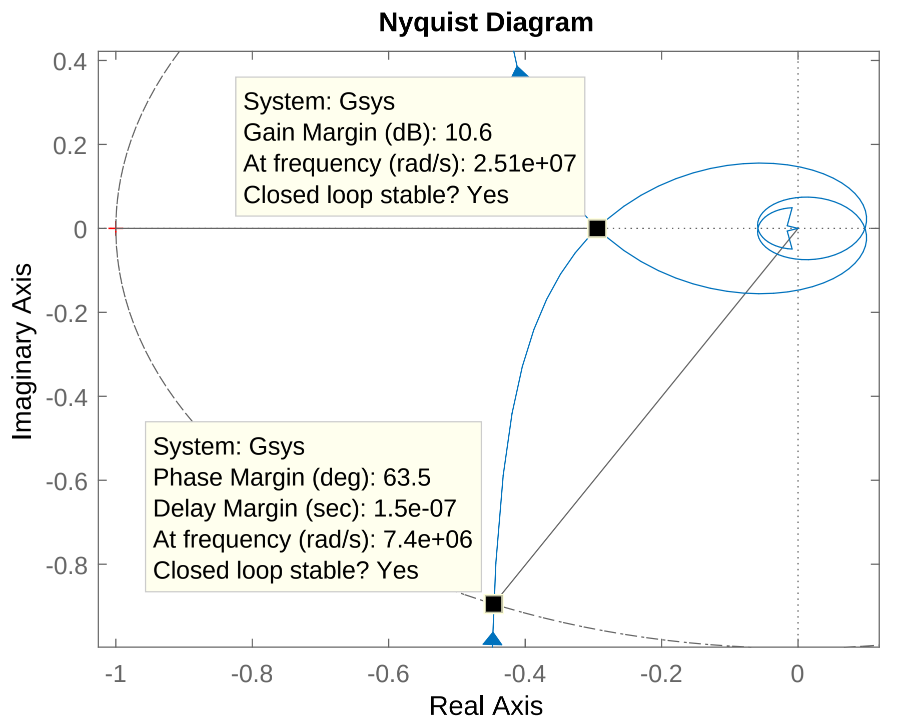

Figure A.16: Zoomed in Nyquist plot for proportional resonant open-loop system with $K_P = 20, K_I = 1500$.

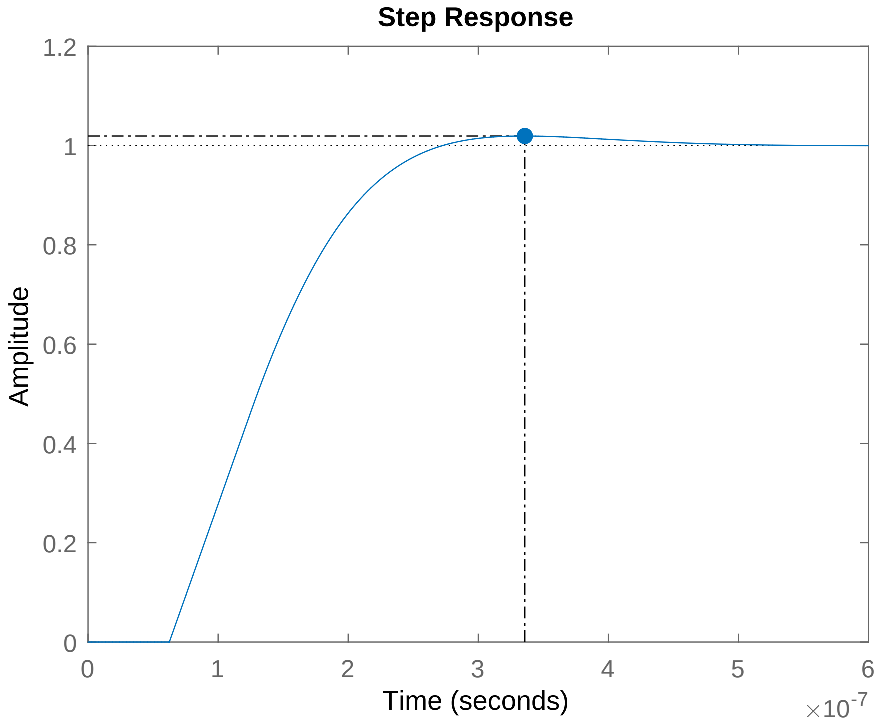

Figure A.17: Step response for proportional resonant closed-loop system with $K_P = 20, K_I = 1500$.

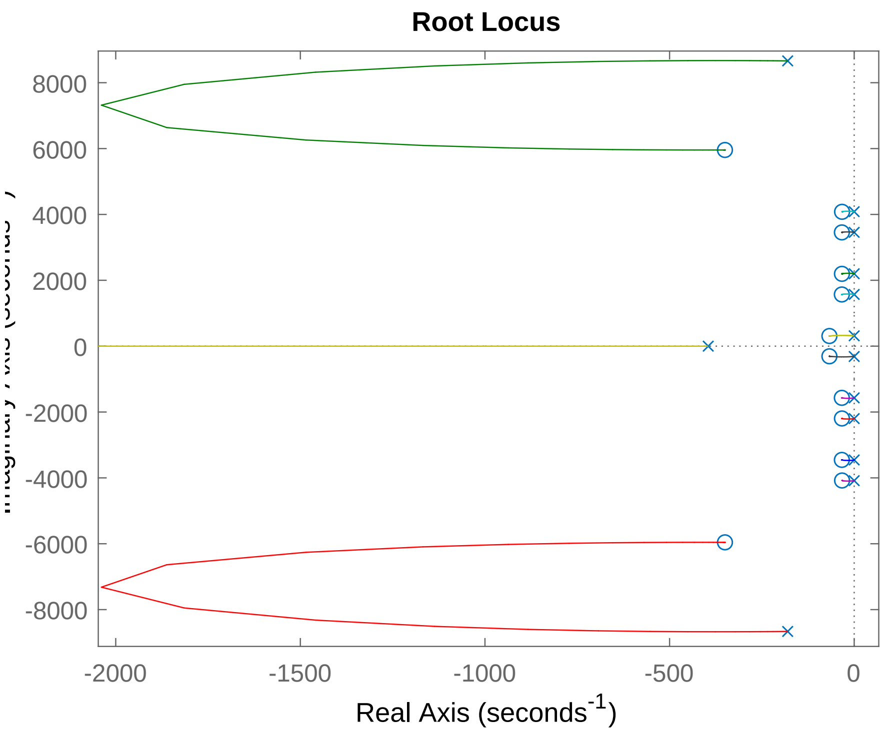

Figure A.18: Root locus for proportional resonant open-loop system using Padé approximation with $K_P = 15$, $K_I = 2000$.

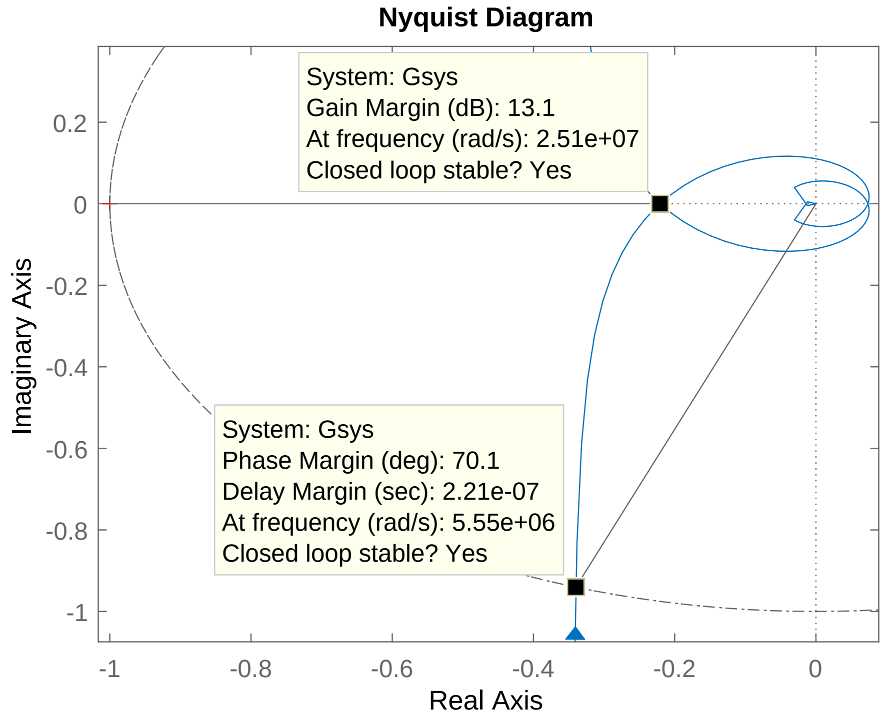

Figure A.19: Zoomed in Nyquist plot for proportional resonant open-loop system with $K_P = 15, K_I = 2000$.

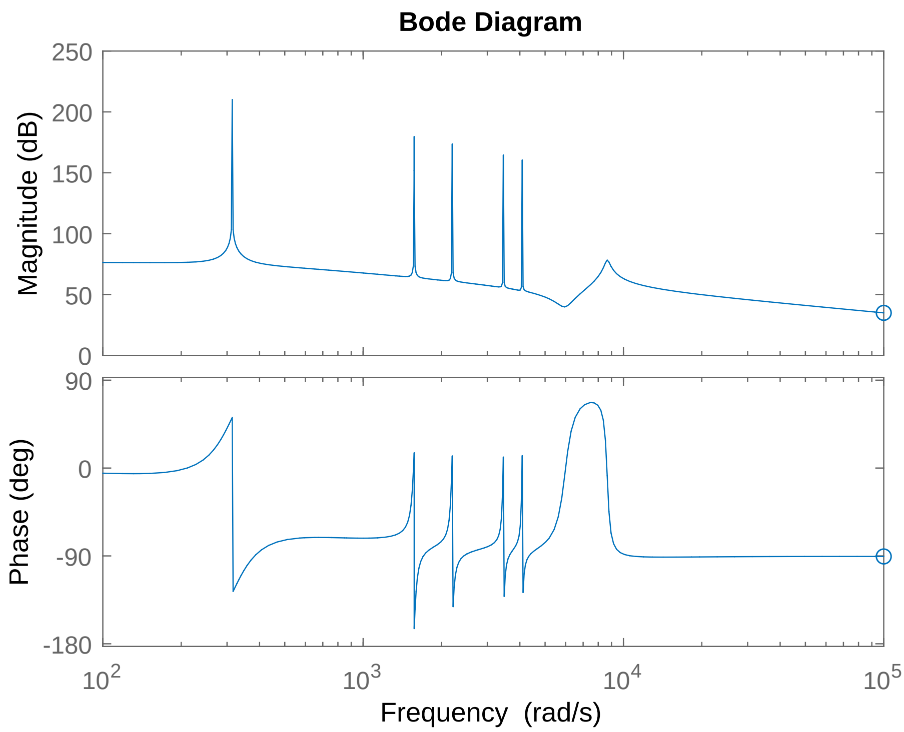

Figure A.20: Bode plot for PR control scheme compensating 5th, 7th, 11th, and 13th harmonic for $K_P = 15$, $K_I = 2000$.

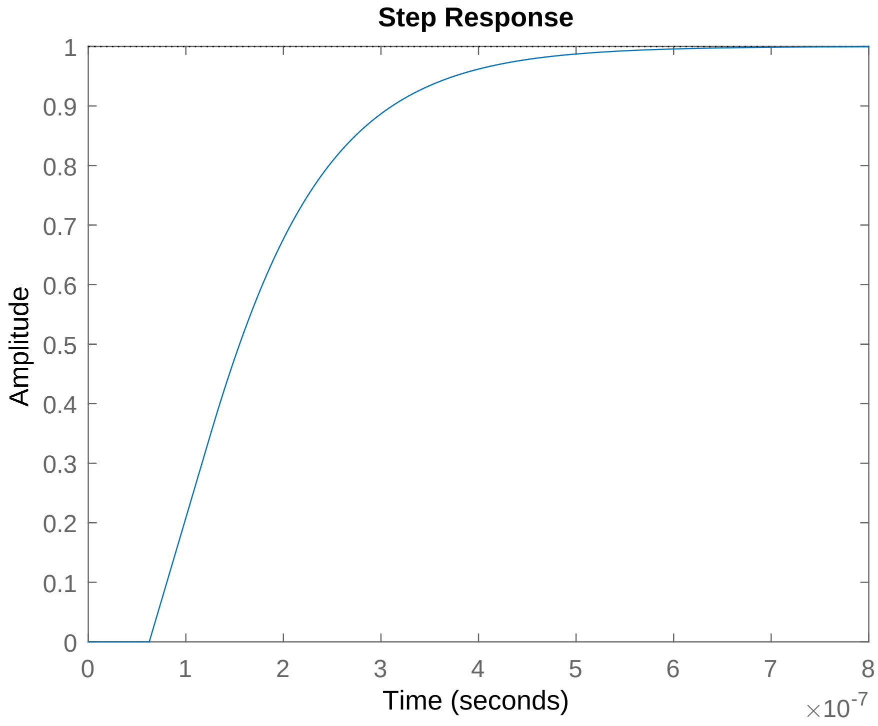

Figure A.21: Step response for proportional resonant closed-loop system with $K_P = 15$, $K_I = 2000$.

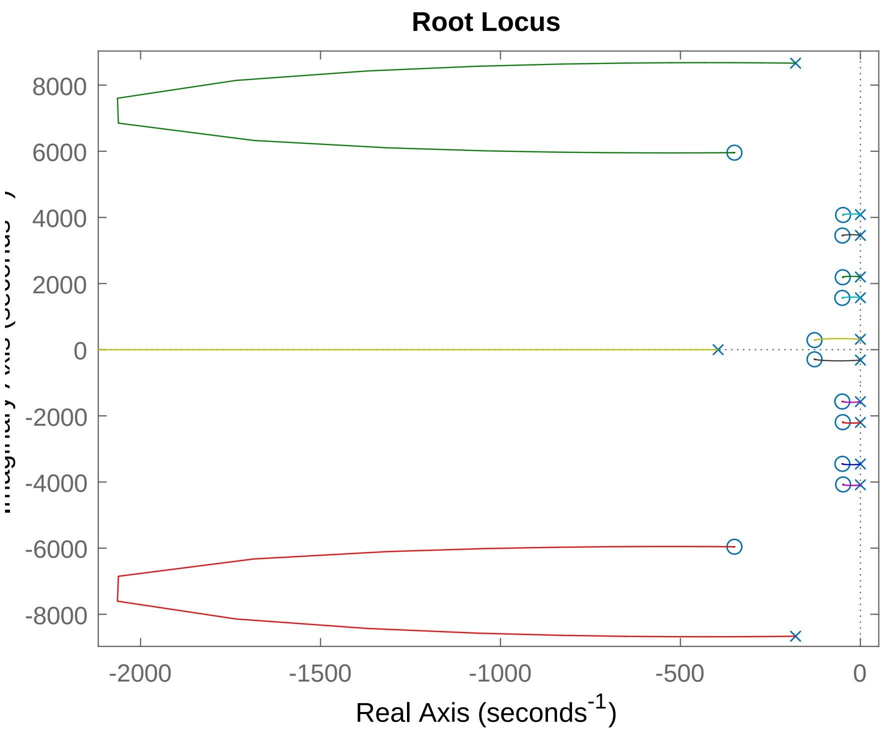

Figure A.22: Root locus for proportional resonant open-loop system using Padé approximation with $K_P = 10$, $K_I = 2500$.

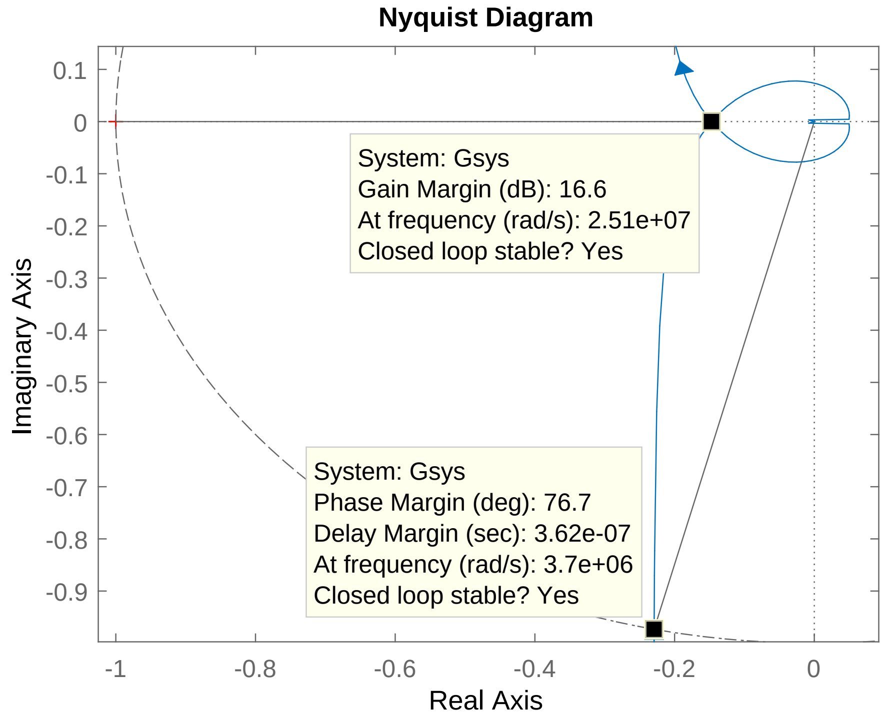

Figure A.23: Zoomed in Nyquist plot for proportional resonant open-loop system with $K_P = 10$, $K_I = 2500$.

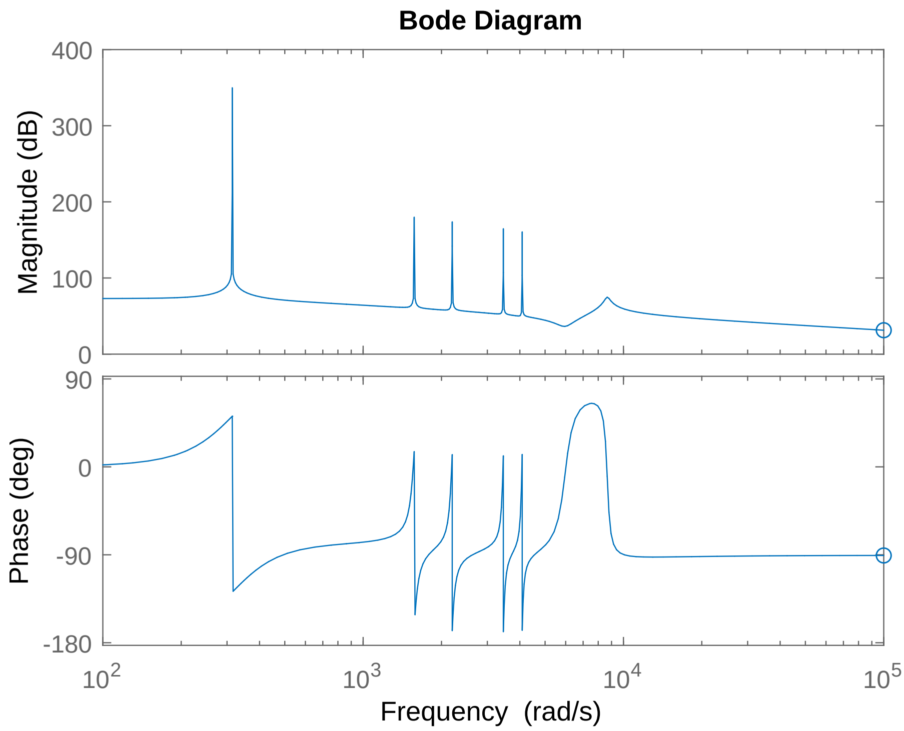

Figure A.24: Bode plot for PR control scheme compensating 5th, 7th, 11th, and 13th harmonic for $K_P = 10$, $K_I = 2500$.

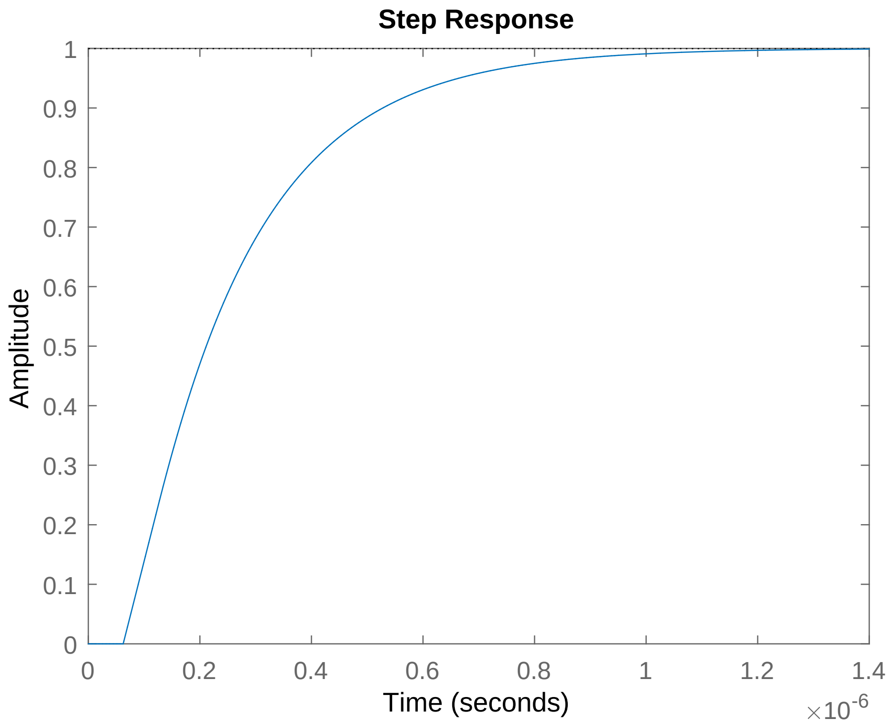

Figure A.25: Step response for proportional resonant closed-loop system with $K_P = 10$, $K_I = 2500$.

A.6 Fuzzy Logic Tuning

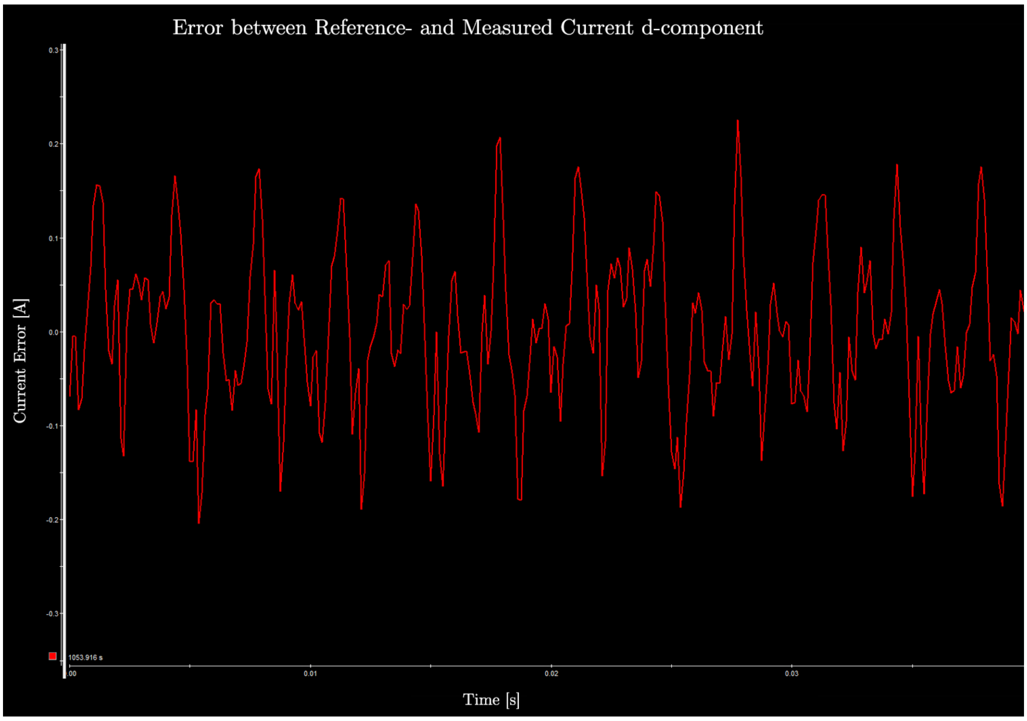

Figure A.26: Error of reference- and measured currents in d-frame for PI control scheme.

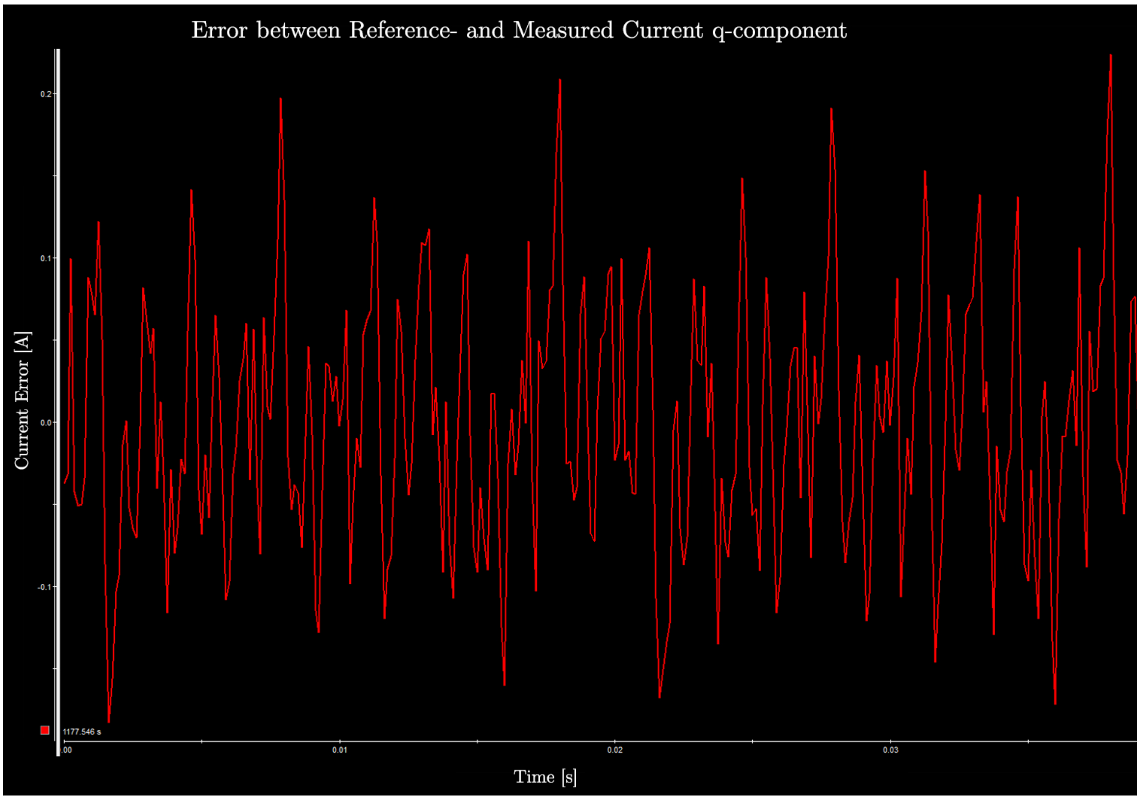

Figure A.27: Error of reference- and measured currents in q-frame for PI control scheme.

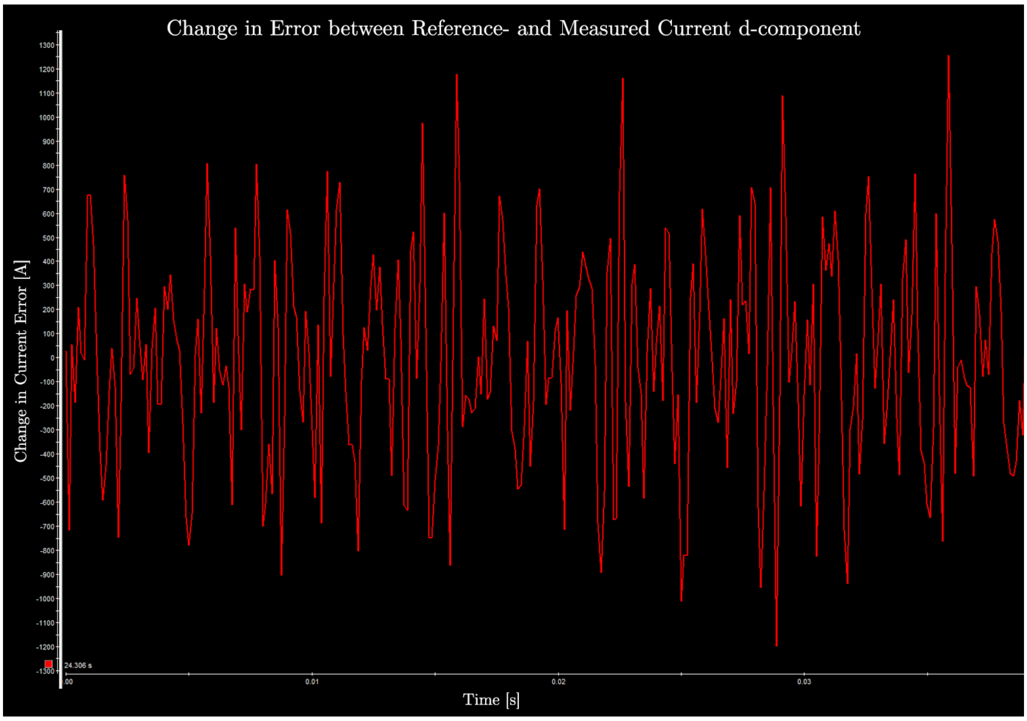

Figure A.28: Change in error of reference- and measured currents in d-frame for PI control scheme.

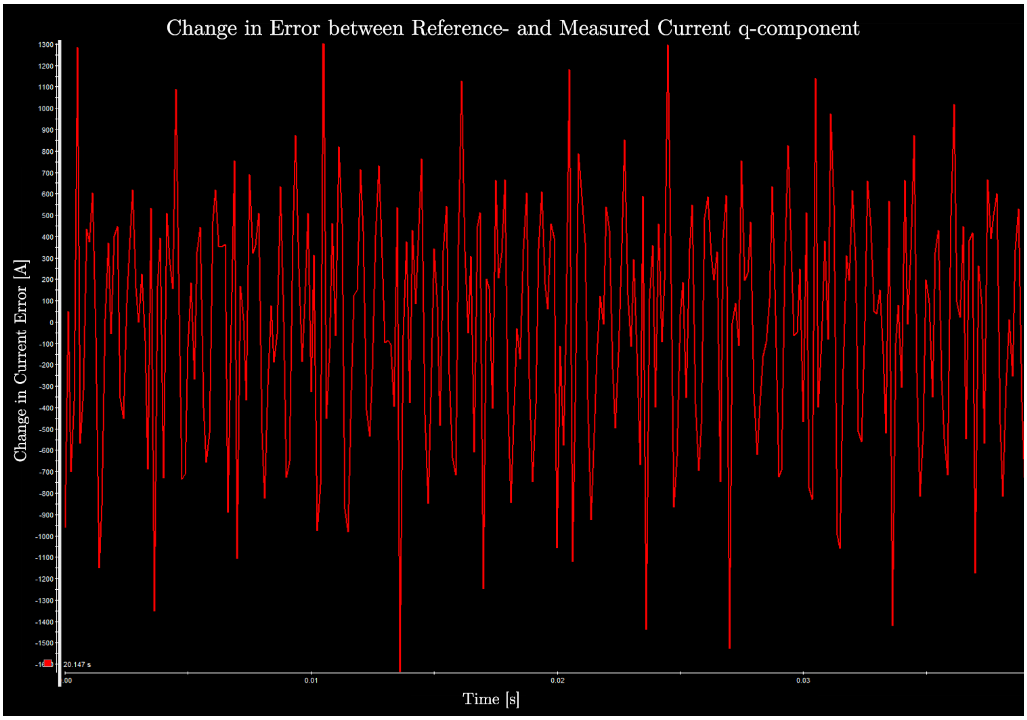

Figure A.29: Change in error of reference- and measured currents in q-frame for PI control scheme.

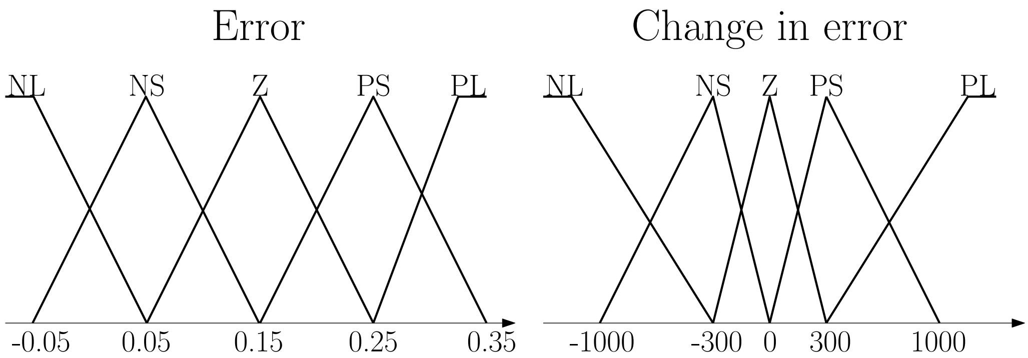

Figure A.30: Membership functions for error and change in error for PR control scheme in experimental setup.

A.7 Simulations

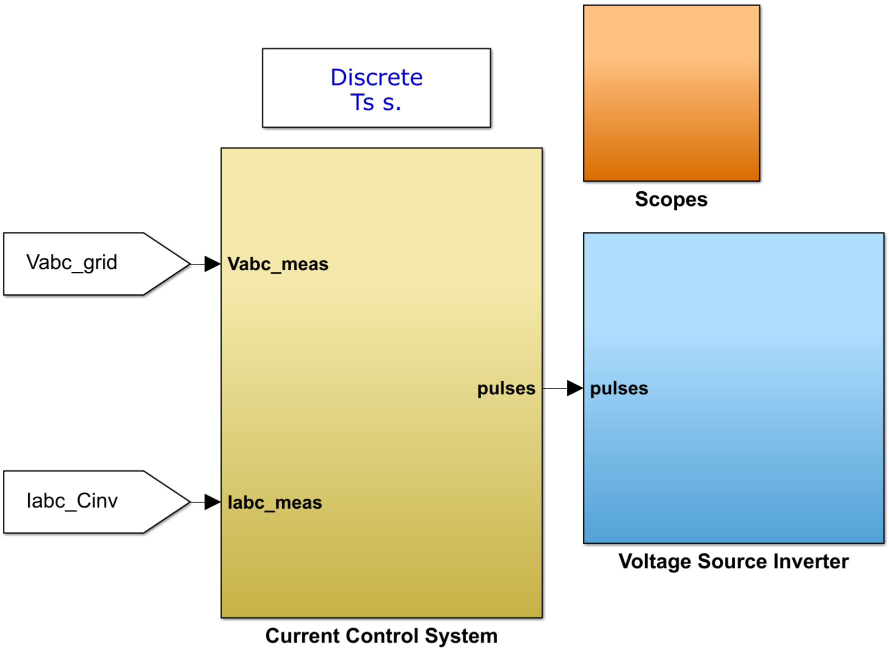

Figure A.31: Overview of the simulation components. All simulations are comprised of this layout.

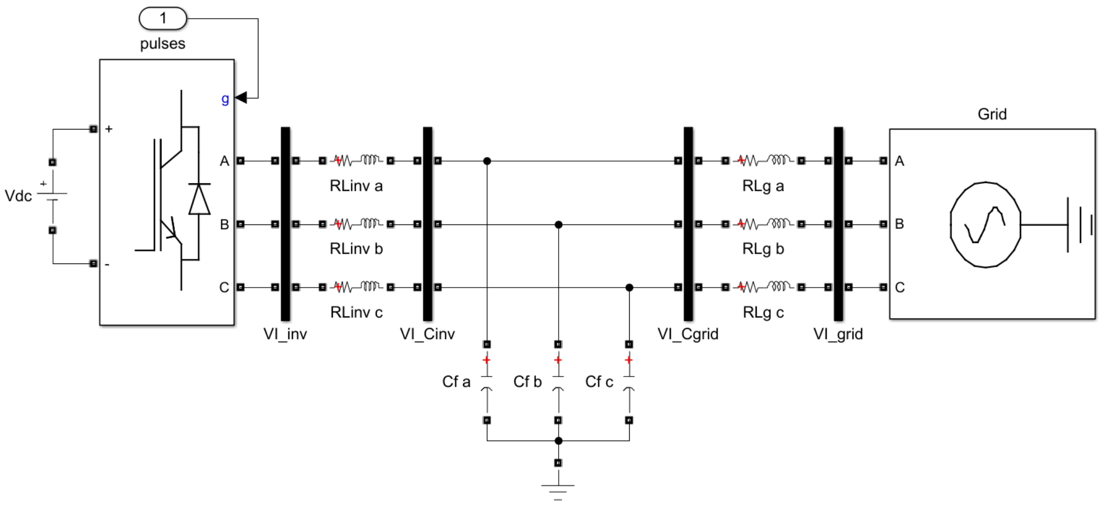

Figure A.32: Overview of the grid-connected voltage source inverter block in the simulations.

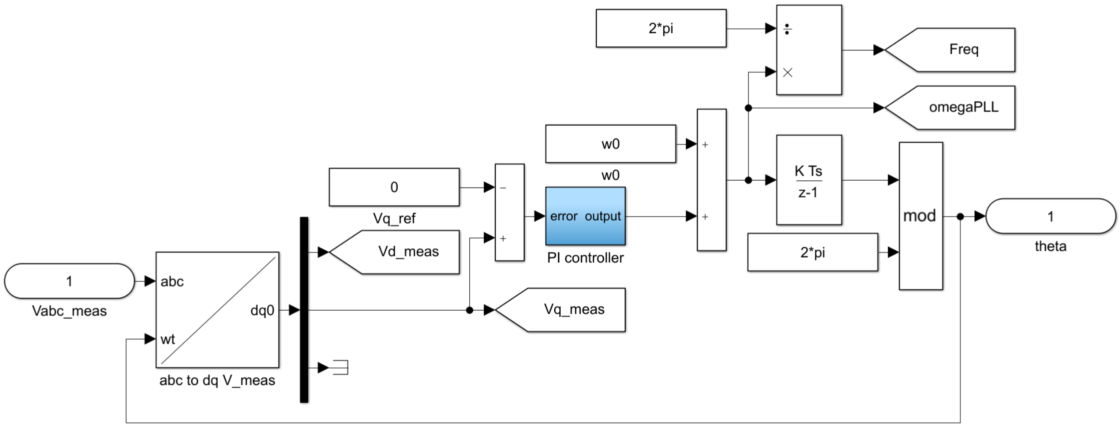

Figure A.33: Block diagram of the phase-locked loop used throughout the simulations.

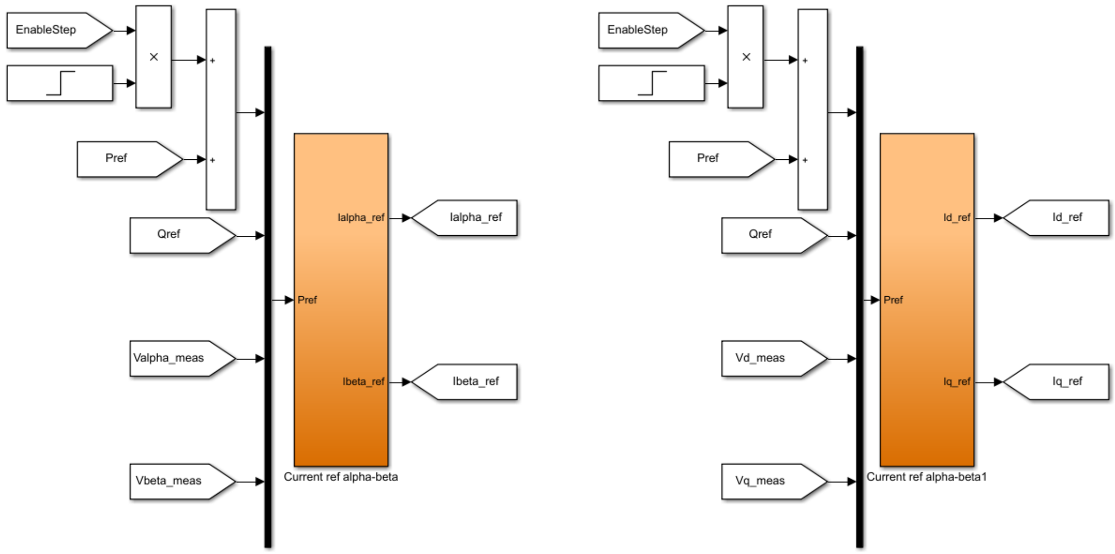

Figure A.34: The current reference power calculations used in the simulations.

A.8 PI Control Simulations

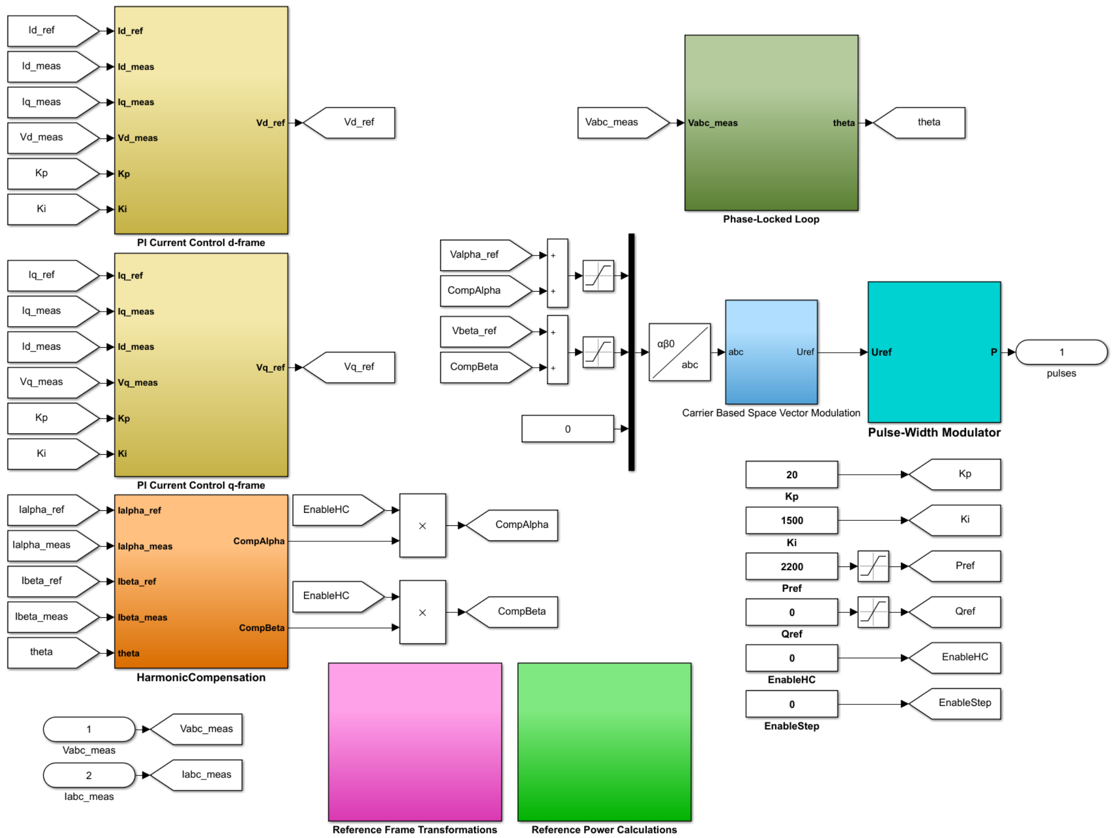

Figure A.35: Current Control block for PI control scheme simulation.

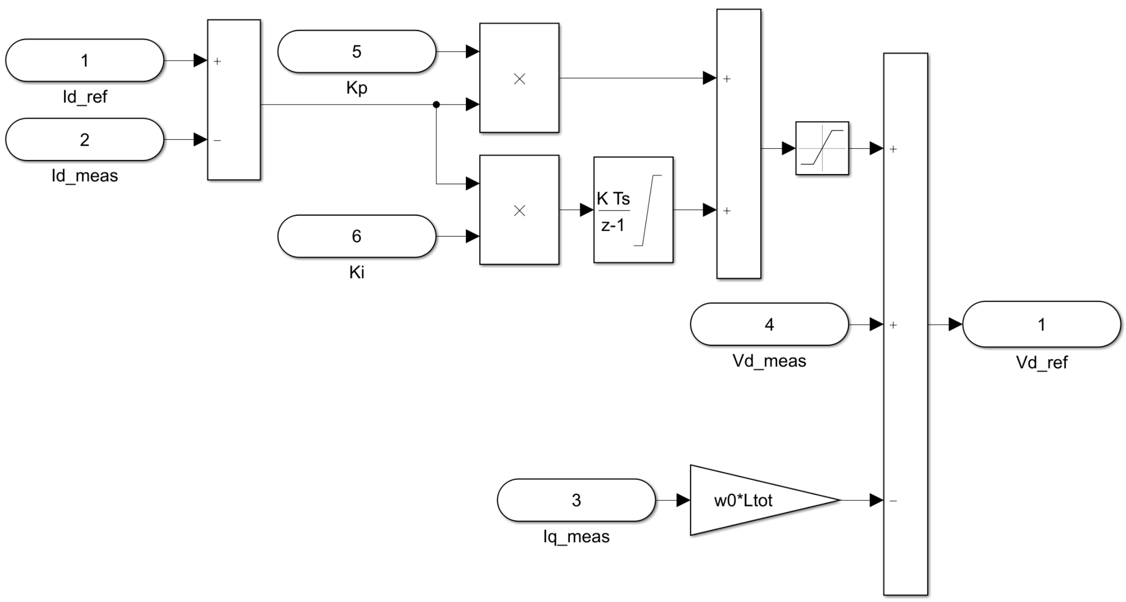

Figure A.36: Current control block diagram in simulations for PI control d-frame.

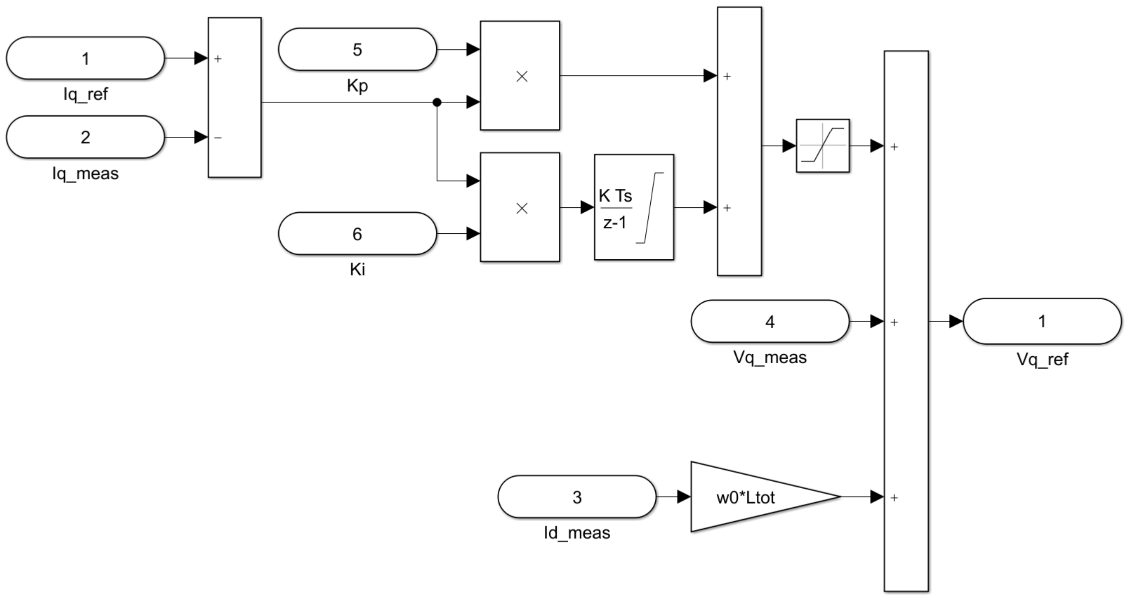

Figure A.37: Current control block diagram in simulations for PI control q-frame.

A.9 PR Control Simulations

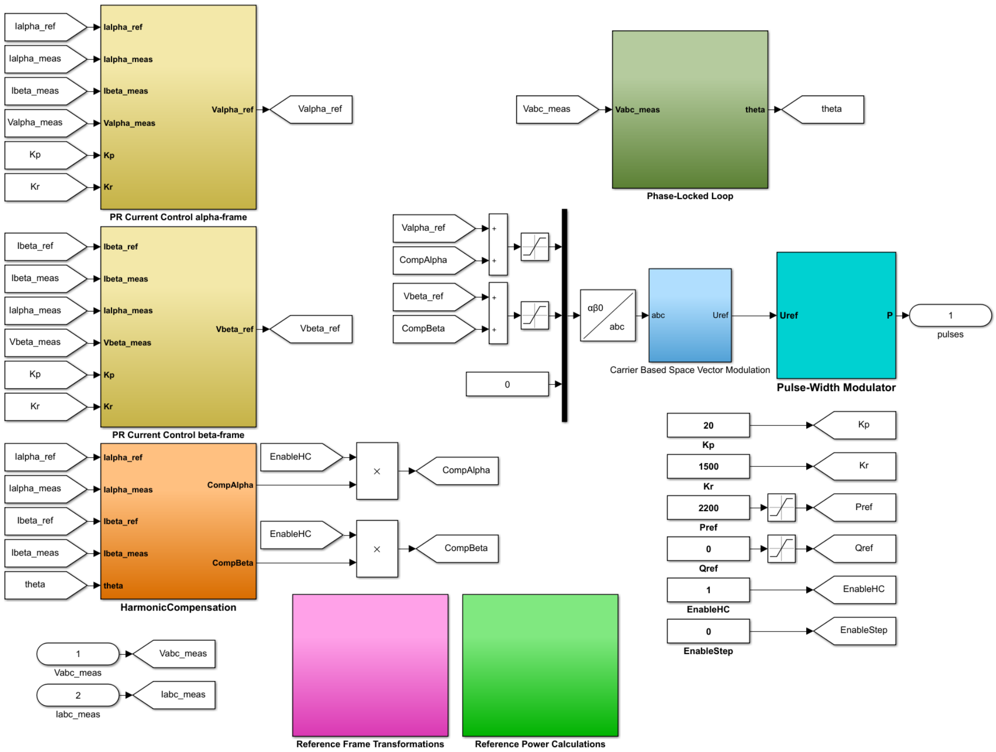

Figure A.38: Current Control block for PR control scheme simulation.

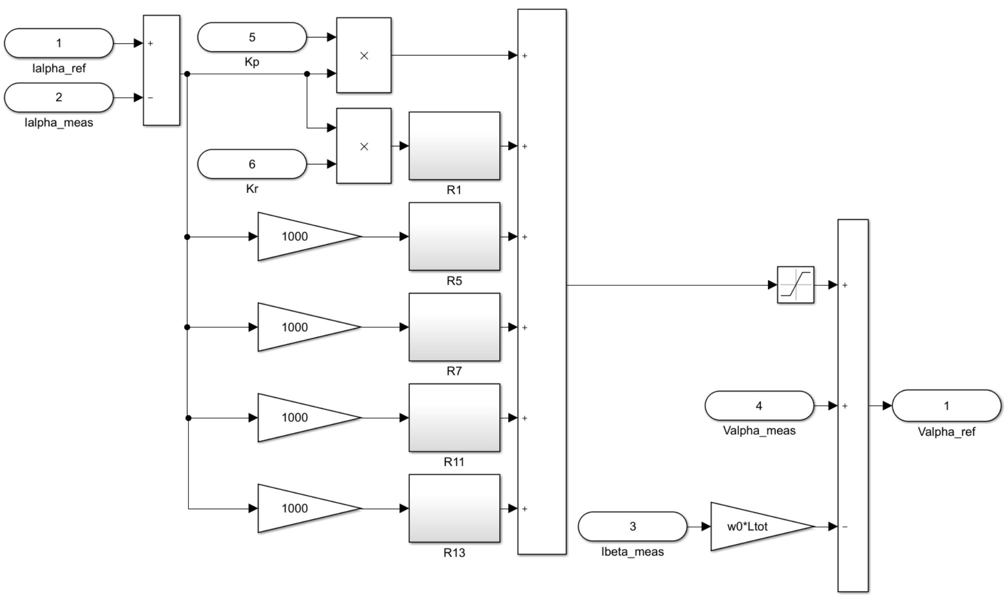

Figure A.39: Current control block diagram in simulations for PR control scheme simulation alpha-frame.

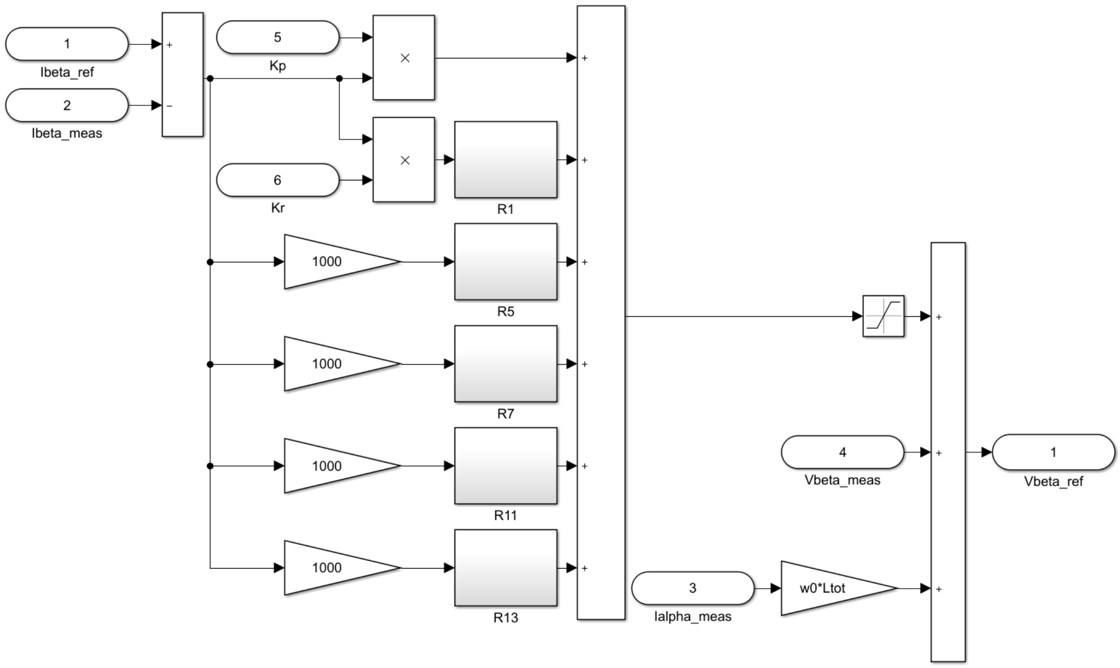

Figure A.40: Current control block diagram in simulations for PR control beta-frame.

A.10 Fuzzy Logic PI Control

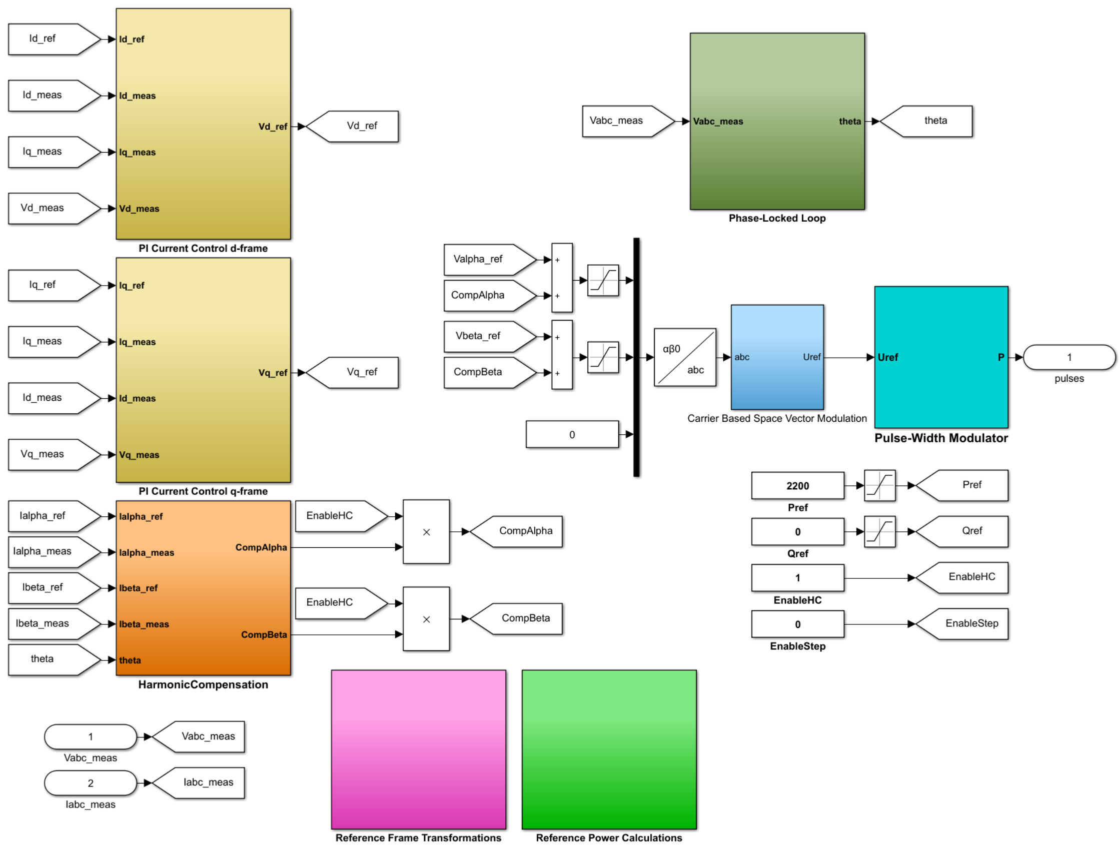

Figure A.41: Current Control block for fuzzy logic PI control scheme simulation.

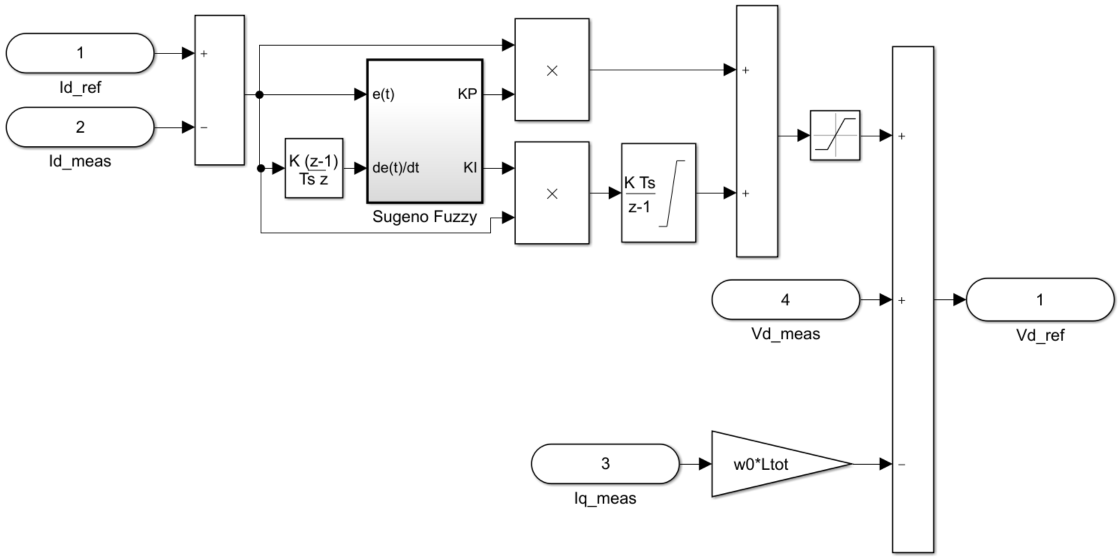

Figure A.42: Current control block diagram in simulations for fuzzy logic PI control in d-frame.

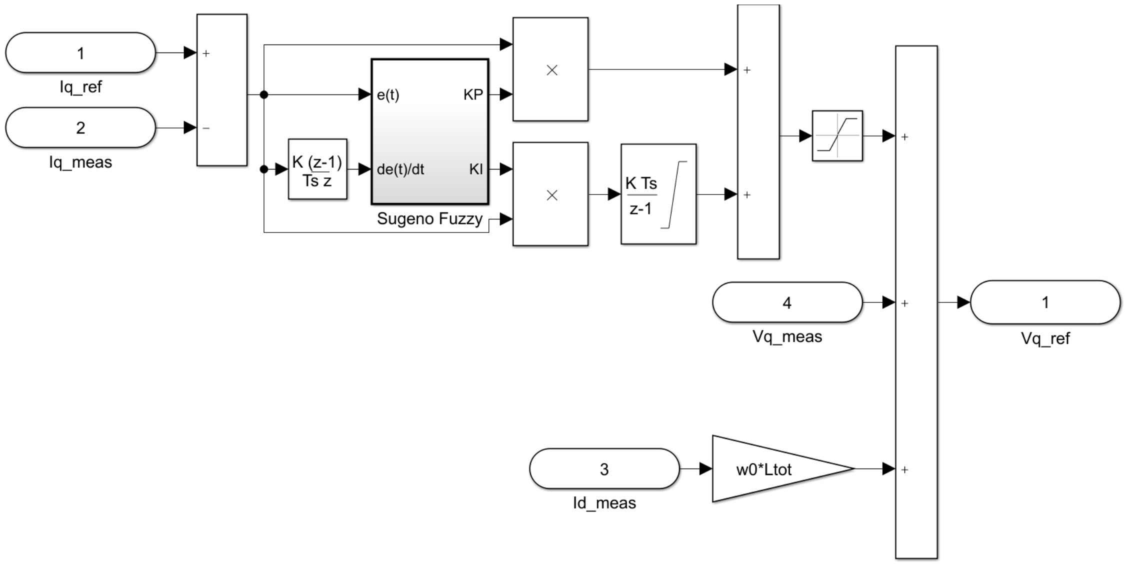

Figure A.43: Current control block diagram in simulations for fuzzy logic PI control in q-frame.

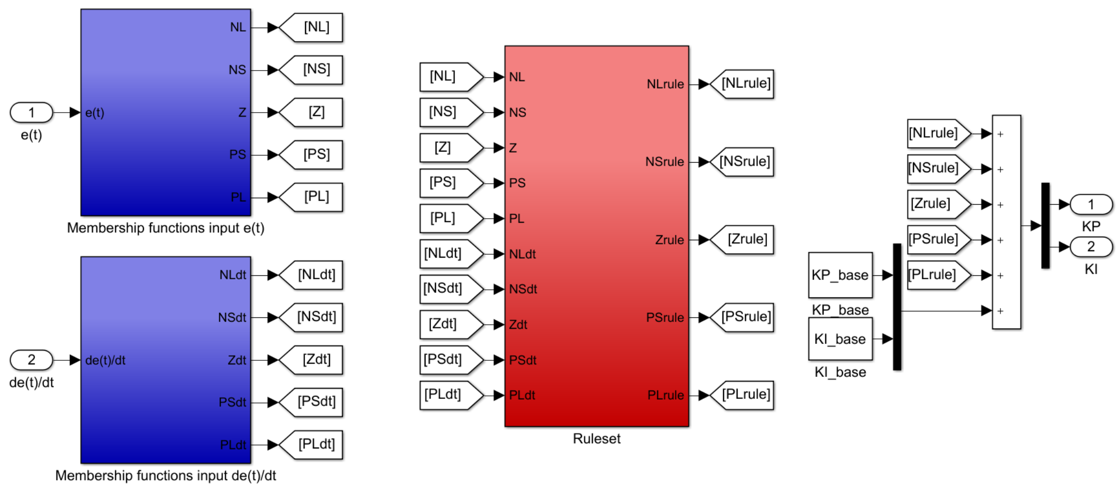

Figure A.44: Overview of the fuzzy logic Sugeno controller build from scratch.

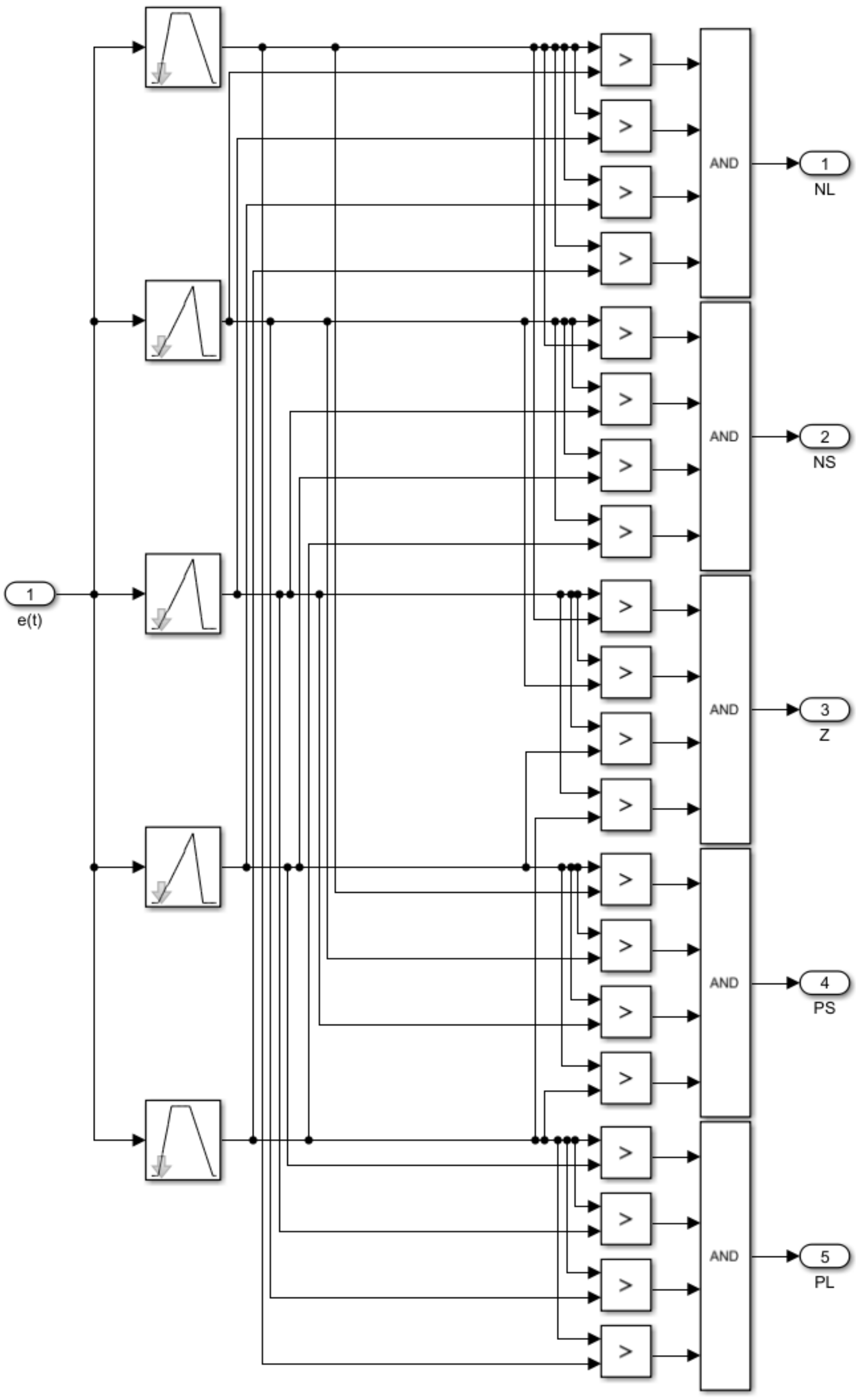

Figure A.45: Membership functions and evaluation of the error for fuzzy logic controller build from scratch.

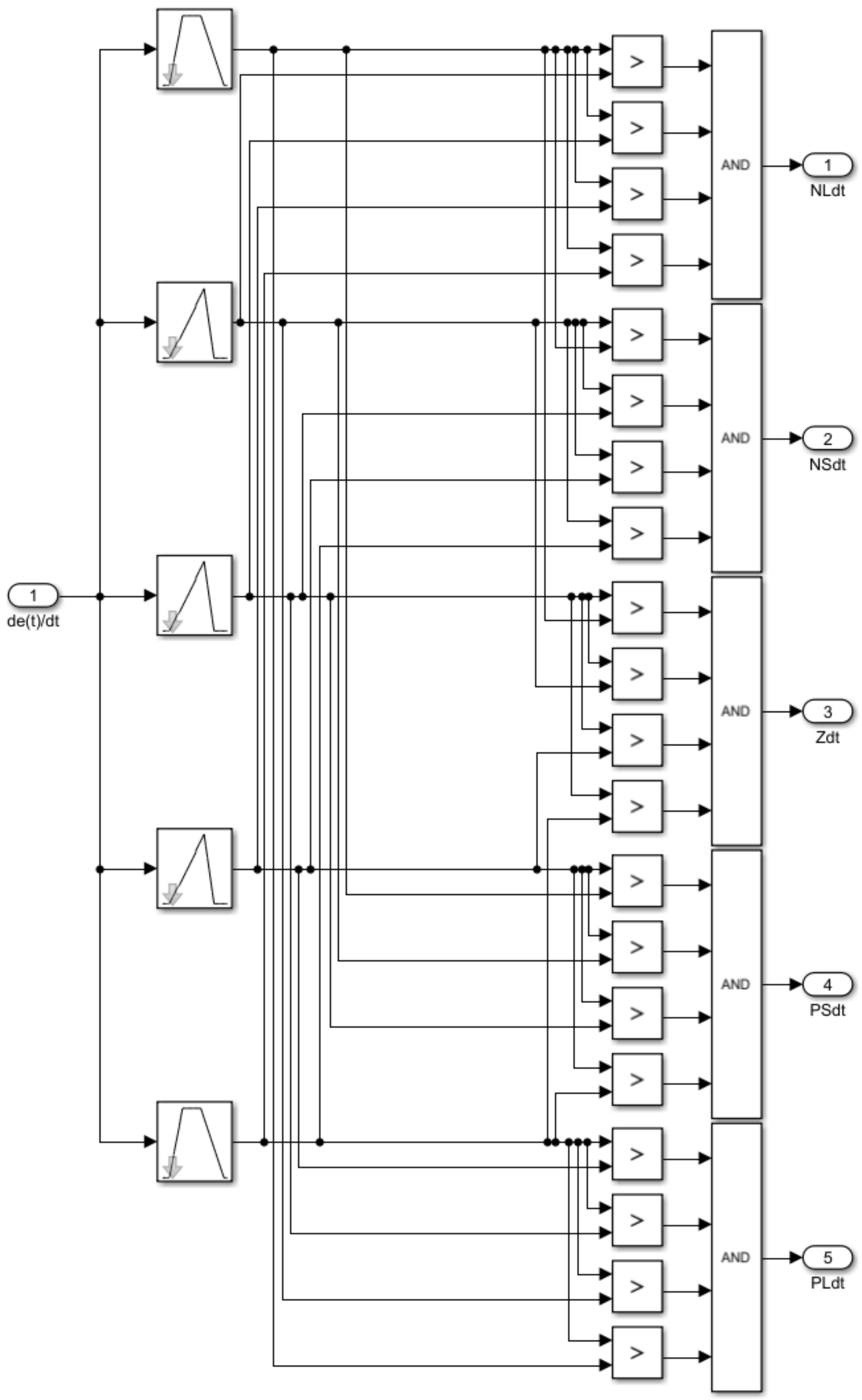

Figure A.46: Membership functions and evaluation of the change in error for fuzzy logic controller build from scratch.

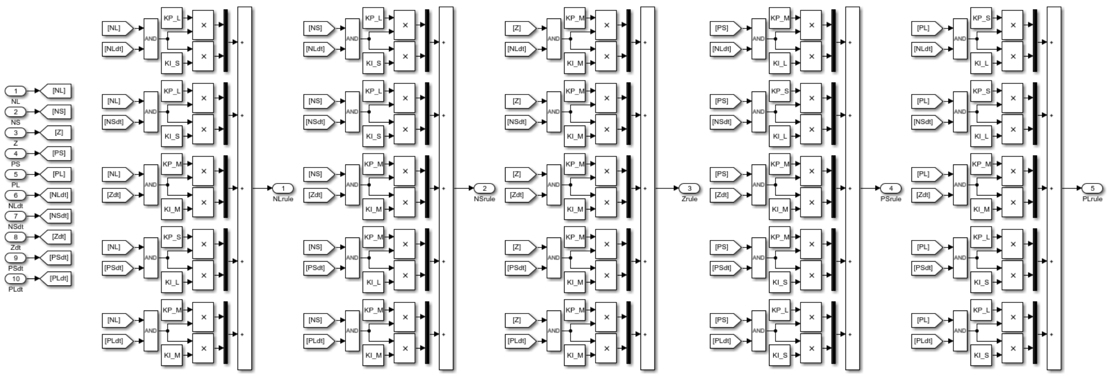

Figure A.47: Ruleset for fuzzy logic controller build from scratch.

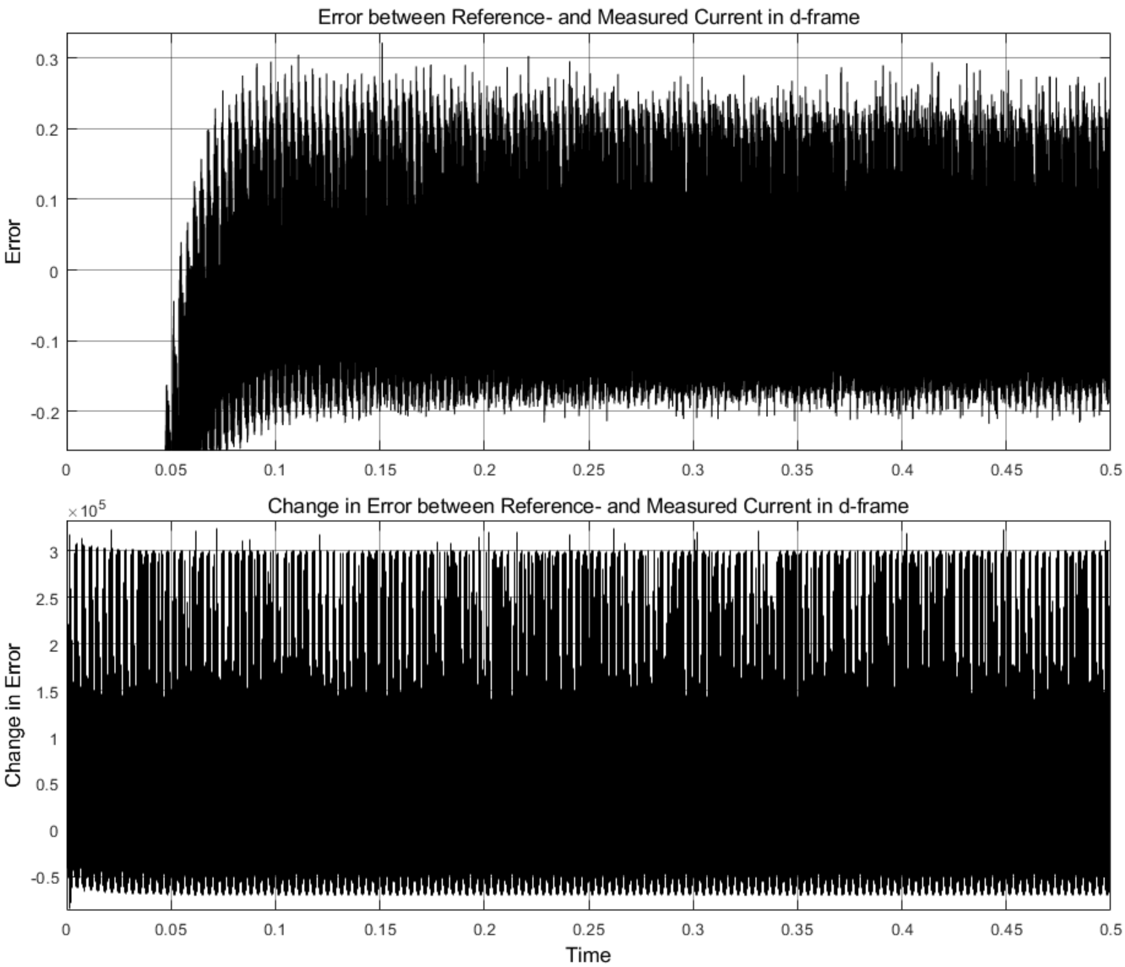

Figure A.48: Error and change in error measurements in d-frame from the conventional PI control scheme simulation used to tune the membership functions for the fuzzy logic controller.

A.11 Fuzzy Logic PR Control

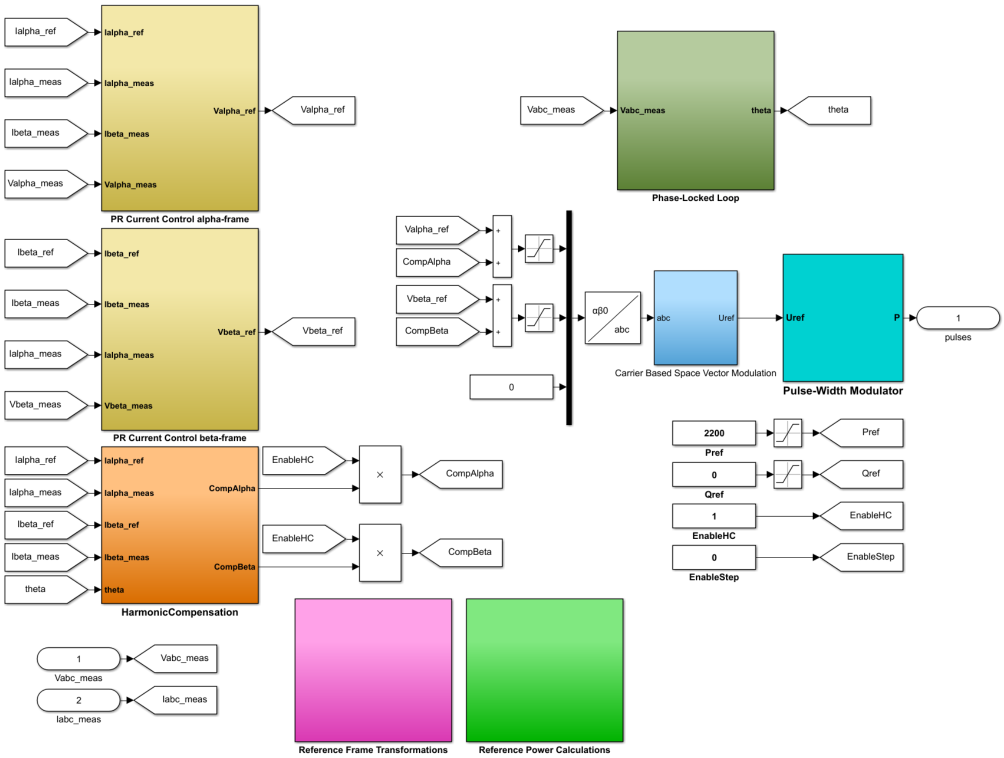

Figure A.49: Current Control block for fuzzy logic PR control scheme simulation.

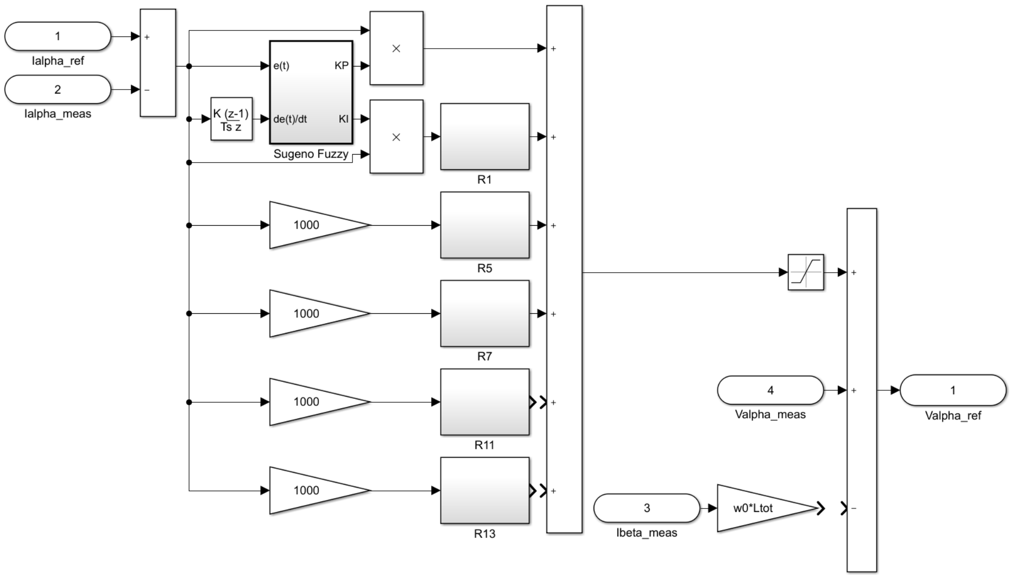

Figure A.50: Current control block diagram in simulations for fuzzy logic PR control in alpha-frame.

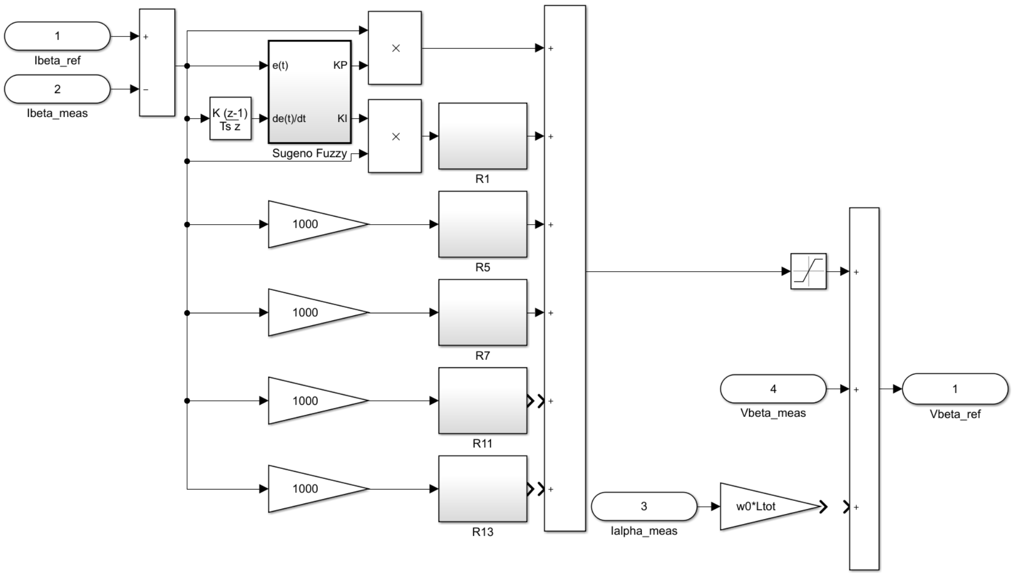

Figure A.51: Current control block diagram in simulations for fuzzy logic PI control in beta-frame.

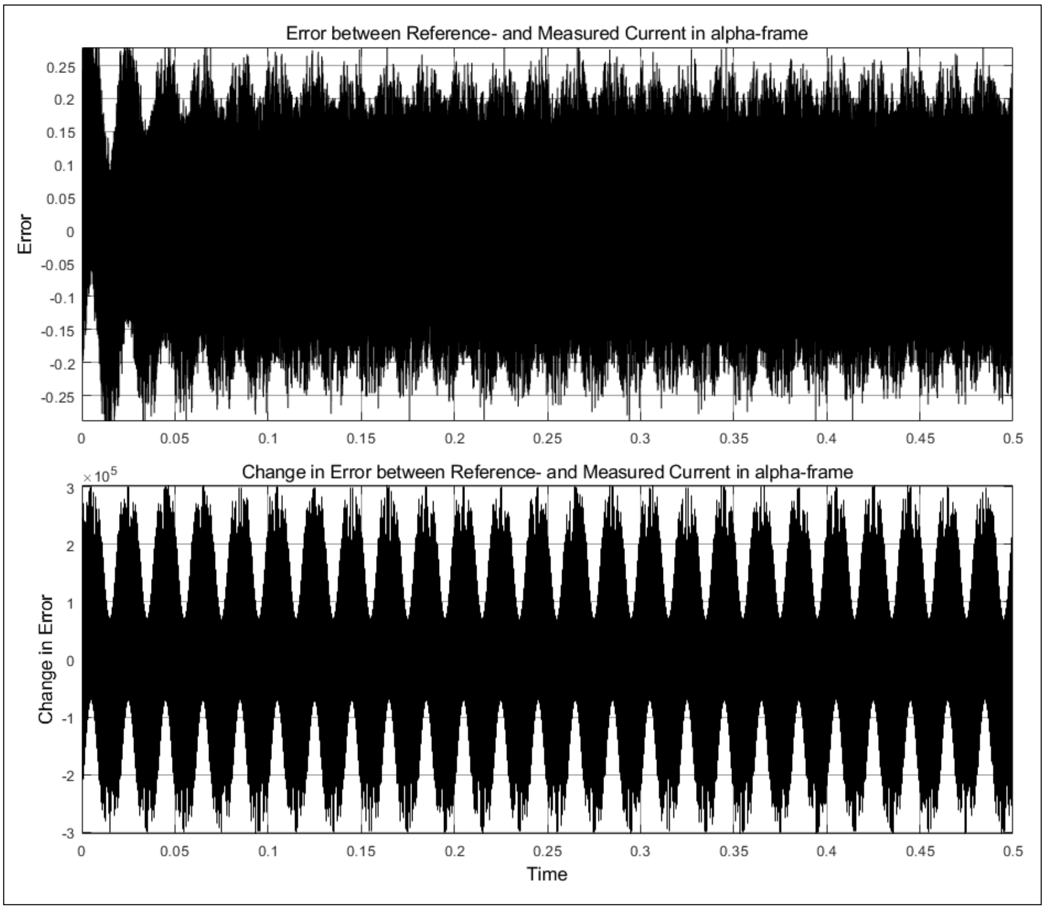

Figure A.52: Error and change in error measurements in q-frame from the conventional PI control scheme simulation used to tune the membership functions for the fuzzy logic controller.

A.12 Experimental Setup

Figure A.53: The experimental laboratory setup including the three-phase grid connection, DC power source, computer and electrical components such as inverter, LCL filter, etc..

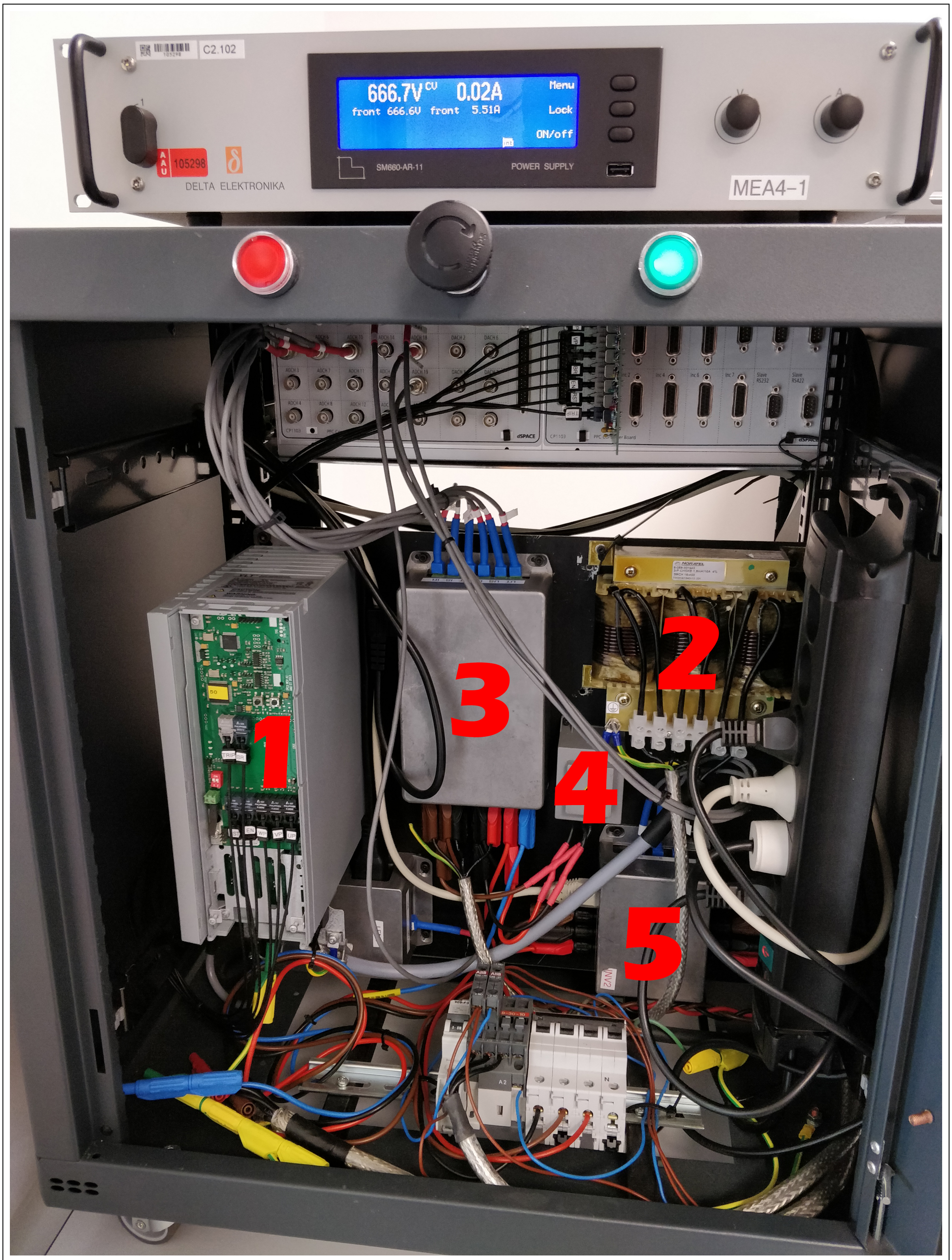

Figure A.54: Close-up of the electrical components in the experimental laboratory setup, including the inverter, LCL filter, etc..

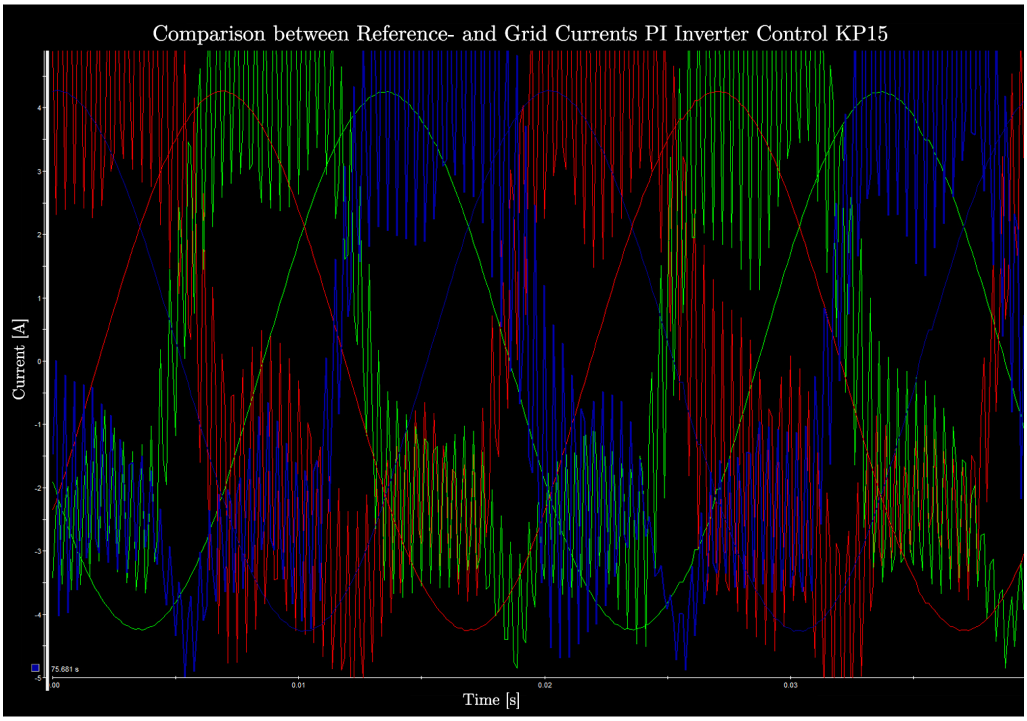

Figure A.55: Grid current measurements compared the reference currents for the laboratory PI control scheme using inverter current measurements in the control loop for K_P=15.

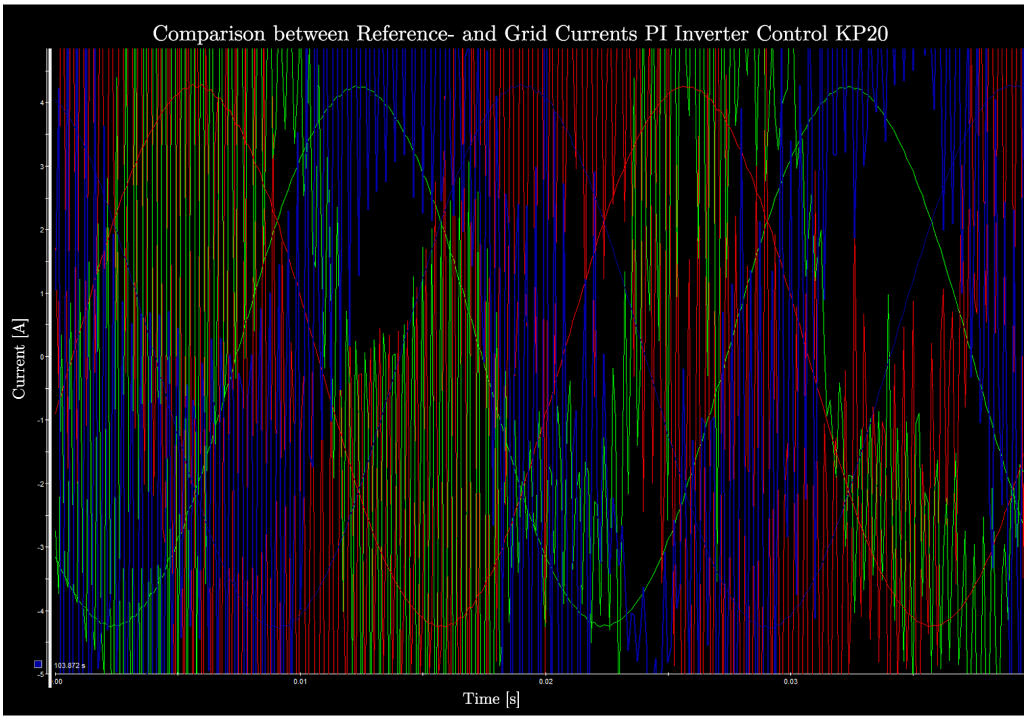

Figure A.56: Grid current measurements compared the reference currents for the laboratory PI control scheme using inverter current measurements in the control loop for K_P=20.

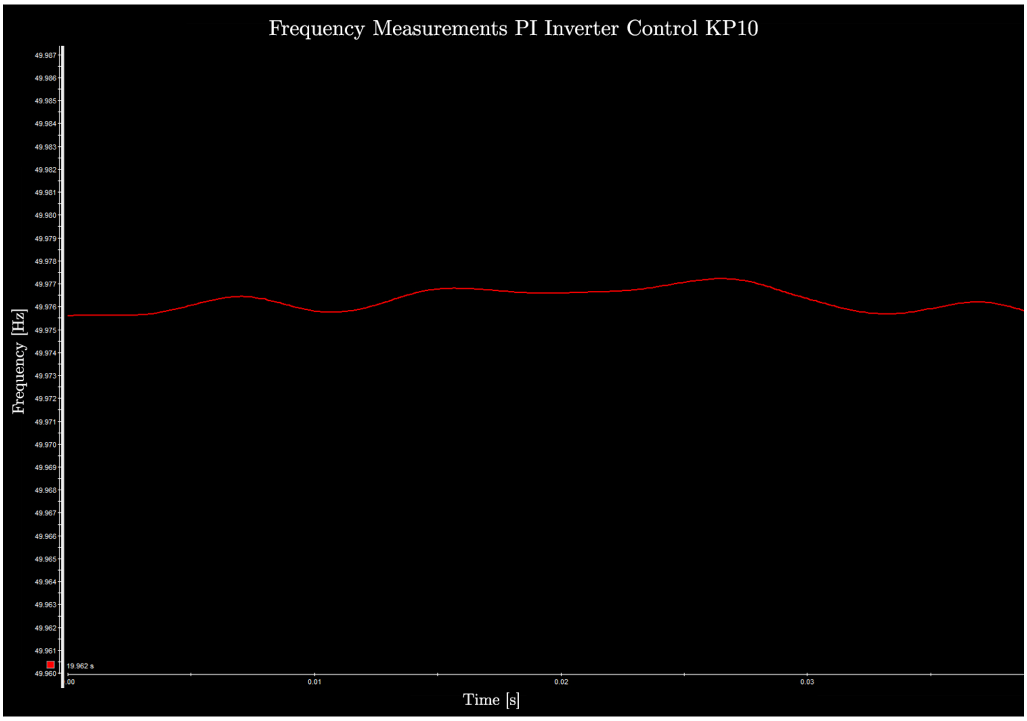

Figure A.57: Frequency measurements for the laboratory PI control scheme using inverter current measurements in the control loop for K_P=10.

A.13 PI Control Laboratory

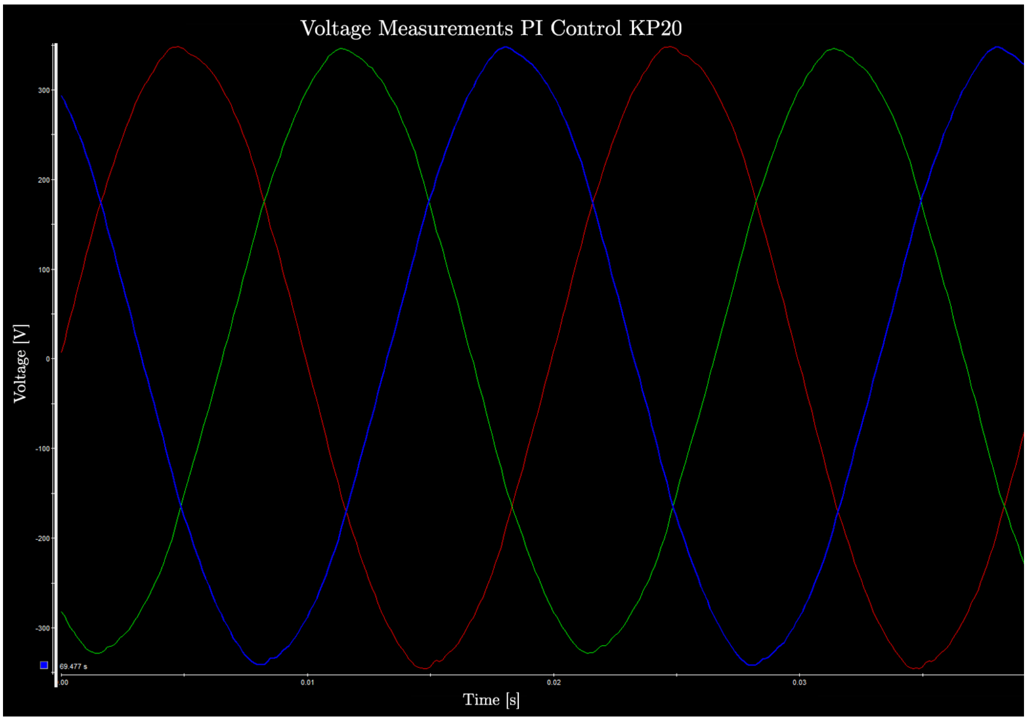

Figure A.58: Voltage measurements of the capacitor voltage in the laboratory PI control scheme for K_P=20.

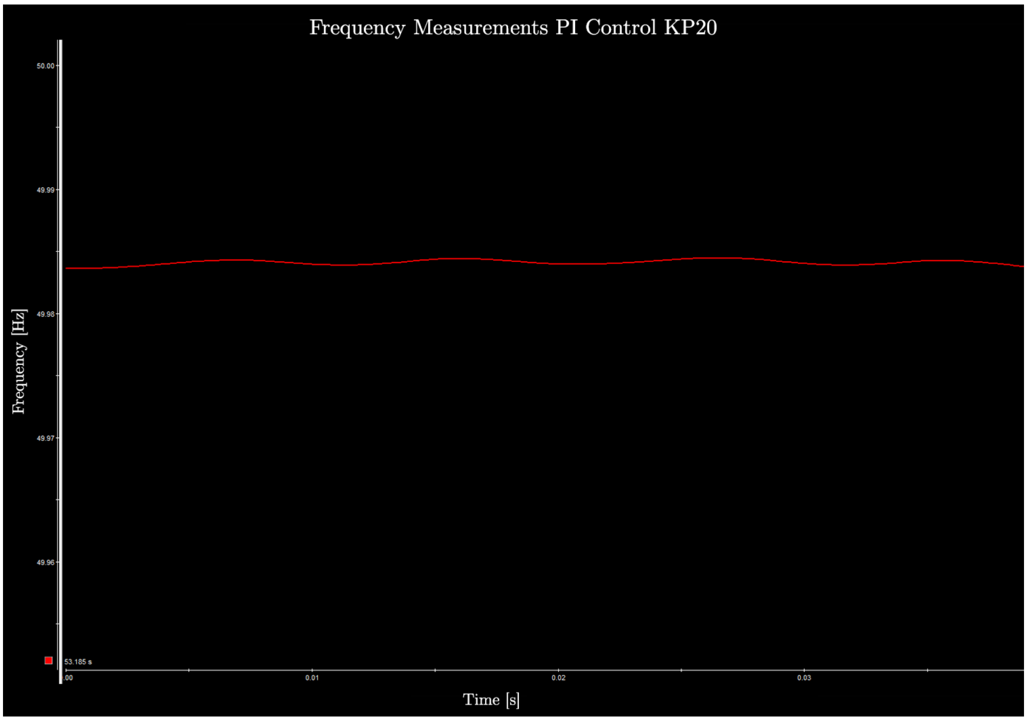

Figure A.59: Frequency measurements in the laboratory PI control scheme for K_P=20.

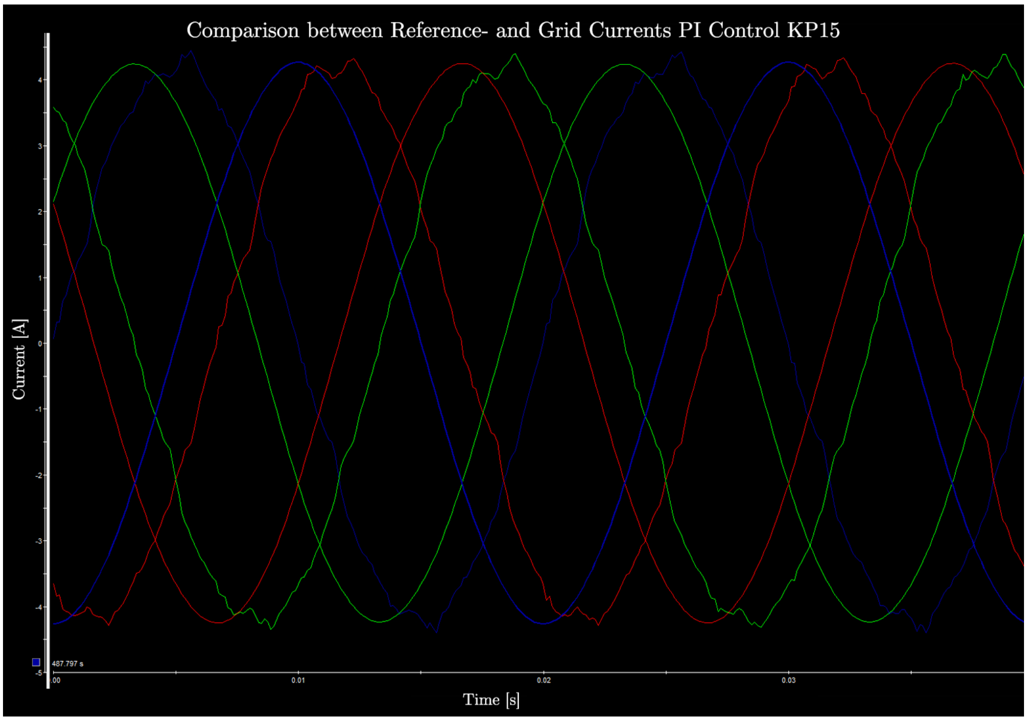

Figure A.60: Comparison of the grid- and reference currents for PI control scheme in experimental setup with $K_P = 15$.

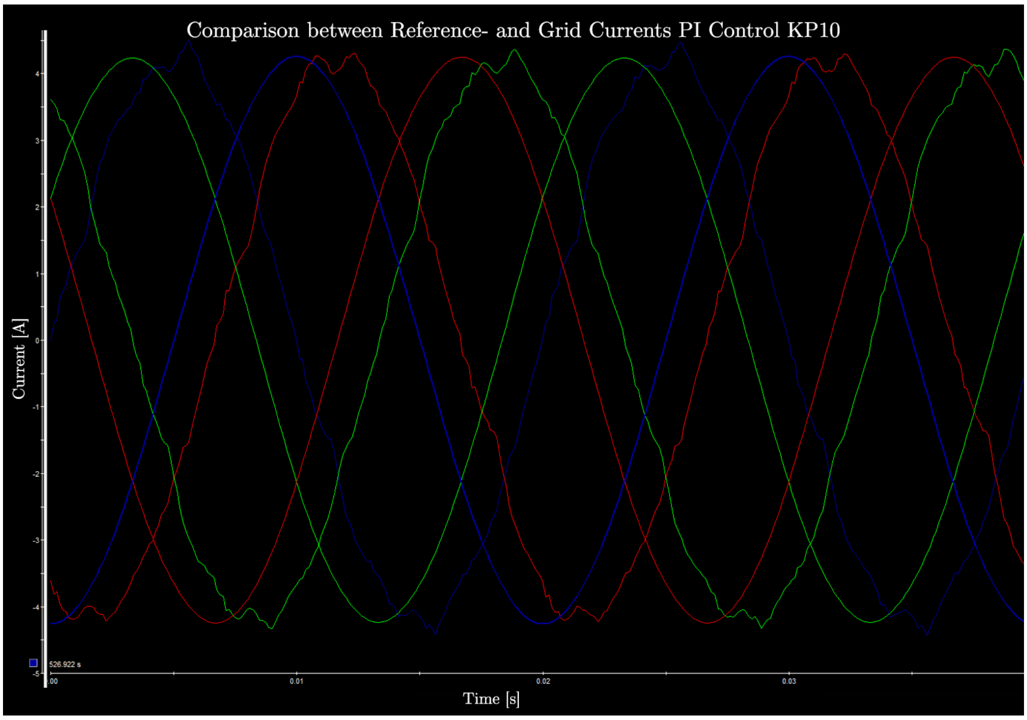

Figure A.61: Comparison of the grid- and reference currents for PI control scheme in experimental setup with $K_P = 10$.

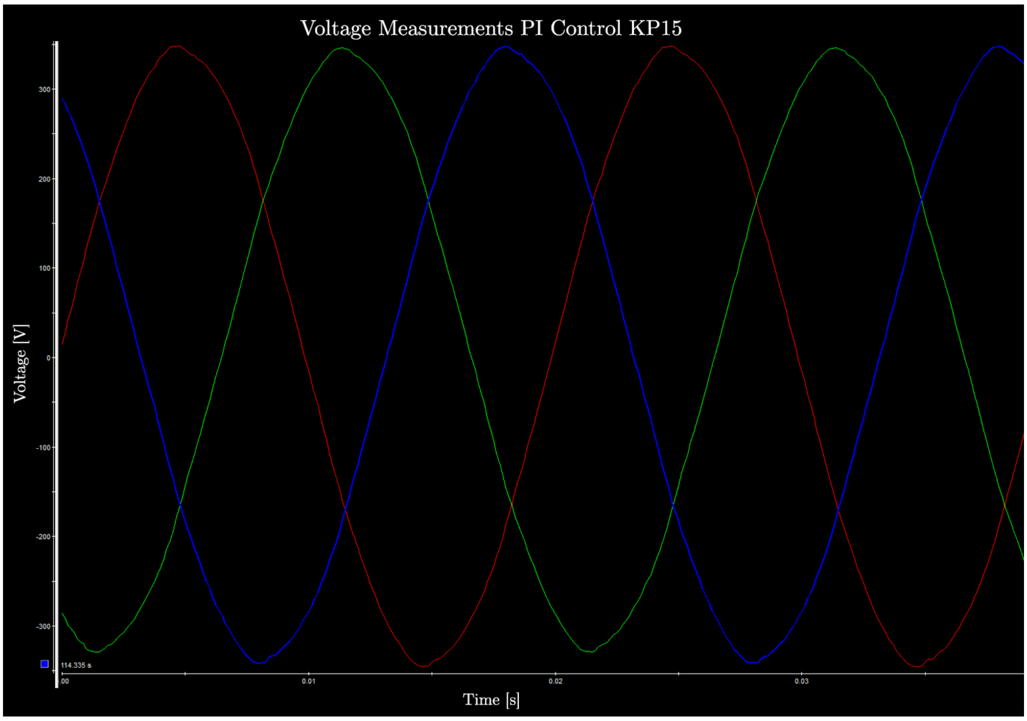

Figure A.62: Voltage measurements of the capacitor voltage in the laboratory PI control scheme for K_P=15.

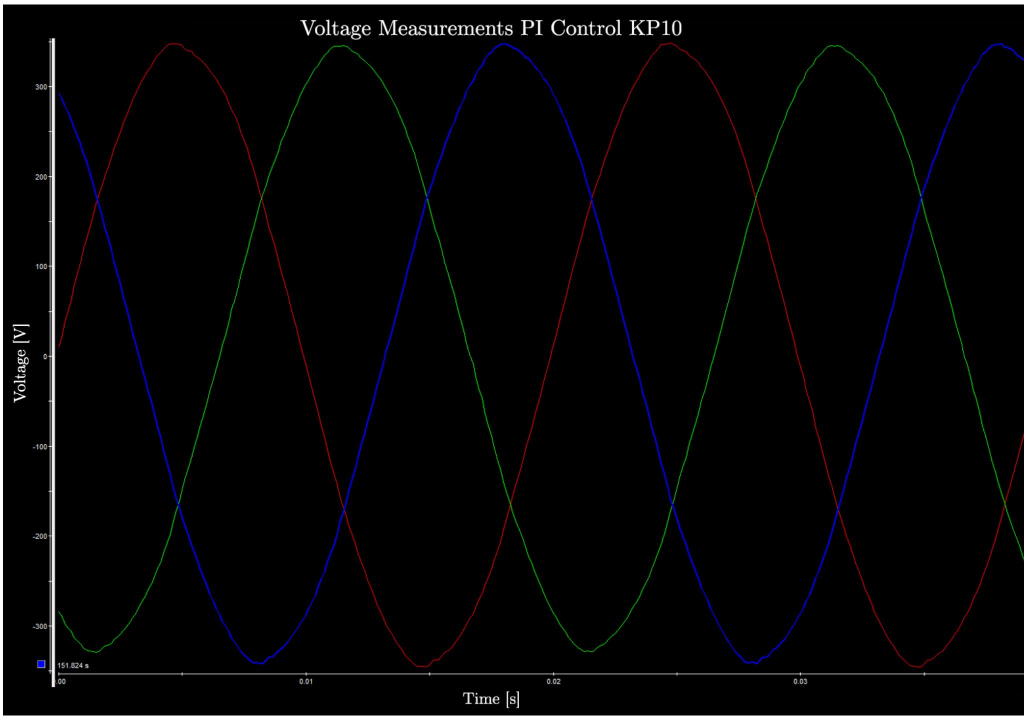

Figure A.63: Voltage measurements of the capacitor voltage in the laboratory PI control scheme for K_P=10.

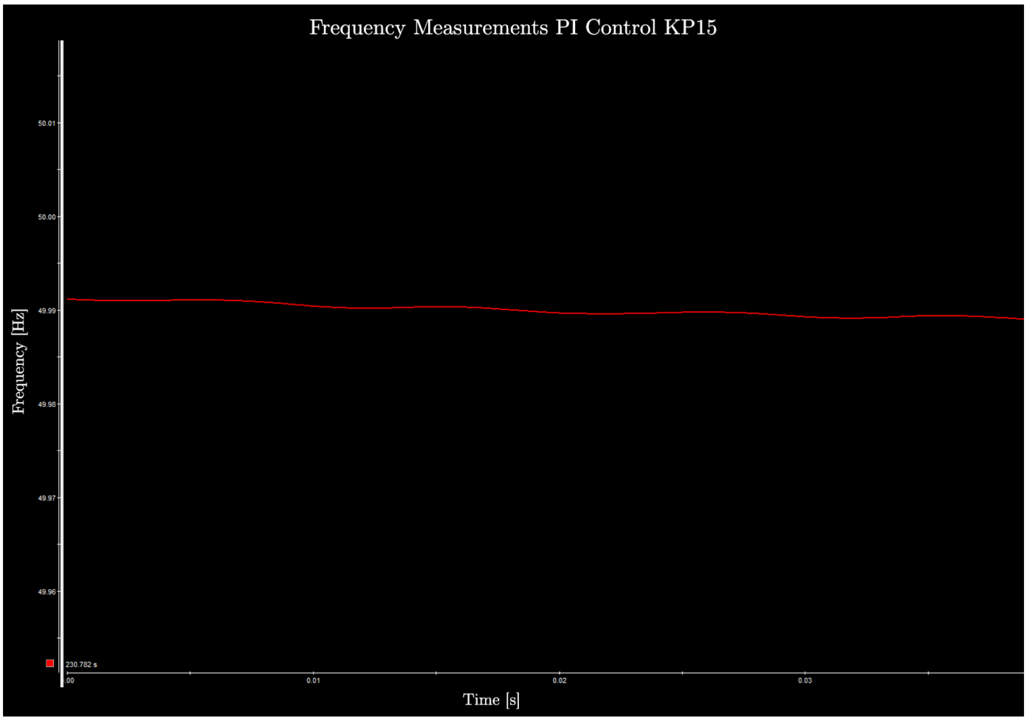

Figure A.64: Frequency measurements in the laboratory PI control scheme for K_P=15.

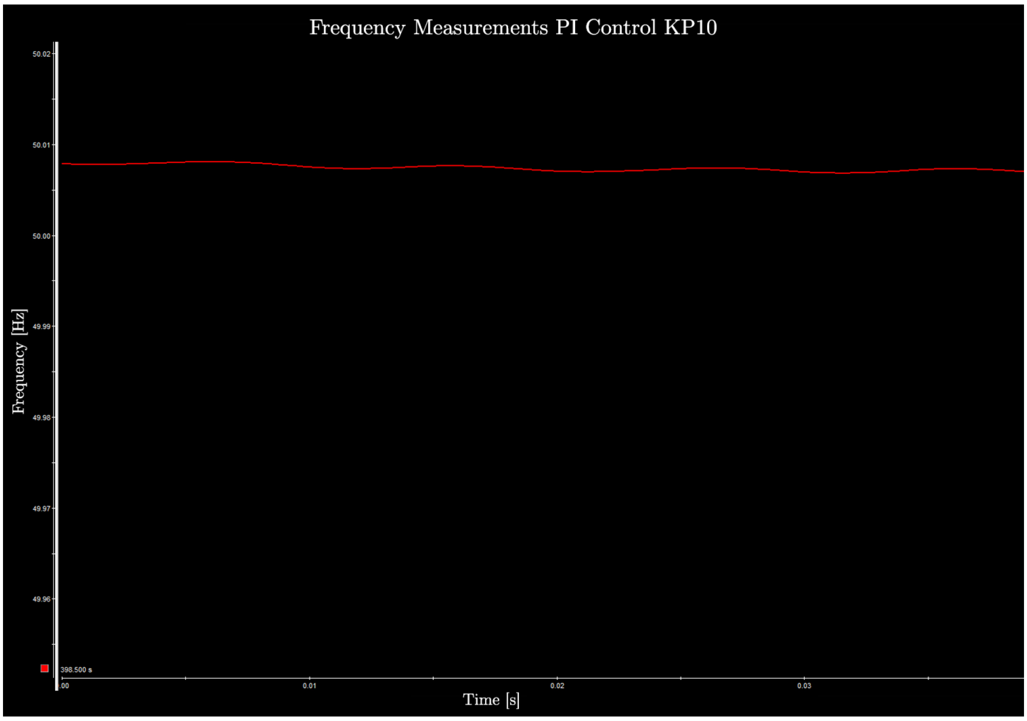

Figure A.65: Frequency measurements in the laboratory PI control scheme for K_P=10.

A.14 PR Control Laboratory

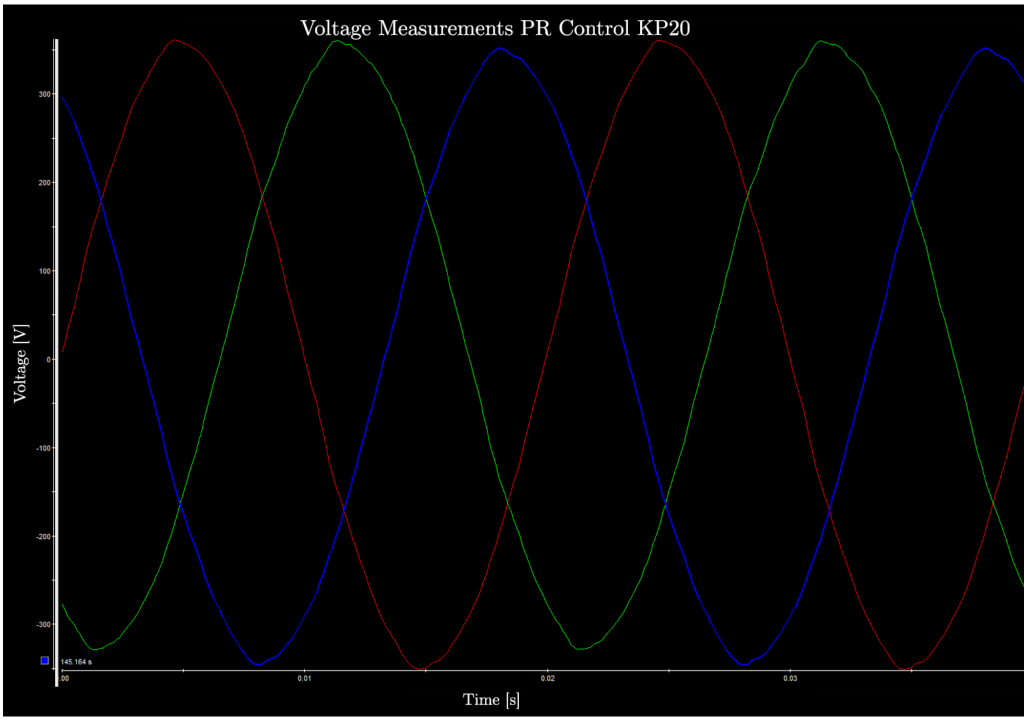

Figure A.66: Voltage measurements of the capacitor voltage in the laboratory PR control scheme for K_P=20.

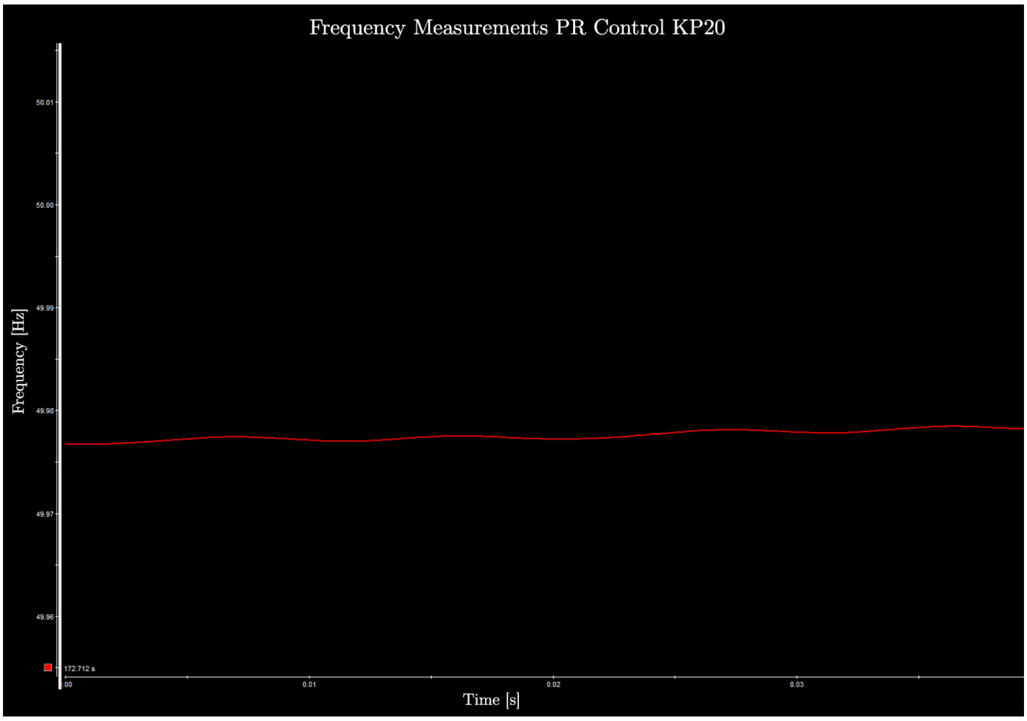

Figure A.67: Frequency measurements in the laboratory PR control scheme for K_P=20.

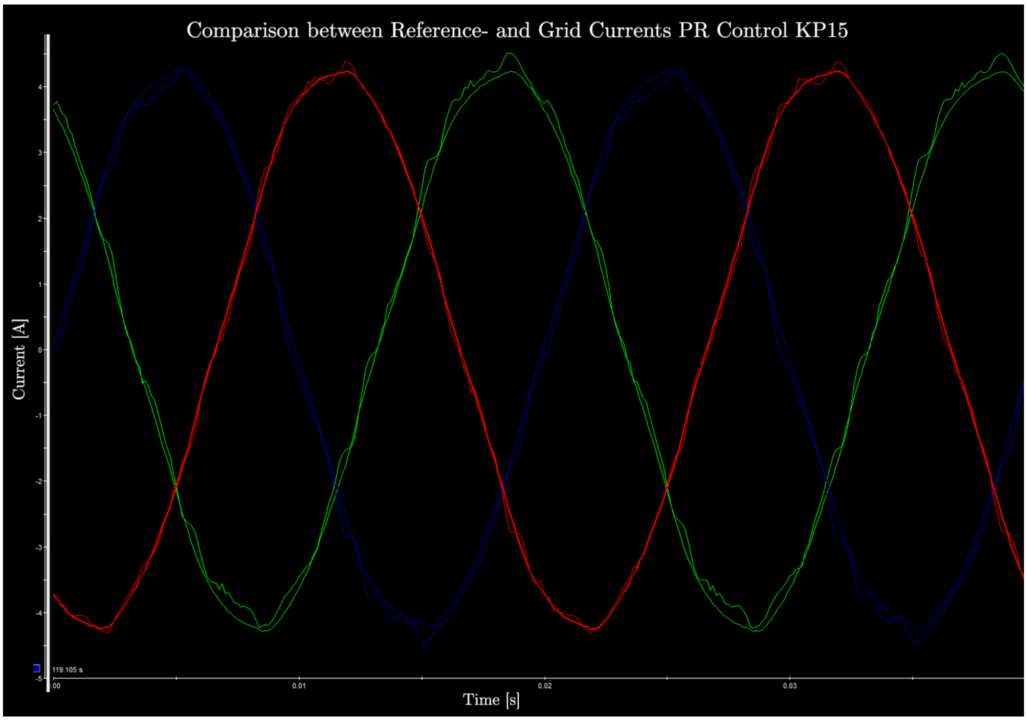

Figure A.68: Comparison of the grid- and reference currents for PR control scheme in experimental setup with $K_P = 15$.

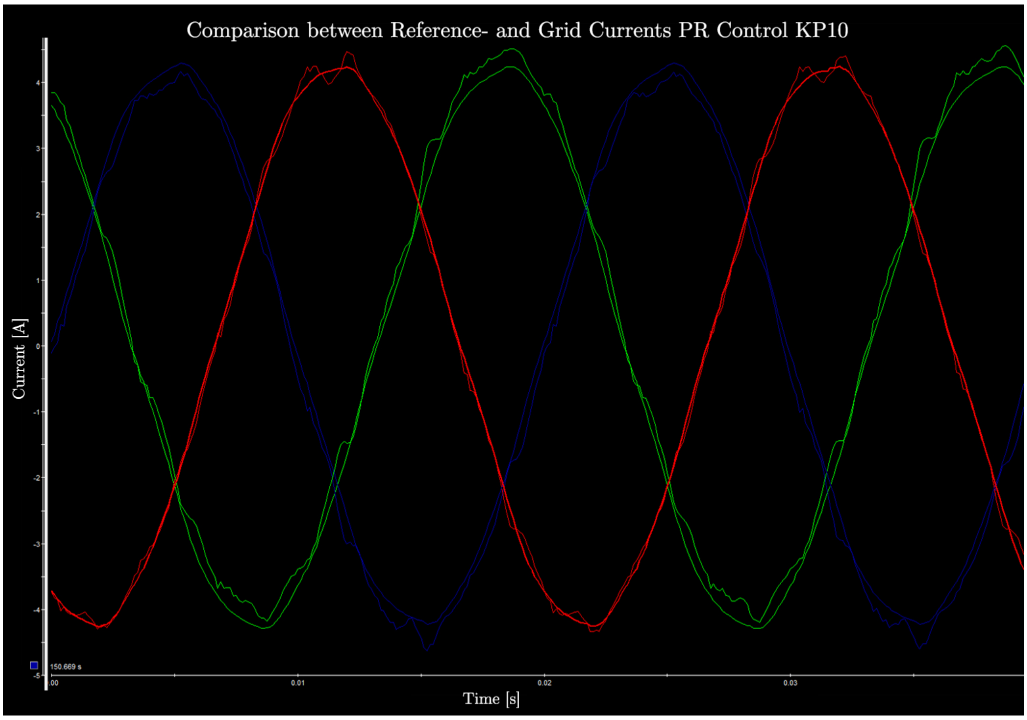

Figure A.69: Comparison of the grid- and reference currents for PR control scheme in experimental setup with $K_P = 10$.

A.15 Fuzzy Logic PI Control Laboratory

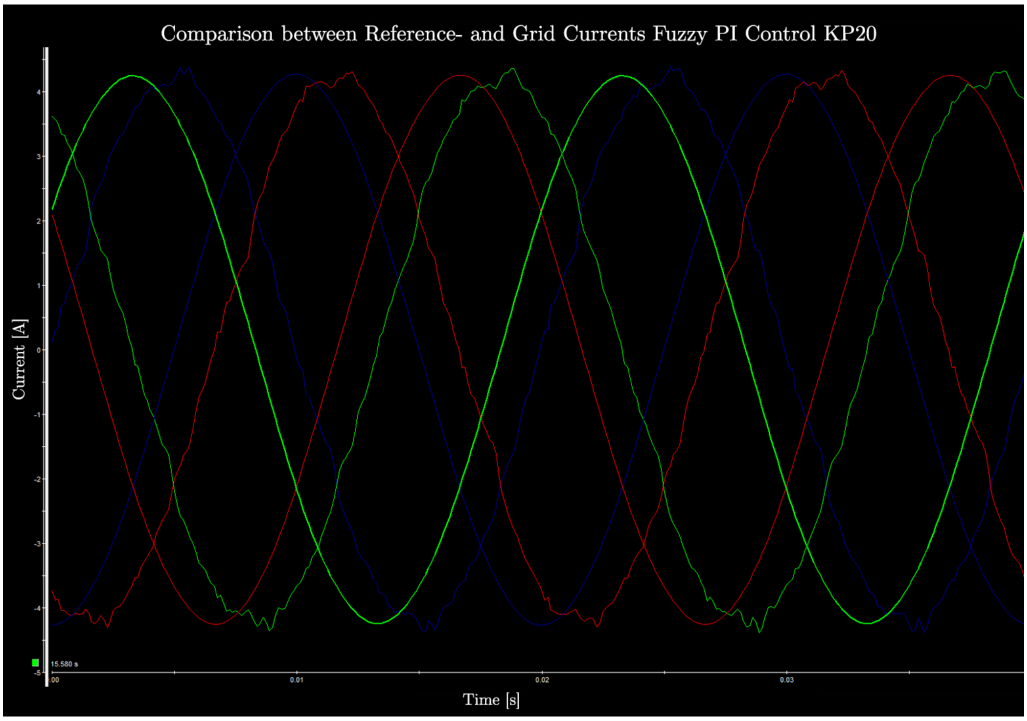

Figure A.70: Comparison of the grid- and reference currents for fuzzy logic controlled PI control scheme in experimental setup with $K_P = 20 \pm 1$.

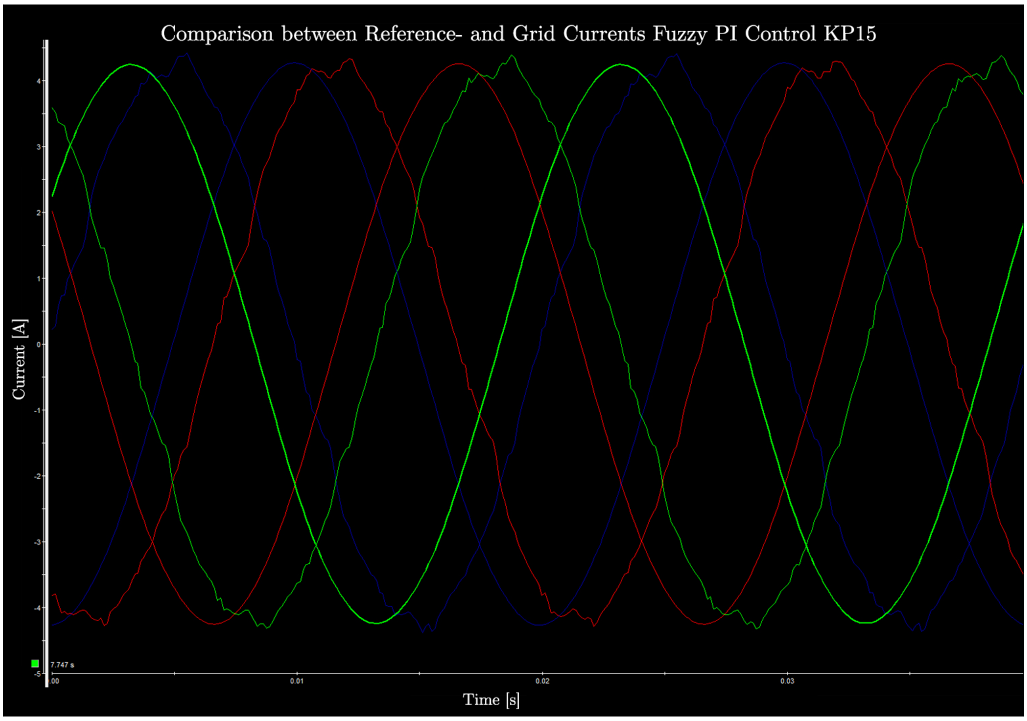

Figure A.71: Comparison of the grid- and reference currents for fuzzy logic controlled PI control scheme in experimental setup with $K_P = 15 \pm 1$.

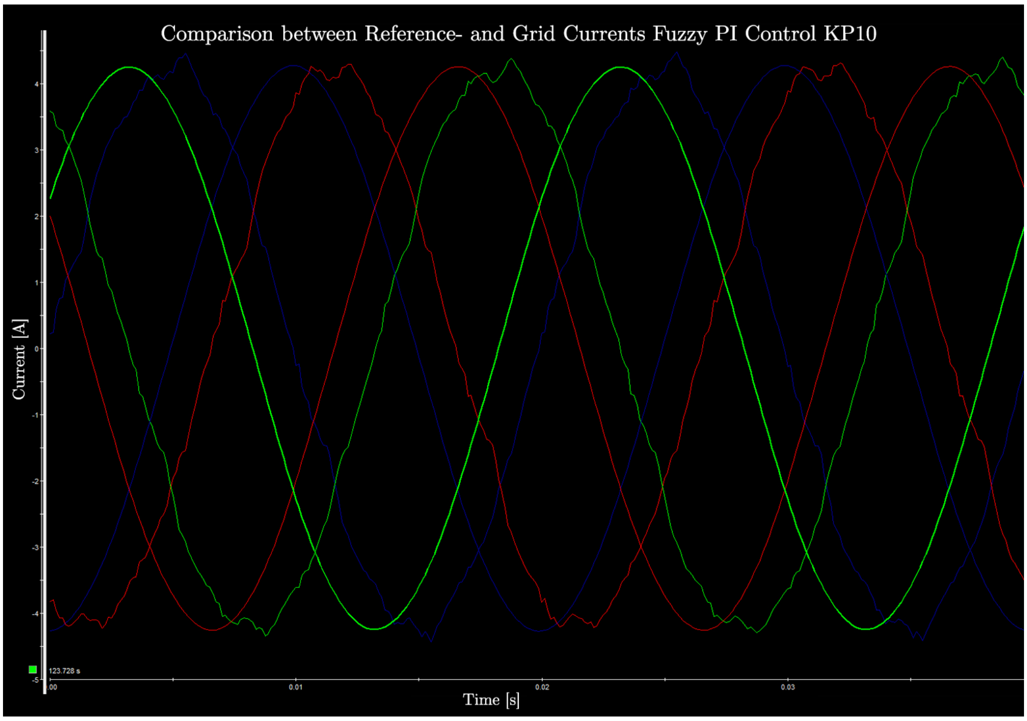

Figure A.72: Comparison of the grid- and reference currents for fuzzy logic controlled PI control scheme in experimental setup with $K_P = 10 \pm 1$.

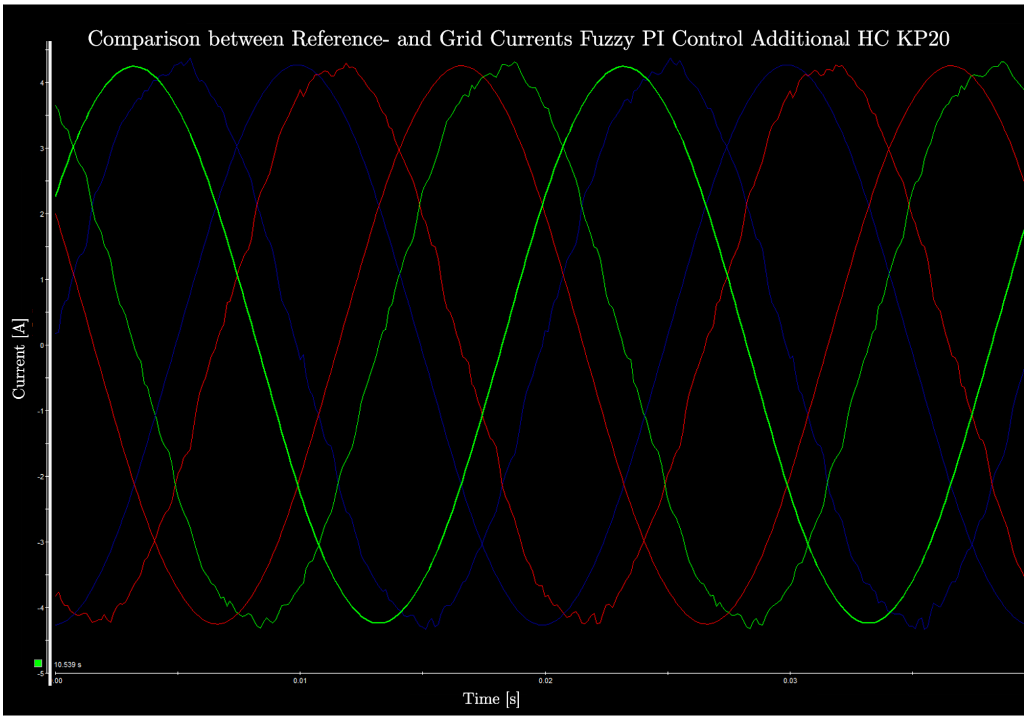

Figure A.73: Comparison of the grid- and reference currents for fuzzy logic controlled PI control scheme in experimental setup with $K_P = 20 \pm 1$ and additional harmonic compensation for the 11^{th} and 13^{th} harmonics.

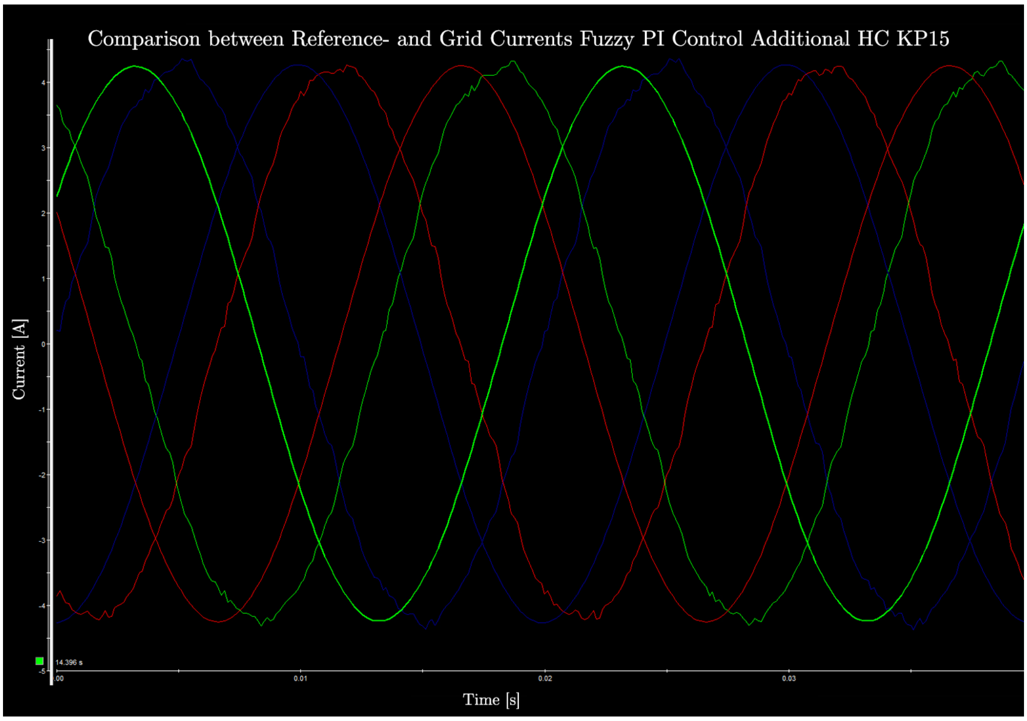

Figure A.74: Comparison of the grid- and reference currents for fuzzy logic controlled PI control scheme in experimental setup with $K_P = 15 \pm 1$ and additional harmonic compensation for the 11^{th} and 13^{th} harmonics.

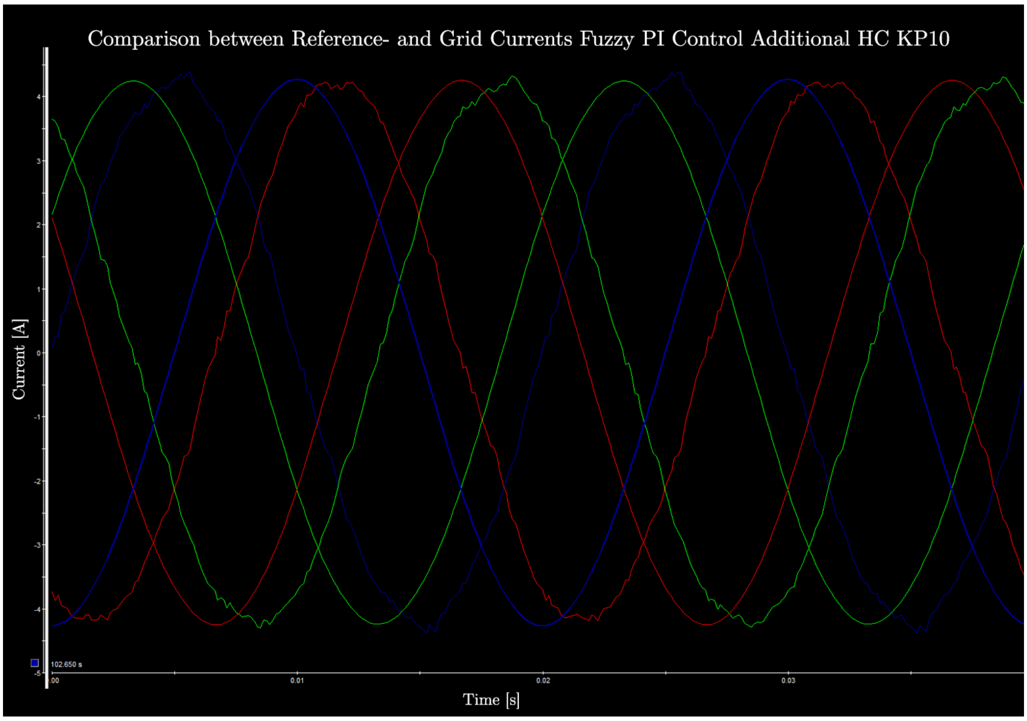

Figure A.75: Comparison of the grid- and reference currents for fuzzy logic controlled PI control scheme in experimental setup with $K_P = 10 \pm 1$ and additional harmonic compensation for the 11^{th} and 13^{th} harmonics.

A.16 Fuzzy Logic PR Control Laboratory

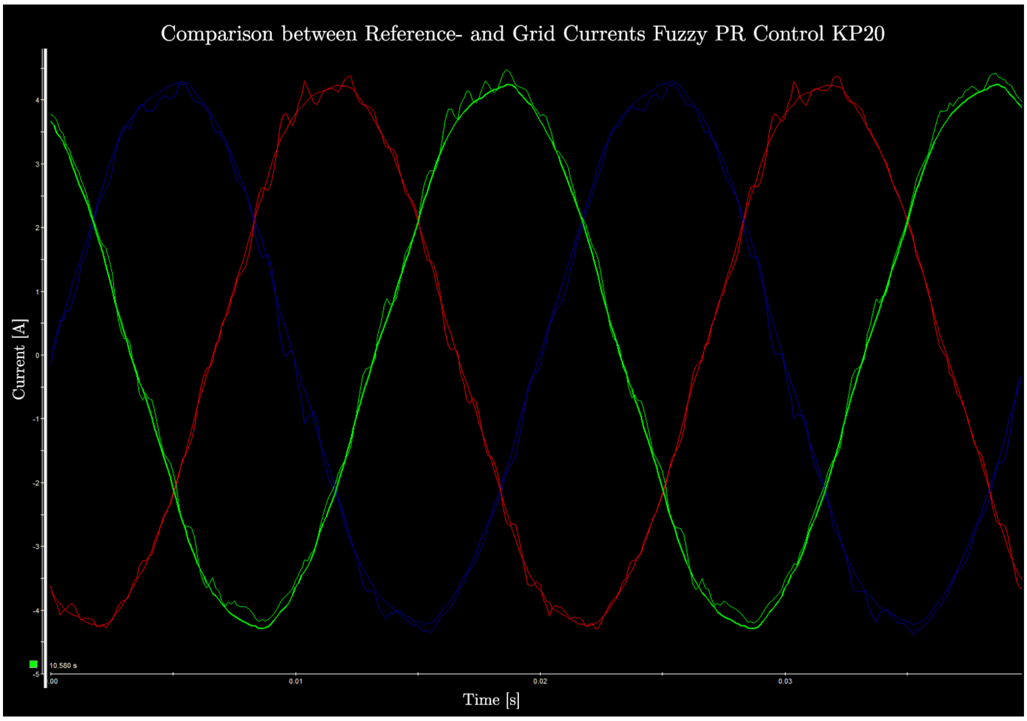

Figure A.76: Comparison of the grid- and reference currents for fuzzy logic controlled PR control scheme in experimental setup with $K_P = 20 \pm 1$.

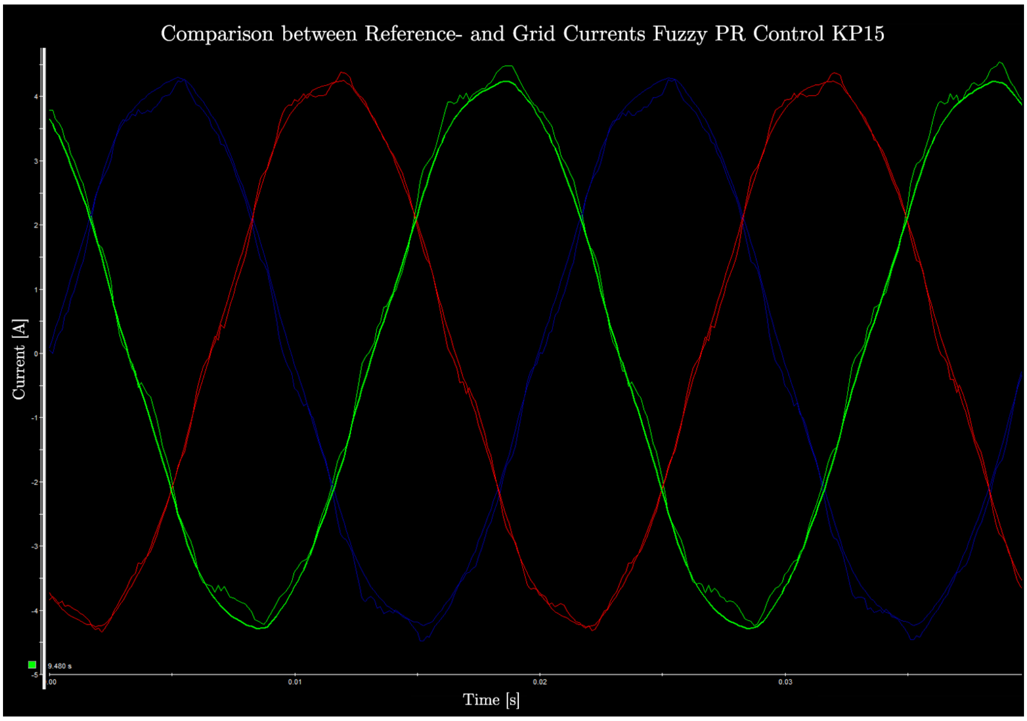

Figure A.77: Comparison of the grid- and reference currents for fuzzy logic controlled PR control scheme in experimental setup with $K_P = 15 \pm 1$.

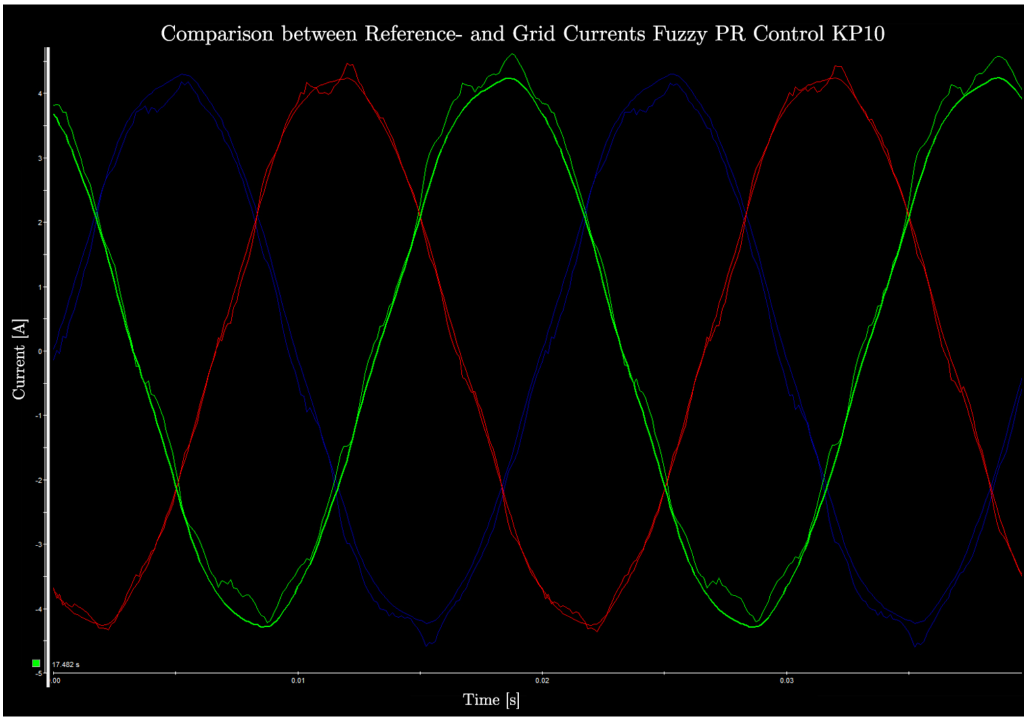

Figure A.78: Comparison of the grid- and reference currents for fuzzy logic controlled PR control scheme in experimental setup with $K_P = 10 \pm 1$.